2017

Developing an oculomotor brain-computer interface and characterizing its dynamic functional network

BOSTON UNIVERSITY

GRADUATE SCHOOL OF ARTS AND SCIENCES

Dissertation

DEVELOPING AN OCULOMOTOR BRAIN-COMPUTER INTERFACE AND CHARACTERIZING ITS DYNAMIC FUNCTIONAL NETWORK

by

NAN JIA

B.Sc., Rensselaer Polytechnic Institute, 2009

Submitted in partial fulfillment of the

requirements for the degree of

Doctor of Philosophy

2017

Approved by

First Reader

Frank H. Guenther, Ph.D.
Professor of Speech, Language and Hearing Sciences
Professor of Biomedical Engineering

Second Reader

Daniel Bullock, Ph.D.
Professor of Psychological and Brain Sciences

Third Reader

Arash Yazdanbakhsh, M.D., Ph.D.
Research Assistant Professor of Psychological and Brain Sciences

ACKNOWLEDGMENTS

Sir Isaac Newton famously said: “If I have seen further it is only by standing on the shoulders of giants.” I do not know if I can claim to have seen further, but I am eternally indebted to the giants that have entered my life. If I were only allowed one word to describe my PhD experience, it would be ‘humbling’. I have had the privilege of knowing so many wonderful people, and learning about myself in the last seven and half years.

I am forever grateful for everyone on my committee. My advisor Frank Guenther, for always being supportive, providing honest feedback, and guiding me through the challenging and sometimes frustrating, but always rewarding process of scientific research. Dan Bullock, for being a knowledge bank, and always being there whenever I need feedback and advice. Arash Yazdanbakhsh, for always being positive, and engaging me with discussions. Earl Miller, for providing the resources for animal experiments and guide. Mark Kramer, for providing thoughtful feedback and discussion on challenging issues I faced. Eric Schwartz, for being supportive of me whenever I asked for help.

I also wish to thank my collaborator Scott Brincat, whom has spent an enormous amount of time with me on the project, teaching me about electrophysiology, as well as how to think carefully and thoroughly like an experimentalist. My lab mates Andrés Salazar-Gómez and Mikhail Panko have also been important predecessors in the dissertation project, the work would not be complete without them. I also particularly wish to thank Jason Tourville and Jen Segawa from my lab, for providing highly constructive feedback

for my defense, and Bobbie Holland, for being so incredibly warm and cheering me on whenever I needed a push. I have also received invaluable support from my family and friends, whom were always there for moral support.

Lastly, I would like to express deep gratitude for everyone that was, or still is, in my department. CNS has been a place full of eclectic people with diverse backgrounds and interests. Yet common to all, everyone was willing to share knowledge, engage in debates, and be open-minded and supportive of each other. I will forever carry with me the memories of the conversations that happened in the hallways of CNS, the Room of Science, the Colonial Oven, the Elk House, and at many other countless times and locations. The topics ranged from theories of language, representations of perception and cognition, to debates about politics, philosophy, beauty, and just about everything else in life. I never cease to be amazed by the depth and grace of character my fellow peers have shown. My passion and love for science and research will be forever entwined with the memories of all of you. Thank you, for instilling in me that sense of excitement, camaraderie, a healthy dose of skepticism, and love for beauty and truth. I have been exceptionally lucky to know all of you, Himanshu Mhatre, Matthew Silver, Sohrob Kazarounian, Alex Store, Yohan John, Tim Barnes, Jesse Palma, Jeffrey Doon, Karthik Srinivasan, Stefan Berteau, Eric Denovellis, Emily Stephen, Oliver Layton, Sara Saperstein, Wei Guo, Emma Meyers, Byron Galbraith, Jeremy Wurbs, Chris Markiewicz, and Sean Patrick.

DEVELOPING AN OCULOMOTOR BRAIN-COMPUTER INTERFACE AND CHARACTERIZING ITS DYNAMIC FUNCTIONAL NETWORK

NAN JIA

Boston University Graduate School of Arts and Sciences, 2017

Major Professor: Frank H. Guenther, Ph.D., Professor of Speech, Language, and Hearing Sciences, Professor of Biomedical Engineering

ABSTRACT

To date, invasive brain-computer interface (BCI) research has largely focused on replacing lost limb functions using signals from hand/arm areas of motor cortex. However, the oculomotor system may be better suited to BCI applications involving rapid serial selection from spatial targets, such as choosing from a set of possible words displayed on a computer screen in an augmentative and alternative communication application.

First, we develop an intracortical oculomotor BCI based on the delayed saccade paradigm and demonstrate its feasibility to decode intended saccadic eye movement direction in primates. Using activity from three frontal cortical areas implicated in oculomotor production – dorsolateral prefrontal cortex, supplementary eye field, and frontal eye field – we could decode intended saccade direction in real time with high accuracy, particularly at contralateral locations. In a number of analyses in the decoding context, we investigated the amount of saccade-related information contained in different implant regions and in different neural measures. A novel neural measure using power in the 80-500 Hz band is proposed as the optimal signal for this BCI purpose.

In the second part of this thesis, we characterize the interactions between the

neural signals recorded from electrodes in these three implant areas. We employ a number of techniques to quantify the spectrotemporal dynamics in this complex network, and we describe the resulting functional connectivity patterns between the three implant regions in the context of eye-movement production. In addition, we compare and contrast the amount of saccade-related information present in the coupling strengths in the network, on both an electrode-to-electrode scale and an area-to-area scale. Different frequency bands stand out during different epochs of the task, and their information contents are distinct between implant regions. For example, the 13-30 Hz band stands out during the delay epoch, and the 8-12 Hz band is relevant during target and response epochs.

This work extends the boundary of BCI research into the oculomotor domain, and invites potential applications by showing its feasibility. Furthermore, it elucidates the complex dynamics of the functional coupling underlying oculomotor production across multiple areas of frontal cortex.

TABLE OF CONTENTS

LIST OF TABLES

LIST OF FIGURES

LIST OF ABBREVIATIONS

ACC ..... Augmentative and alternative communication

ALDA ..... Adaptive linear discriminant analysis

ANN .....Artificial neural network

ANOVA ..... Analysis of variance

As .....Arcuate sulcus

BCI ..... Brain computer interface

ECoG ..... Electrocorticography

FEF ..... Frontal eye field

LDA ..... Linear discriminant analysis

LFP .....Local field potential

LIS .....Locked-in syndrome

MI .....Mutual information

MS ..... Multiple sclerosis

MU.....Multi-unit

PFC ..... (dorsolateral) Prefrontal cortex

PLV.....Phase-locking value

PPC .....Pairwise-phase consistency

Ps ..... Principal sulcus

SEF ..... Supplementary eye field

SFC ..... Spike-field coherence

SU .....Single unit

1. INTRODUCTION

Brain computer interfaces (BCIs) lie at the intersection of neuroscience and engineering. The knowledge accumulated in these two broad disciplines allows us to understand how the brain functions as well as to build novel applications to benefit broad populations. BMIs can be used to replace motor functions or as rehabilitation tools for afflicted patients, or more generally, as augmentative and alternative communication (AAC) devices to improve communication efficiency for everyday life. BMIs can be broadly divided into two categories by their methods: invasive and non-invasive. Invasive methods usually incur higher financial cost than non-invasive methods and carry risks of infection and surgical complications, but provide better resolution and signal quality. Invasive methods typically use microelectrode arrays or, more recently, electrocorticography (ECoG). At its frontier, one study has demonstrated that a tetraplegia patient with a motor cortex implant can grasp objects with the aid of a robotic arm that receives movement commands decoded from neural activities (Collinger et al., 2013).

The effort of invasive BCIs has largely been aimed to replace skeleto- or limb-motor functions of the suffering population. Yet for paralyzed patients such as those with Locked-In Syndrome (LIS), Multiple Sclerosis (MS), and Amyotrophic Lateral Sclerosis (ALS), even speech and eye movement can be impaired, damaging even the simplest communication efforts. For example, according to the National Institute of Health, it is estimated that the baseline of the ALS population in the US alone is about 30,000, with a

diagnosis of nearly 5,000 new patients annually. A system designed for fast information transfer would be highly desirable to aid these populations in improving their daily communication abilities such as controlling a computer interface. For this purpose, we believe a BMI involving saccadic eye movements is ideal since saccades are naturally rapid and ballistic movements, allowing fast goal acquisition. We develop an eye movement BMI that can be used either as a stand-alone system or to supplement other AACs, targeting the oculomotor regions involved in saccade generation.

The oculomotor system involves multiple brain regions that contribute to different aspects of eye movement production and has been extensively studied. In comparison with hand and arm movement production, the role of attention in influencing neural activities during eye movement is much better known (Kelley et al., 2008; Awh et al., 2006). These factors make the oculomotor system a rich ground of exploration and innovation for BMIs. For this project, we target multiple brain regions implicated in oculomotor control using chronic implants to explore the potential use for an eye movement BMI: dorsolateral prefrontal cortex (PFC), supplementary eye field (SEF), and frontal eye field (FEF).

PFC Located along the posterior portion of the principal sulcus (Brodmann area 46), anterior to area FEF, dlPFC neurons exhibit saccade related activity and directional tuning (Funahashi et al., 1991), but the role of dlPFC in eye movement is less known than FEF and SEF. The dlPFC has been implicated in memory-guided saccades, spatial short-

term memory, and decisional processes related to saccades (Pierrot-Deseilligny et al., 2004).

SEF Located in the dorsomedial frontal cortex anterior to the supplementary motor area, SEF was discovered much later than FEF. The neural activities in SEF share a high resemblance to those found in FEF in saccade tasks (Schall, 1991), but appear to encode saccade endpoints in several different coordinate systems, and as a result SEF has been proposed to be involved in coordinate transformation (Tehovnik et al., 1998; Martinez-Trujillo et al., 2004). The SEF also appears to be involved in contextual executive control of saccades (Stuphorn and Schall, 2006) and motor sequence planning (Tanji and Shima, 1994; Histed and Miller, 2006), but its exact role remains unclear.

FEF FEF has long been known to encode saccade directions in vector form in retinocentric space (Bruce et al., 1985; Tehovnik et al., 2000). FEF is also known to exhibit saccade related activities such as visual, visuo-movement, and movement activities (Bruce and Goldberg, 1985), and memory/delay activity (Sommer and Wurtz, 2001). Located along the anterior bank of the arcuate sulcus and posterior border of the principal sulcus, some topography is known with larger saccades evoked from the dorsomedial portion and smaller saccades from the ventrolateral portion. In addition to having visual and motor responses, FEF also participates in visual selective attention and maintenance of spatial information (Armstrong et al., 2012).

The PFC, SEF, and FEF areas have mostly been studied under acute electrophysiology recording within a single brain region, without much emphasis on their interactions with each other during eye movement production. Yet it has becoming increasingly evident that brain signals interact with each other and exhibit complex rhythmic activities that affect perception/action arising in the cortex. Many models and theories have been proposed to underlie the production and function of different rhythms (Varela *et al.*, 2001; Fries, 2005; Womelsdorf and Fries, 2007; Börgers and Nancy J. Kopell, 2008; Siegel, Donner and Engel, 2012). We analyze the functional connectivity in the three prefrontal oculomotor regions during simultaneous recordings during the BCI task from chronic implants, using different couplings measures.

The breakdown of this dissertation will be as follows: Chapter 2 will present and discuss the details of the implementation, and analysis of the oculomotor BCI task, Chapter 3 will focus on the functional connectivity analysis between spike-field and field-field signals, and finally in Chapter 4, we summarize the results and impact of the project, with a brief discussion of future directions.

2. DECODING OF INTENDED SACCADE DIRECTION IN AN OCULOMOTOR BRAIN-COMPUTER INTERFACE [1]

2.1. Introduction

Brain-computer interfaces (BCIs) utilizing electrodes implanted in cerebral cortex have shown great promise for restoring lost motor function to severely paralyzed individuals. To date, research efforts involving intracortical BCIs have mostly involved implants in the hand/arm area of motor cortex in an effort to control movement of a computer cursor or robotic arm/hand, initially in non-human primates (Serruya *et al.*, 2002; Taylor, Tillery and Schwartz, 2002; Carmena *et al.*, 2003; Velliste *et al.*, 2008; Ifft *et al.*, 2013) and more recently in quadriplegic human participants(Hochberg *et al.*, 2006; Collinger *et al.*, 2013). Human movement capabilities extend far beyond movements of our hands and arms, and different portions of the motor and premotor cortices are specialized for different motor tasks. Accordingly, one would expect that motor cortical areas other than the hand/arm area may be better suited for many BCI tasks. For example, speech motor cortical regions may be better suited than the hand/arm area for controlling movements of a speech synthesizer (Guenther *et al.*, 2009).

Saccades are amongst the fastest and most accurate voluntary movements we make in our everyday lives. Plus, saccades are relatively simple compared to limb movements. They are discrete (step-like), ballistic, and highly stereotyped eye movements. The neural

[1] Part of the work described in this chapter has been published in the Journal of Neural Engineering, Jia et al 2017 *J. Neural Eng.* https://doi.org/10.1088/1741-2552/aa5a3e

representation of saccade has the potential of direct endpoint decoding (Robinson and Fuchs, 1969; Bruce *et al.*, 1985; Russo and Bruce, 2000). Thus, the motor and premotor cortical regions devoted to saccade control may be ideally suited for BCI-driven spatial target selection. Spatial target selection is central to our interfacing with a computer. We choose desired letter keys or menu items. Thus, a BCI capable of making rapid target selections would be of great utility for restoring communication capabilities in individuals suffering from near-total paralysis (as in locked-in syndrome, and the later stages of amyotrophic lateral sclerosis and multiple sclerosis) via an augmentative and alternative communication (AAC) software package.

In the current study, we investigated the use of the saccadic eye movement system for a BCI task involving selection of one of multiple spatially distributed targets on a computer screen (hereafter referred to as an *oculomotor BCI*, see also Brincat *et al.*, 2013; Graf and Andersen, 2014), by predicting the intended saccade directions prior to saccade execution. Two monkeys were implanted chronically with multielectrode arrays in three cortical regions: dorsolateral prefrontal cortex (PFC), supplementary eye field (SEF), and frontal eye field (FEF). PFC, SEF, and FEF are frontal areas that have been implicated in spatial short-term memory, saccade planning, and saccade generation (Funahashi, Chafee and Goldman-Rakic, 1993; Rainer, Asaad and Miller, 1998; Takeda and Funahashi, 2002; Armstrong, Chang and Moore, 2009; Markowitz *et al.*, 2011; Boulay *et al.*, 2015). Saccades can be elicited by low-current electrical stimulation in both SEF and FEF (Robinson and Fuchs, 1969; Bruce *et al.*, 1985; Russo and Bruce, 2000), and FEF in

particular has been shown to contain a vector representation of saccade endpoints (Bruce *et al.*, 1985), making these areas ideal for real-time prediction of saccade plans.

In addition to demonstrating proficient control of the oculomotor BCI, we performed a number of offline analyses to characterize the amount of saccade-related information contained in different brain regions and in different neural activity measures. Previous studies have used a number of different neural activity measures for BCI purposes, including multiunit/single-unit firing rates, local field potentials (LFPs) in different frequency bands, or hybrid signals (Wessberg *et al.*, 2000; Taylor, Tillery and Schwartz, 2002; Mehring *et al.*, 2003; Schalk *et al.*, 2007; Markowitz *et al.*, 2011; Bansal *et al.*, 2012; So *et al.*, 2014), with differing conclusions about which is the most effective for decoding. Here we systematically test a variety of neural activity measures to assess their suitability for decoding intended saccadic eye movement directions.

2.2. Materials and Methods

2.2.1. Monkeys and implants

Two adult male monkeys (monkey C, *Macaca fascicularis,* 9kg, monkey J, *Macaca mulatta,* 11kg) were handled in accordance with National Institutes of Health guidelines and the Massachusetts Institute of Technology Committee on Animal Care. Prior to the recording and BCI sessions, the monkeys were trained to perform a memory-guided saccade task (described further below), which required them to hold the location of one out of six randomly chosen visual targets in memory during a delay period and saccade to

the target location to receive a liquid reward. After they became proficient at the task, three microelectrode arrays (Blackrock Microsystems) each consisting of 32 microelectrodes spaced 400 μm apart and 1 mm in length were implanted unilaterally in dorsolateral prefrontal cortex (PFC), supplementary eye field (SEF), and frontal eye field (FEF) in each monkey. The implant sites were determined prior to surgery using structural magnetic resonance imaging and anatomical atlases. One monkey received implants in the left hemisphere and the other in the right hemisphere, the implant locations for both monkeys are sketched in Figure 2.1.

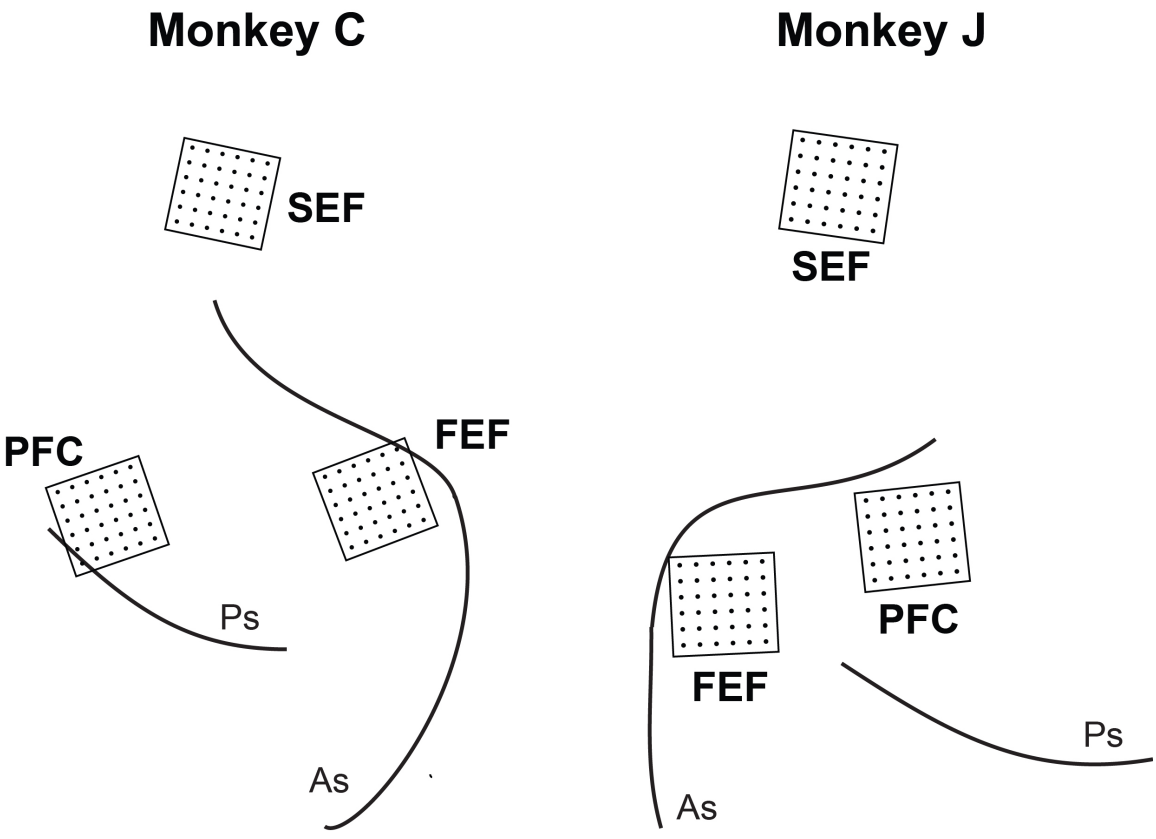

Figure 2.1. Implant locations for both monkeys. Ps: principal sulcus; As: arcuate sulcus; PFC: dorsolateral prefrontal cortex; SEF: supplementary eye field; FEF: frontal eye field.

2.2.2. Brain-computer interface paradigm

The BCI paradigm is a modified version of the memory-guided saccade task (Figure 2.2 A). Monkeys were required to fixate on a dot in the center of the screen, and were briefly (350 ms) presented with one out of six targets (evenly spaced apart at 12.5-degree eccentricity). Following the cue presentation, the monkeys had to keep the cued location in working memory for a 750 ms delay epoch while maintaining central fixation. At the end of the delay epoch, the fixation dot disappeared, signaling the end of enforced fixation. From here on, the task differed depending on which of two phases of the session was being performed: *eye-control trials* or *BCI-control trials*.

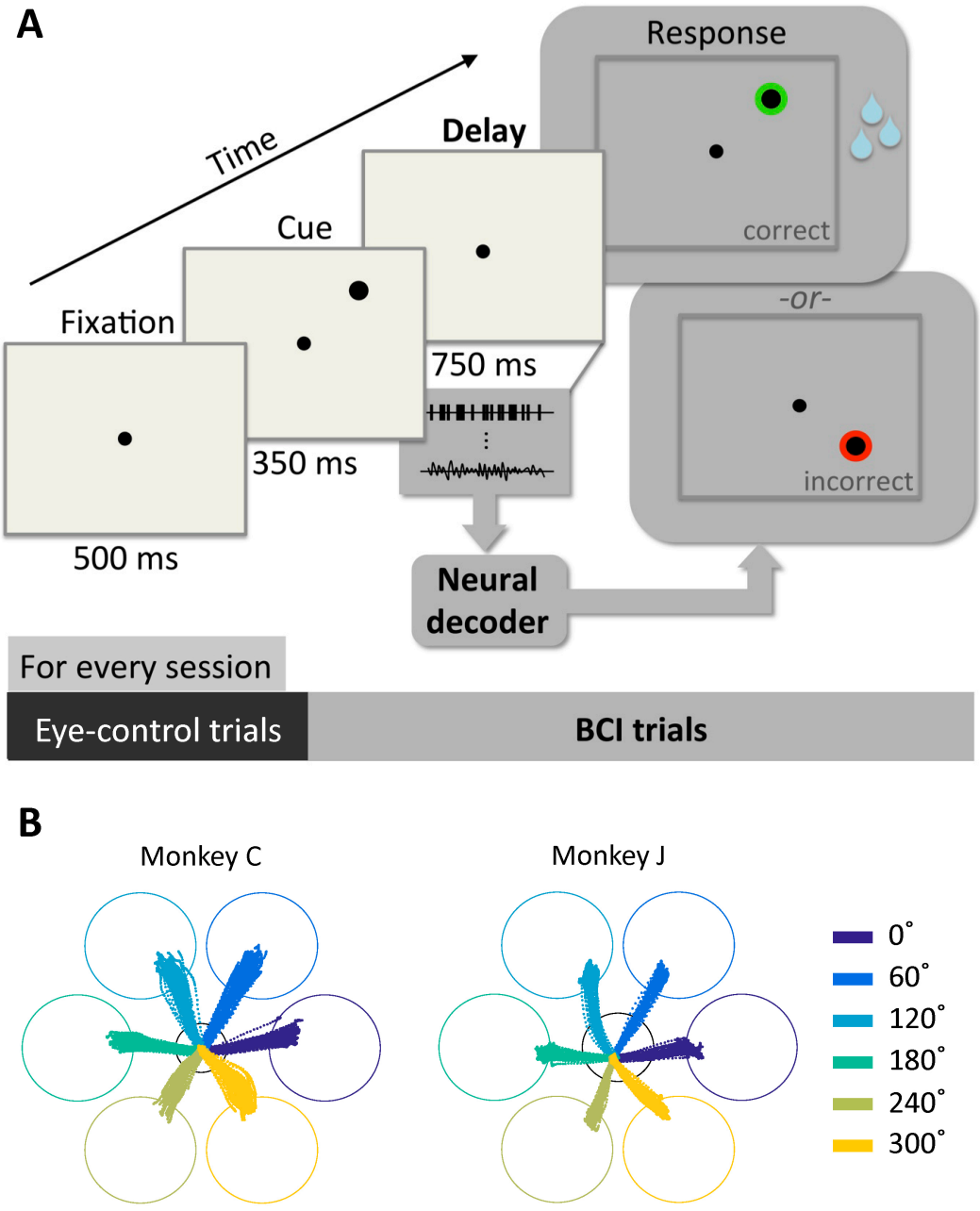

Figure 2.2. **BCI paradigm and decoding scheme.** A: BCI paradigm. Each trial was initiated by central fixation. A cue randomly chosen from 6 possible locations appeared briefly on screen, followed by the delay epoch, during which the monkeys must hold the target location in working memory and neural signals were collected. The response epoch differed depending on the trial type. During eye-control trials, monkeys had to make saccades to the correctly remembered target location to receive liquid reward. If that

happened, a green highlight was then placed at the correct target location along with the correct target. If monkeys made saccades to a wrong target location, a red highlight was placed at that incorrect target location along with the incorrect target, followed by a 3-second time-out. During BCI-control trials, a neural decoder instead selected the target location and drove the same feedback as in the eye-control trials. Every session consisted of 600 (for monkey C) or 300 (for monkey J) successfully performed eye-control training trials before the BCI trials were initiated. Epoch durations are given in milliseconds below panels. B: saccade trajectories during eye-control trials. Taken from 1 session for each monkey, color-coded by the cued target locations.

In the first phase, eye-control trials, the monkeys performed a saccade to the target location held in memory when the fixation dot was removed. Saccade trajectories from example sessions for both monkeys are shown in figure 1B, color-coded by the cued target locations. In our experiments, both monkeys completed their saccades typically in less than 20 ms from saccade initiation. If the saccade was made to the cued location, the target was presented with a green highlight and a water reward was delivered. If the saccade was made to any other location (which happened very rarely in practice), the chosen target was presented with a red highlight, and reward was withheld. 600 successful eye-control trials were required in the first phase for monkey C before progressing to the BCI-control trials phase.

Once the required number of eye-control trials had been successfully performed, a decoder was trained using data gathered from successfully performed eye-control trials with known saccade targets, and the session entered the BCI-control phase. The BCI-control trials of the task were similar to eye-control trials, except that target selection and the resulting reward were controlled by a neural decoder that predicted intended saccade

location based on delay period neural activity. During BCI-control trials, monkeys were allowed to move their eyes freely following the disappearance of the fixation dot and/or the display of the BCI-chosen saccade direction. Reward was contingent only on decoder output. In other words, the trained decoder came 'online' and replaced overt eye movements for target selection in the BCI-control trials. Subsequent offline analysis indicated that eye-control trials in excess of 300 did not result in substantial performance improvement for decoder training (average offline decoding accuracy of 10 sessions for 300 training trials: 67.81%, 400 trials: 69.66%, 500 trials: 69.96%, 600 trials: 70.66%, combined for both monkeys, using linear discriminant analysis decoder described below). Therefore only 300 eye-control trials were used for monkey J. Both monkeys were given the same number of total trials per session. Since the number of eye-control trials differed (600 for monkey C, 300 for monkey J), the number of BCI-control trials per session differed, and was at least 700 for monkey C, and 1000 for monkey J.

2.2.3.Neural signal processing

Recording. From each electrode, we acquired both threshold-crossing spike waveforms and LFPs using a multichannel data acquisition system (Cerebus, Blackrock Microsystems). Spiking thresholds were set manually for each channel, and a spike was registered if the voltage trace crossed the threshold. LFPs were extracted with a fourth order Butterworth low-pass filter with a cut-off frequency of 500 Hz and recorded at 1 kHz. The choice of a relatively high cut-off frequency (500 Hz, compared to LFP cut-off frequencies of 200-300 Hz or lower in many studies) was motivated by pilot findings of

significant saccade direction information in the 200-500 Hz range. Eye movements were monitored using an infrared eye tracking system (EyeLink 1000, SR Research) at a sampling rate of 1 kHz.

Online BCI paradigm. Electrode signals to be used for online decoding were collected during the first 720 ms of the delay epoch of the paradigm, leaving the final 30 ms of the delay epoch to allow for transformation of the electrical signals into decoder input and transmission of the decoder output to the computer display. High-frequency LFP was extracted online in Matlab (MathWorks) for every channel, by first performing common average referencing for each array, then applying a third order Butterworth bandpass filter with a passband from 80 to 500 Hz. Each channel's band-passed LFP was transformed to provide inputs to the decoder by simply summing its magnitude (absolute value) across the 720 ms recording period. The 80-500 Hz range was chosen based on pilot results from monkey C, which indicated that this range provided the most information for decoding of intended eye movement direction. After completion of eye-control trials at the start of each session, channels selection was performed to help determine the most useful channels and reduce dimensionality of the input data structure for the decoder, using one-way analysis of variance (ANOVA, $p < .05$) with respect to saccade directions on data collected during eye-control trials, and only these channels were used for decoding the intended saccade target for the rest of the session, as offline analysis indicated that channel selection with ANOVA generally helped decoder performance for a variety of inputs and decoders (unpublished observation).

Offline neural measure comparison. In addition to the online BCI, a number of offline analyses were performed in order to compare different measures derived from the recorded electrical signal during the first 720 ms of the delay period as potential decoder inputs. A total of 11 measures were extracted from the recorded neural signals, grouped into three signal types: continuous LFP magnitude measures; discrete, spike-related measures based on threshold crossings and waveform shapes; and hybrid measures that combine the continuous and discrete measures.

Continuous LFP magnitude measures were extracted from 6 different commonly studied frequency bands: 1-4 Hz (delta), 4-8 Hz (theta), 8-13 Hz (alpha), 13-30 Hz (beta), 30-80 Hz (gamma), and 80-500 Hz (including high gamma[2]). To calculate the LFP magnitude measure for each frequency band, the recorded electrical signals were filtered with a third order Butterworth bandpass filter with corresponding frequency bands, then the magnitudes of the filtered LFP signals were summed over the delay period to form one decoder input per recording channel. The LFP signal magnitudes were then log-transformed to obtain a more Gaussian-like distribution of inputs to the neural decoders described in the next subsection.

Three different discrete measures were obtained from the detected threshold crossing waveforms. To obtain single-unit (SU) spike counts for each electrode, the waveforms

[2] Much of the literature on high gamma band utilizes an upper bound anywhere between 150 Hz and 250 Hz rather than the broader 80-500 Hz band utilized herein. For this reason we use the term *high frequency LFP* to refer to the 80-500 Hz signal rather than high gamma.

were manually sorted offline into single units using principal component analysis (Plexon Offline Sorter). Individual electrodes were found to have between 0 and 4 single units. Spike counts during the delay period for all detected single units acted as input to the SU decoder. Some threshold-crossing waveforms did not satisfy waveform shape and/or cluster distinctness requirements for identification as a distinct single unit. These waveforms, termed *un-isolable spikes*, were included in a second discrete signal measure that augmented SU spike counts with a count of non-isolable spikes for each electrode. This measure will be referred to as SU+. Finally, multi-unit (MU) spike counts were formed for each electrode by summing all threshold-crossing waveforms occurring on that electrode (essentially pooling together all SU and non-isolable spikes).

In addition to these continuous and discrete measures, two hybrid measures were analyzed. Both utilized LFP magnitude in the 80-500 Hz range since this range was shown to provide the best decoding performance of the continuous measures. For the first hybrid measure, the continuous measure for each electrode was supplemented with SU spike counts for each identified SU. For the second hybrid measure, the continuous measure was supplemented with MU spike counts for each electrode.

For each signal measure, an ANOVA ($p < .05$) was applied to select channels to be used as input, and a leave-one-out cross-validation procedure was used to characterize the accuracy of an LDA decoder (described below) using the selected channels as input to the decoder. The first 300 eye-control trials were used for this analysis, in which 299 trials

were used to train the decoder and the remaining trial was used to test it. This procedure was repeated 300 times (omitting a different trial from the training set each time), and decoder accuracy was computed as the average percentage of correctly decoded trials across these 300 iterations.

Spectrotemporal analysis of saccade direction information. To obtain a finer-grained analysis of the spectrotemporal contents of LFPs on different electrode channels, we used multi-taper methods (Bokil *et al.*, 2010) to compute a spectrogram for each channel during the delay period of each eye-control trial. Multi-taper parameters were: 5 tapers, half time-bandwidth product of 3 (TW = 3), and window size of 500 ms stepped every 20 ms. The explained variance by intended saccade direction for each time-frequency point of the spectrogram was then computed with a one-way ANOVA as a measure of the information about saccade direction in time-frequency resolved neural signals.

2.2.4. Decoders

Online BCI paradigm. The 80-500 Hz LFP magnitude signals measured during training trials were first used to identify electrode channels containing information about intended saccade direction (one-way ANOVA on delay-period activity, with respect to the cued saccade target directions; $p < .05$). The 80-500 Hz LFP magnitude on these p significant channels was then used as training data to compute the probability that observed p-dimensional data vectors $X = (x_1, \ldots, x_p)$ on each test trial belonged to each possible class (target direction). These probabilities were computed using a linear discriminant

analysis (LDA) classifier (or decoder), which assumes neural activity for each class approximates a multivariate Gaussian distribution with a class-specific mean μ_k, but common covariance structure Σ across $k = 1, \ldots, 6$ target directions (Hastie, Tibshirani and Friedman, 2001):

$$P(X|k) = \frac{1}{\sqrt{(2\pi)^p |\Sigma|}} e^{\left(-\frac{1}{2}(X-\mu_k)^T \Sigma^{-1} (X-\mu_k)\right)}.$$

Estimates of the Gaussian means μ_k and the covariance matrix Σ were calculated from training trials. On validation trials, the saccade direction with the highest probability $P(X|k)$ was selected as the decoder's estimate $\hat{y}$ of the intended saccade direction. Note that, because target direction had uniform probability $P(k)$ and the normalization constant $P(X)$ is the same for all directions, this decision rule is identical to selection based on the posterior probability using Bayes Theorem:

$$P(\hat{y} = k|X) = \frac{P(X|k)P(k)}{P(X)}.$$

Selecting the direction with the highest posterior probability is equivalent to selecting the predicted class based on log likelihood ratios as is typically done in LDA. Thus for our decoding purpose, this is an equivalent formulation as the classical LDA. LDA variants have been previously used offline to decode reaching directions (Mehring *et al.*, 2003) and saccade directions (Pesaran *et al.*, 2002; Boulay *et al.*, 2015). An LDA decoder was chosen for the current BCI because of its simplicity, computational efficiency, and optimal performance based on pilot results from monkey C.

Offline decoder comparisons. To confirm that our conclusions were not dependent on the specific decoder used, we also performed offline analyses comparing LDA to four other decoders: naïve Bayes classification, linear regression, artificial neural network classification, and artificial neural network regression.

Like LDA, a Naïve Bayes classifier computes the posterior probability of each class (saccade target), selecting the class with the highest posterior probability (Mehring *et al.*, 2003). However, it makes a distinct set of assumptions—that all features approximate Gaussian distributions with class-specific means and variances (loosening the common covariance assumption of LDA), but are independent from each other (i.e., zero covariance):

$$P(X|k) = \prod_{i=1}^{p} \frac{1}{\sqrt{2\pi\sigma_{ik}}} e^{-\frac{(x_i-\mu_{ik})^2}{2\sigma_{ik}^2}}.$$

Estimates of the Gaussian mean μ_{ik} and variance σ_{ik} for $k = 1, \ldots, 6$ target directions and for each feature i were calculated from training trials. As with LDA, on validation trials the target direction with the highest posterior probability was selected as intended saccade direction.

Linear regression decoding has been applied in several prior BCIs (Wessberg *et al.*, 2000; Hochberg *et al.*, 2006), and provides a continuous output, unlike the discrete classifiers described above. Regression coefficients mapping neural activity to the horizontal and vertical components of saccade target directions were estimated from eye-control trials

using least squares:

$$B_h = (X^T X)^{-1} X^T y_h$$

$$B_v = (X^T X)^{-1} X^T y_v$$

where X represents the neural signal used as input and the y's represent the horizontal ($y_h = \cos\theta$) and vertical ($y_v = \sin\theta$) components of the saccade direction θ. On validation trials, these coefficients were used to decode a continuous saccade direction:

$$\hat{\theta} = \tan^{-1}(\hat{y}_v/\hat{y}_h), \qquad \hat{y}_v = XB_v, \qquad \hat{y}_h = XB_h$$

which was then discretized into the nearest one of the six possible target directions.

Artificial neural networks (ANN) have been successfully used to decode direction of intended movement in the reaching literature (Wessberg *et al.*, 2000; Hatsopoulos, Joshi and O'Leary, 2004). Here we tested both a discrete-output ANN that classified each saccade direction as a distinct class (ANN-c), and a continuous-output ANN that similarly decoded the horizontal and vertical components of saccade target directions like the regression decoder described above (ANN-r), both using a fully connected 3-layer feed-forward network consisting of one input layer, one hidden layer, and one output layer. The input layer consisted of nodes representing selected neural measures as input for the network. The hidden layer contained the same number of nodes as the input layer, each computing a weighted sum across input nodes (where x_i is the activation of the *i*th input node, and w_{ij} is the connection weight from input node i to hidden node j):

$$z_j = \sum_{i \in \text{input}} x_i w_{ij}$$

Then passing its output through a logistic activation function:

$$y_j = \frac{1}{1 + e^{-z_j}}$$

The output layer differed between ANN-c and ANN-r decoders. For ANN-c, the output layer consisted of six output nodes with logistic activation functions, each representing one of the six saccade target directions, and the network was trained using the cross entropy loss function:

$$L = -\frac{1}{N}\sum_{n=1}^{N}\sum_{k=1}^{6}[y_{n,k}\, log\, \hat{y}_{n,k} + (1 - y_{n,k})\, log(1 - \hat{y}_{n,k})]$$

Where $\hat{y}_{n,k}$ represents the k^{th} (out of 6 directions) output node's activation level for the n^{th}(out of N) training sample, and $y_{n,k}$ represents the desired output (1 if the node represents the correct saccade direction, 0 otherwise). For ANN-r, the output layer consisted of 2 nodes with linear activation functions, representing the horizontal and vertical components of the saccade direction. The ANN-r network was trained using the sum of squared error loss function:

$$L = \frac{1}{2}\sum_{n=1}^{N}\sum_{a=1}^{\{horiz.,vert.\}}(y_{a,n} - \hat{y}_{a,n})^2$$

Where $\hat{y}_{a,n}$ is the activation level of the a^{th} output node (representing either the horizontal-axis or vertical-axis component) corresponding to the i^{th}(out of N) training sample, and y_{an} represents the desired output.

Both ANN-c and ANN-r were trained using backpropagation in conjunction with

conjugate gradient descent optimization, during which errors were propagated throughout the neural network according to their respective loss functions. For ANN-c, intended saccade direction was decoded as the output node with the highest activation level in the output layer, while for ANN-r intended saccade direction was computed from its horizontal and vertical components, and then discretized into the nearest one of the six possible target directions.

Two versions of each decoder type were trained: one using the magnitude of the LFP in the 80-500 Hz frequency range, and one using the SU+ spike counts. Only channels with saccade direction information (one-way ANOVA, $p < .05$) in training trials were used as inputs for decoders. A leave-one-out cross-validation procedure using the first 300 eye-control trials was applied to characterize the accuracy of each of the 10 resulting decoders (5 decoder types x 2 input types), and decoder accuracy was computed as the average percentage of correctly decoded trials across these 300 iterations.

2.2.4. Mutual information.

In addition to decoding accuracy, we also evaluated decoder performance using the mutual information (MI) between the decoder-predicted and actual saccade directions. MI measures how much information the decoder predictions $\hat{Y}$(including both correct and incorrectly decoded ones) can provide about true saccade directions Y. The entropy of the actual saccade direction distribution Y is:

$$H(Y) = -\sum_{k=1}^{6} P(y = k) \log_2 P(y = k)$$

And the entropy of the actual saccade direction distribution Y conditional on decoded saccade direction distribution $\hat{Y}$ is:

$$H\left(Y\middle|\hat{Y}\right) = -\sum_{k=1}^{6}\sum_{c=1}^{6} P(\hat{y} = c, y = k) \log_2 \frac{P(\hat{y} = c)}{P(\hat{y} = c, y = k)}$$

Finally, the mutual information between Y and $\hat{Y}$ is:

$$MI\left(Y, \hat{Y}\right) = H(Y) - H(Y|\hat{Y})$$

MI is measured in bits, and for our six-class paradigm ranges from 0 to $\log_2 6 \approx 2.58$ bits. All probabilities were computed directly from the empirical data values.

To illustrate the distinction between decoding accuracy and MI, suppose we have a 2-direction decoding task, and one hypothetical decoder can achieve 50% accuracy if it outputs the same direction all the time, without knowing anything about the data. Its MI would be 0 bits, indicating that it provides no information about the true direction. On the other hand, if another hypothetical decoder always predicted the direction opposite of the correct one, it would have a decoding accuracy of 0%, but its MI would be 1 bit, indicating a perfect relationship (anti-correlation) between the decoded and the true directions. Comparing the MIs between these two hypothetical decoders reveals that the second one had knowledge of the underlying data structure (albeit completely flipped from the true one). In this extreme toy example, the MI provides a more accurate assessment of the decoders from the perspective of model validation, and can serve as a

useful complementary measure for decoder comparison. In practice, we found that MI and accuracy provided essentially identical results.

2.2.5. Comparison of saccade information in different brain regions. To assess how much each brain region (FEF, SEF, PFC) contributed to decoder performance, we performed offline analyses in which LDA decoders were generated for each brain region separately. For each brain region, decoders were constructed for each of the 6 continuous and 3 discrete neural measures described above. To assess whether delay-period results generalized to the peri-saccadic period, this analysis was carried out separately using data from: (i) the first 720 ms of the delay epoch, and (ii) 100 ms before to 100 ms after saccade onset. A leave-one-out cross-validation procedure using the first 300 eye-control trials was applied to characterize the accuracy of each decoder for each brain region in each epoch. Unlike previous analyses, no channel selection using ANOVA was performed since it would result in no usable channels for some areas (for instance area FEF in monkey C did not always have usable spikes during some sessions due to its low unit count). All channels were provided to the LDA decoders.

2.3. Results

2.3.1. Online BCI performance

Prior to the BCI sessions, both monkeys were proficient at the memory-delayed saccade task and were at near-perfect performance. Therefore, any incorrectly decoded trials were attributed to decoder error rather than behavioral error on the part of the monkey. Based

on pilot results from monkey C, we determined that LFP power in the 80-500 Hz range was likely to provide the most informative neural measure for decoding purposes (see related analyses in next subsection). This measure was thus used for online performance in the BCI sessions.

The decoding accuracies for 10 consecutively recorded BCI sessions were 61.46% with SD ± 6.48%, MI 1.03 ± .19 bits for monkey J, and 71.84 ± 3.24%, MI 1.42 ± .11 bits for monkey C, both highly above chance (16.67%). Since both monkeys received implants unilaterally, we expected BCI performance to be better for targets in the visual field contralateral to the implant due to a stronger contralateral visual representation in the implanted areas of frontal cortex (Bruce *et al.*, 1985; Sawaguchi and Iba, 2001; Kagan *et al.*, 2010). Figure 3 shows the breakdown of decoding accuracy for targets in contralateral and ipsilateral visual fields. Monkey J received implants in the right hemisphere, and decoding accuracy for contralateral targets was 76.64 ± 6.91%, while ipsilateral target decoding accuracy was 46.53 ± 13.55%. Monkey C received implants in the left hemisphere, with contralateral decoding accuracy of 87.7 ± 2.05% and ipsilateral decoding accuracy of 55.95 ± 5.3%. Contralateral targets had significantly higher decoding accuracies than ipsilateral targets for both monkeys (monkey C: $p = .002$, monkey J: $p = .002$, two-sided Wilcoxon signed-rank test). The confusion matrices in figure 3 show that the decoders tended to confuse targets in the ipsilateral visual field for both monkeys. For instance, 240º target for monkey C was usually confused with 180º

target by the decoder, and 60º target was confused with 0º target by the decoder for monkey J.

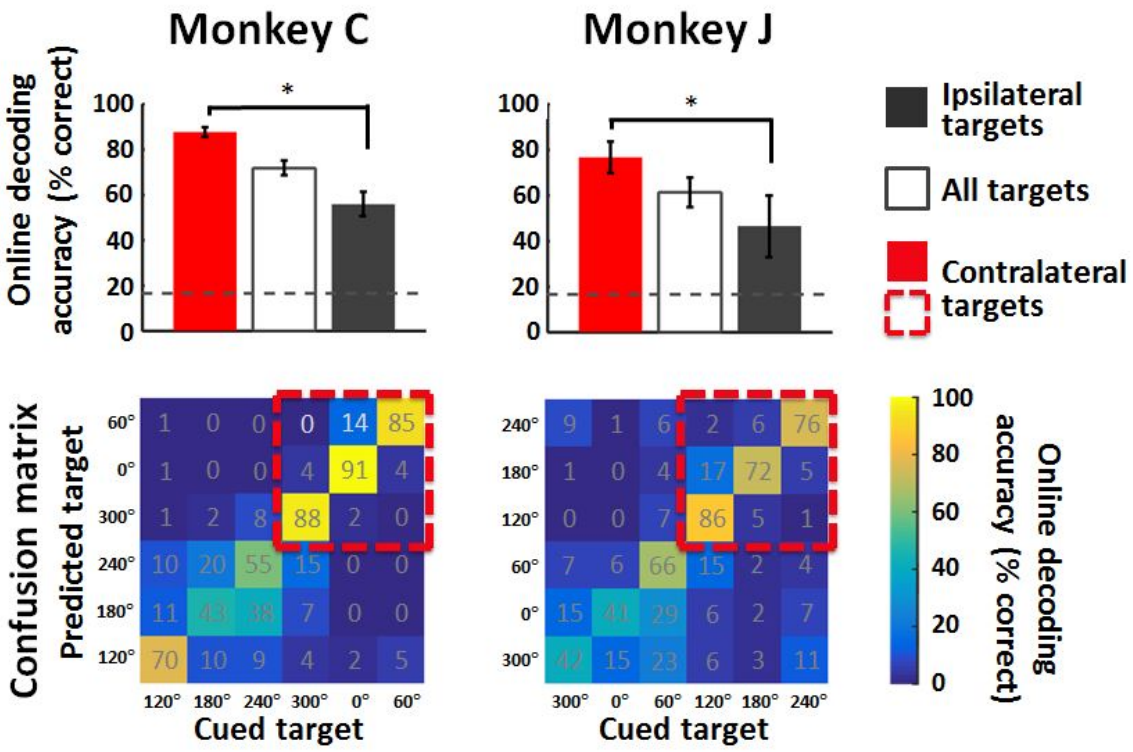

Figure 2.3. BCI performance summary. Top row: average BCI performance for contralateral and ipsilateral targets across all 10 sessions, as well as all targets combined, for each monkey. Decoding accuracies of contralateral targets are significantly higher than ipsilateral targets, indicated by a star. Dashed line indicates chance level accuracy. Bottom row: confusion matrices for all six targets, for each monkey, with contralateral targets highlighted in dashed red line, and the number of trials for each cued-predicted target pairs are labeled in gray.

To quantify the effect of practicing on BCI performance, we compared decoding accuracy during the early BCI phase with the late BCI phase of the same session. Trials from the first 25% of the BCI phase were extracted, and their online decoding accuracies were computed and compared with trials from the last quarter of the BCI phase in that session, for all sessions. Monkey J performed better during the beginning of the BCI

phase (early: 73.29 ± 5.96%, late: 52.16 ± 7.46%, p = .002, two-sided Wilcoxon signed-rank test), while monkey C's performances remained stable over the BCI phase (early: 71.36 ± 4.92%, late: 71.91 ± 3.73%, p = .56, two-sided Wilcoxon signed-rank test). For both monkeys, decoding accuracies per session were not significantly worse during earlier sessions compared to later sessions (average difference of online decoding accuracies between the first and last 3 sessions for monkey C: 4.5%; monkey J: -1.76%).

2.3.2. Effect of practice

To investigate the effect of practice on BCI performance, we compared online decoding accuracy during the early BCI phase with the late BCI phase of the same session. The first 25% of BCI-control trials were extracted, and their online decoding accuracies were compared with performance of trials from the last 25% of the BCI-control trials within session, for all sessions. Monkey J performed better during the early BCI phase (early: 73.29 ± 5.96%, late: 52.16 ± 7.46%, p = .002, two-sided Wilcoxon signed-rank test), while monkey C's performances remained stable over the BCI phase (early: 71.36 ± 4.92%, late: 71.91 ± 3.73%, p = .56, two-sided Wilcoxon signed-rank test). This difference in performance stability is likely related to the change in neural signals within the same session. High-frequency LFP signals from channels selected for decoder input changed by 1.97 ± 1.69% on average from early to late BCI phase for monkey C, while the signal changed by 3.16 ± 3.75% on average for monkey J. The signal drift of monkey J was significantly more pronounced than that of monkey C ($p << .01$, two-sided Wilcoxon rank sum test), and likely contributed to its performance decrease within the same session. For both monkeys, decoding accuracies were not significantly worse

during earlier sessions compared to later sessions (average difference of online decoding accuracies between the first and last 3 sessions for monkey C: 4.5%; monkey J: -1.76%).

Inspection of eye movement traces revealed that monkey C gradually stopped making overt saccades to the cued location during BCI-control trials, while monkey J continued to produce overt eye movements in BCI-control trials even though these movements were not required to obtain reward. This difference is likely due to a slight paradigm difference between the two monkeys: the fixation dot remained on after the end of the delay epoch for monkey J (though fixation maintenance was not required), while for the second monkey the fixation dot promptly disappeared at the end of the delay epoch and there was a longer delay until reward feedback.

2.3.3. Neural measure comparison

The BCI literature has not reached a consensus regarding which measures of neural signals work best for decoding purposes. Studies using single-unit (SU) spikes, multiunit (MU) spikes, and LFPs have all shown promising results (Pesaran *et al.*, 2002; Mehring *et al.*, 2003; Zhuang *et al.*, 2010; Markowitz *et al.*, 2011; So *et al.*, 2014). To compare neural signal types in the current BCI paradigm, we calculated leave-one-out cross validation accuracies in offline analysis, for LDA decoders trained using 11 different signal measures, including LFP power in 6 frequency bands: 1-4 Hz (delta), 4-8 Hz (theta), 8-13 Hz (alpha), 13-30 Hz (beta), 30-80 Hz (gamma), and 80-500 Hz (including high gamma); 3 spike-related measures: firing rates of sorted SU spikes (referred to as

SU), sorted SU spikes supplemented by non-isolable spikes that did not satisfy waveform shape and/or cluster distinctness requirements to be identified as a distinct single unit (referred to as SU+), all spikes pooled together for each electrode (referred to as MU); and two hybrid measures that combine LFP and spike components: 80-500 Hz and SU+, 80-500 Hz and MU. Analyses were restricted to eye-control trials to avoid potential signal changes from monkeys adapting to the BCI paradigm. Qualitatively similar results were obtained for both monkeys; their decoder accuracies were combined in the analyses presented here.

Table 2.1 indicates the number of identified single units in each implanted area for each monkey. There are large differences between the number of isolated single units on each array and subjects. PFC contained the highest number of single units in monkey C, while for monkey J it was SEF. Offline decoder accuracies using LDA for all 11 signal measures are summarized in figure 4. Among the LFP measures tested, 80-500 Hz band power had the highest leave-one-out cross validation accuracies (82.32 ± 4.52%, MI 1.79 ± .15 bits), significantly higher than any other continuous or discrete measures ($p << .01$ for all pairs, two-sided Wilcoxon signed-rank test). For the spike-related measures, SU+ had the highest decoding accuracies (62.02 ± 14.44%, MI 1.11 ± .42 bits), and statistical comparison of SU+ with SU revealed that decoding accuracies were significantly higher ($p << .01$, two-sided Wilcoxon signed-rank test) when non-isolable spikes were included, as in the SU+ measure. Hybrid models that combined 80-500 Hz LFP with either SU+ or MU had decoder accuracies that were nearly identical to decoder accuracy when using

only the 80-500 Hz LFP band ('80-500 Hz LFP / SU+': 82.29 ± 6.39%, MI 1.79 ± .21 bits, '80-500 Hz LFP / MUs': 82.32 ± 5.66%, MI 1.79 ± .20 bits), suggesting that any additional information from spike-related measures was largely if not completely redundant with information in the 80-500 Hz LFP measure.

	PFC	SEF	FEF
Monkey C	33.1 ± 3.04	4 ± 0.94	0.5 ± 0.97
Monkey J	3.5 ± 1.08	42.2 ± 2.97	5.5 ± 1.65

Table 2.1. Daily single-unit counts in each implant region. Counts are summed over all electrodes on the same array, and averaged across sessions.

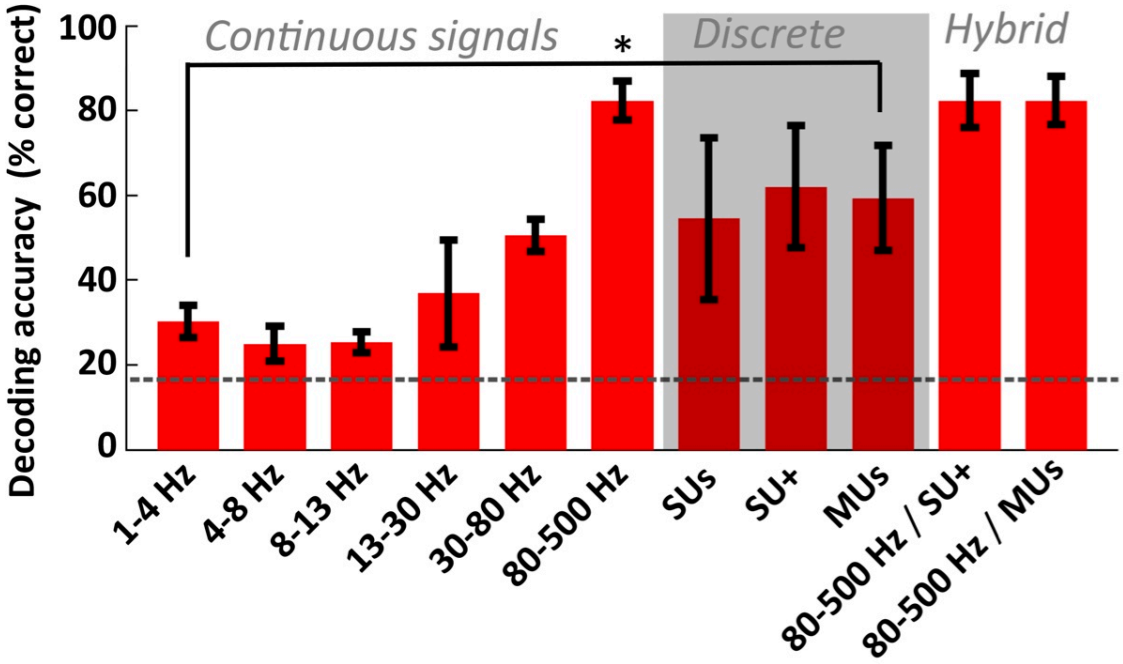

Figure 2.4. Offline decoding performance comparison of 6 continuous, 3 discrete, and 2 hybrid neural activity measures. Analysis is restricted to eye-control trials to avoid signal changes caused by monkeys adapting to the BCI paradigm. Leave-one-out cross validation accuracies were computed with an LDA decoder. Results are combined for both monkeys, 10 sessions per monkey. Continuous signals are the raw magnitudes of the given frequency bands. Discrete signals consist of three types of firing rates: 'SU', firing rates of sorted single-units only; 'SU+', firing rates of single-units, augmented with the rate of all un-isolable threshold-crossing spikes as a distinct decoder input; 'MU', firing rate of multiunits (all threshold-crossing spikes on the same electrode). Hybrid signals combine continuous and discrete measures: '80-500 Hz / SU+', high-frequency LFP and SU+; '80-500 Hz / MU', high-frequency LFP and MU. Dashed line indicates chance level accuracy. Decoding accuracy of the 80-500 Hz band is significantly higher than all other signals ($p << 0.01$, two-sided Wilcoxon signed-rank test) except hybrid signals.

2.3.4. Decoder comparison

The analyses described thus far utilized LDA decoders. To ensure that our results are not specific to the decoder used, in additional offline analyses we compared performance of LDA decoders to four other decoder types: discrete artificial neural network classification

(ANN-c), continuous artificial neural network regression (ANN-r), naïve Bayes, and linear regression decoders. Figure 2.5 summarizes each decoder's accuracy using the 80-500 Hz LFP signal (left panel) and SU+ spike count signal (right panel), and table 2 shows the corresponding mutual information values. Among different signal types, 80-500 Hz LFP performed the best for all five decoders, indicating that it is a robust and informative signal, independent of the specific choice of decoder.

Of the five decoders tested, LDA consistently performed best for both continuous and discrete signals. While this is consistent with previous results showing optimal performance of simple linear models in decoding neural spiking data (Meyers and Kreiman, 2011) we do not wish to make any general claims about the optimality of LDA. It might be the case, for example, that larger training datasets (compared to our few hundred trials) might support more complex, nonlinear models. Our results do suggest that LDA—which is simple and computationally inexpensive—produces reasonably good decoding accuracy with a relatively small number of training observations.

	Monkey C		Monkey J	
	80-500 Hz LFP	SU+	80-500 Hz LFP	SU+
LDA	1.74 ± .12	.72 ± .09	1.82 ± .16	1.50 ± .20
ANNd	1.62 ± .13	.64 ± .10	1.61 ± .16	1.42 ± .19
ANNc	1.37 ± .14	.47 ± .10	1.26 ± .15	1.19 ± .19
Naïve Bayes	1.33 ± .19	.40 ± .07	1.32 ± .12	1.13 ± .16
Regression	1.58 ± .14	.69 ± .09	1.57 ± .15	1.37 ± .14

Table 2.2. Mutual information (bits) of different decoders for 80-500 Hz LFP, and SU+ inputs.

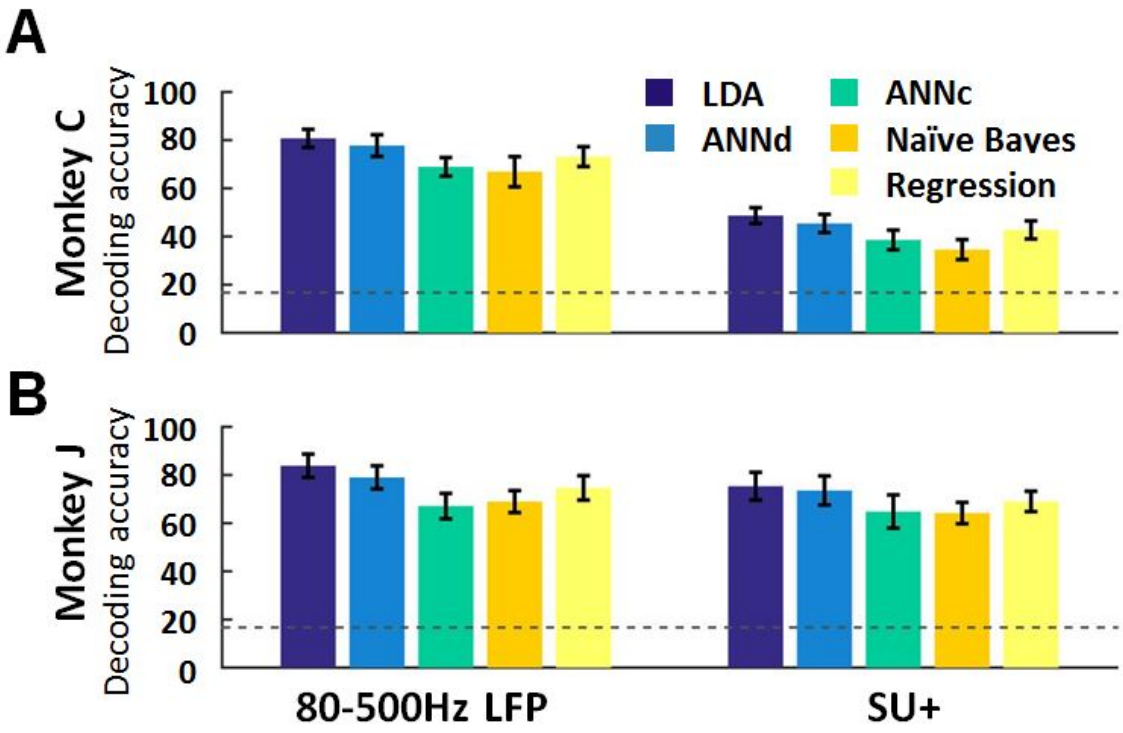

Figure 2.5. Offline decoding performance comparison of different decoders. Results from leave-one-out cross validation are shown separately for each monkey (A: monkey C; B: monkey J), 10 sessions per monkey. 80-500Hz LFP: 80-500Hz raw band power. 'SU+': firing rates of single-units, augmented with the rate of all non-isolable threshold-crossing spikes, as a distinct decoder input. Dashed lines indicate chance level accuracy.

2.3.5. Brain region comparison

To determine how saccade information is distributed across the brain regions studied here, LDA decoders utilizing signals from only one brain region (FEF, SEF, or PFC) were constructed and evaluated using leave-one-out cross-validation to compute decoder accuracy offline. Figure 2.6 provides the decoder accuracies for each of the 6 continuous and 3 discrete neural signal measures considered herein. Decoder accuracies provided in figure 2.6A are for data collected during the first 720 ms of the delay epoch; those in

figure 6B are for data collected during the 200 ms period centered around saccade initiation (response epoch). For monkey C, SEF provided the best decoding performance for all signal types, both during the delay epoch and the response epoch. For monkey J, SEF provided the best decoding performance for the three discrete signal measures, whereas FEF provided the best performance for the continuous signal measures; this was true for both the delay and response epochs.

The number of identified single-units appears not to correlate with the decoding performance of high-frequency LFP in each implant region. PFC and FEF in monkey J both have relatively few identified single-units (see Table 1), their decoding performances are worse than that of SEF when using discrete signals as input, but become equal or even better than SEF when using high-frequency LFP. This is also reflected in SEF in monkey C. Despite having much lower single-unit counts than PFC, SEF still outperforms PFC regardless of which input signal is used for monkey C.

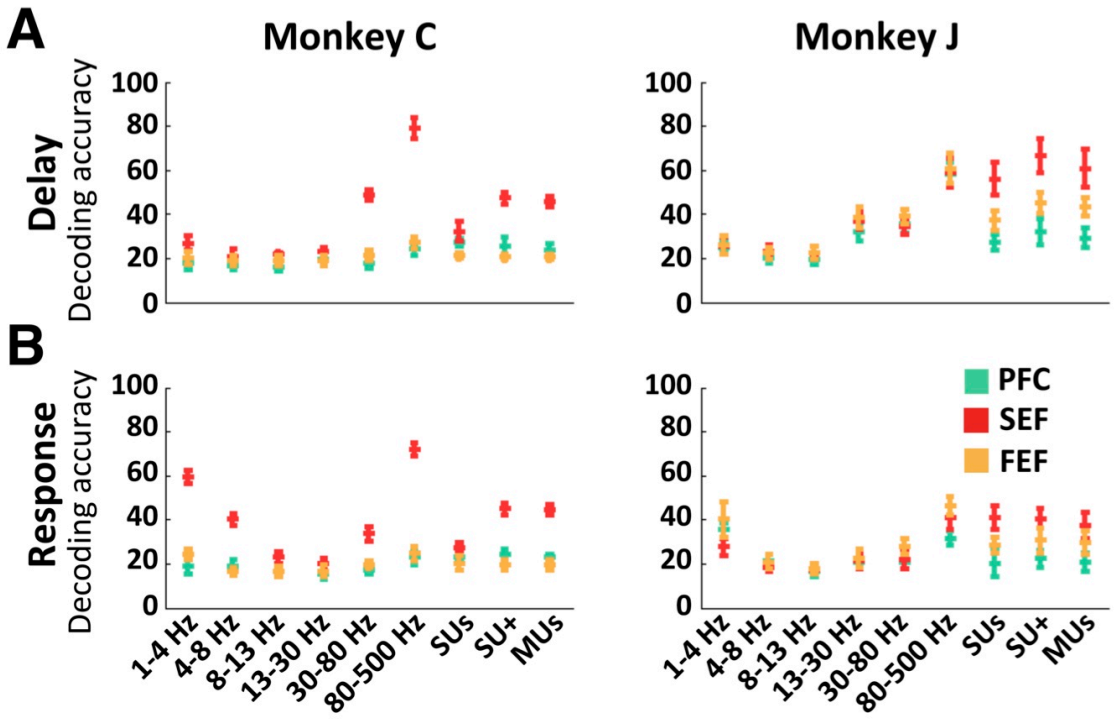

Figure 2.6. Offline decoding performance comparisons of implant regions during (A) the first 720 ms of the delay epoch and (B) the response epoch (100 ms before saccade onset to 100 ms after saccade onset), for different signal types. The first 300 trials during each session are used to obtain leave-one-out cross validation (decoding performance) for 9 signal types: 1-4 Hz band LFP; 4-8 Hz band LFP; 8-13 Hz band LFP; 30-80 Hz band LFP; 80-500 Hz band LFP; 'SU', firing rates of sorted single-units only; 'SU+', firing rates of single-units, augmented with the rate of all un-isolable threshold-crossing spikes, as a distinct decoder input; 'MU', firing rate of multiunits (all threshold crossings on the same channel, unsorted).

2.3.6. Spectrotemporal analysis of saccade direction information

To assess how saccade direction information is distributed across LFP frequency bands in different electrode channels, we computed spectrograms for each electrode channel during the delay period of each eye-control trial. We then performed a one-way ANOVA to determine how much of the variance in the spectrogram data can be accounted for by saccade direction at each frequency and time point. Figure 2.7 shows the explained

variance in the spectrograms of 4 example channels, with the first two panels corresponding to two electrode channels in monkey J and the last two panels to electrode channels in monkey C. Generally speaking, information about saccade direction appears to be spread across a broad frequency range, and different frequency ranges appear to encode information in different electrode channels. For example, the first channel from the left in Figure 2.7 has most of the explained variance about saccade direction in frequencies above 300 Hz, while the last channel has the highest explained variance roughly between 80 and 200 Hz, particularly toward the end of the delay epoch. These factors may explain why the broad 80-500 Hz range provided the best decoder performance of all the neural measures compared in Figure 2.4.

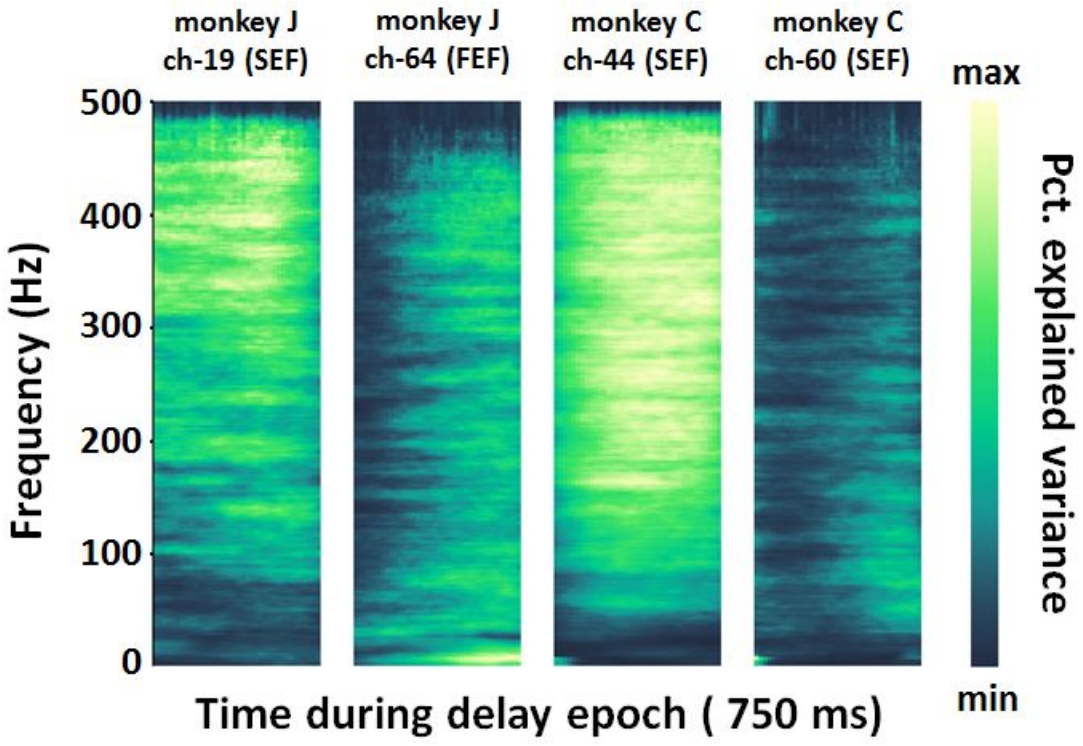

Figure 2.7. Saccade direction information during the delay epoch. The percent of variance explained by saccade direction in the spectrogram data of 4 example channels (2 from each monkey) are shown here. Time is plotted relative to start of delay epoch; the

entire delay epoch is plotted here. The ranges (minimum–maximum) of explained variances for all 4 spectrograms from left to right are: 0–18, 0–20, 0–30, and 0–10, respectively. Channel source from left to right: monkey J – channel 19 (SEF), monkey J – channel 64 (FEF), monkey C – channel 44 (SEF), monkey C – channel 60 (SEF).

2.3.7. Quantifying signal drift and behavioral degradation during BCI sessions

BCI performance may suffer if the subjects lose motivation, or if the signal quality degrades over the recording session. To break down these two potential confounds, we inspect the signal quality and each subject's effort at performing the task during the sessions.

To quantify how much effort each monkey is putting into the BCI session, we look at what percentage of presented trials were correctly executed during the sessions. Correctly executed trials are defined as trials that were successfully executed until end of the delay period during the BCI sessions (i.e., trials in which the monkey maintained fixation throughout the delay period), and trials with saccades to correct targets during the non-BCI sessions (only for monkey J; monkey C lacked control sessions for comparison). As mentioned before, the monkeys were at near perfect performance before the BCI sessions, therefore any incorrectly decoded trial was regarded as a mistake made by the decoder and not attributed to the monkey. If monkeys suffer no motivation loss, then the percentage of correctly executed trials should stay stable throughout the entire session. Figure 2.8 A and B show the sliding window average of percentage of correctly executed trials for each monkey, smoothed with a [-100 100] trials window for ease of visualization. For both monkeys, motivation seems to decline steadily towards session

end, indicating that they were indeed suffering from loss of motivation. Interestingly, monkey J appears to have tried harder in the BCI sessions than in the control sessions to acquire more reward (on average, percent of correctly executed trials are about 10% higher during BCI sessions than control sessions).

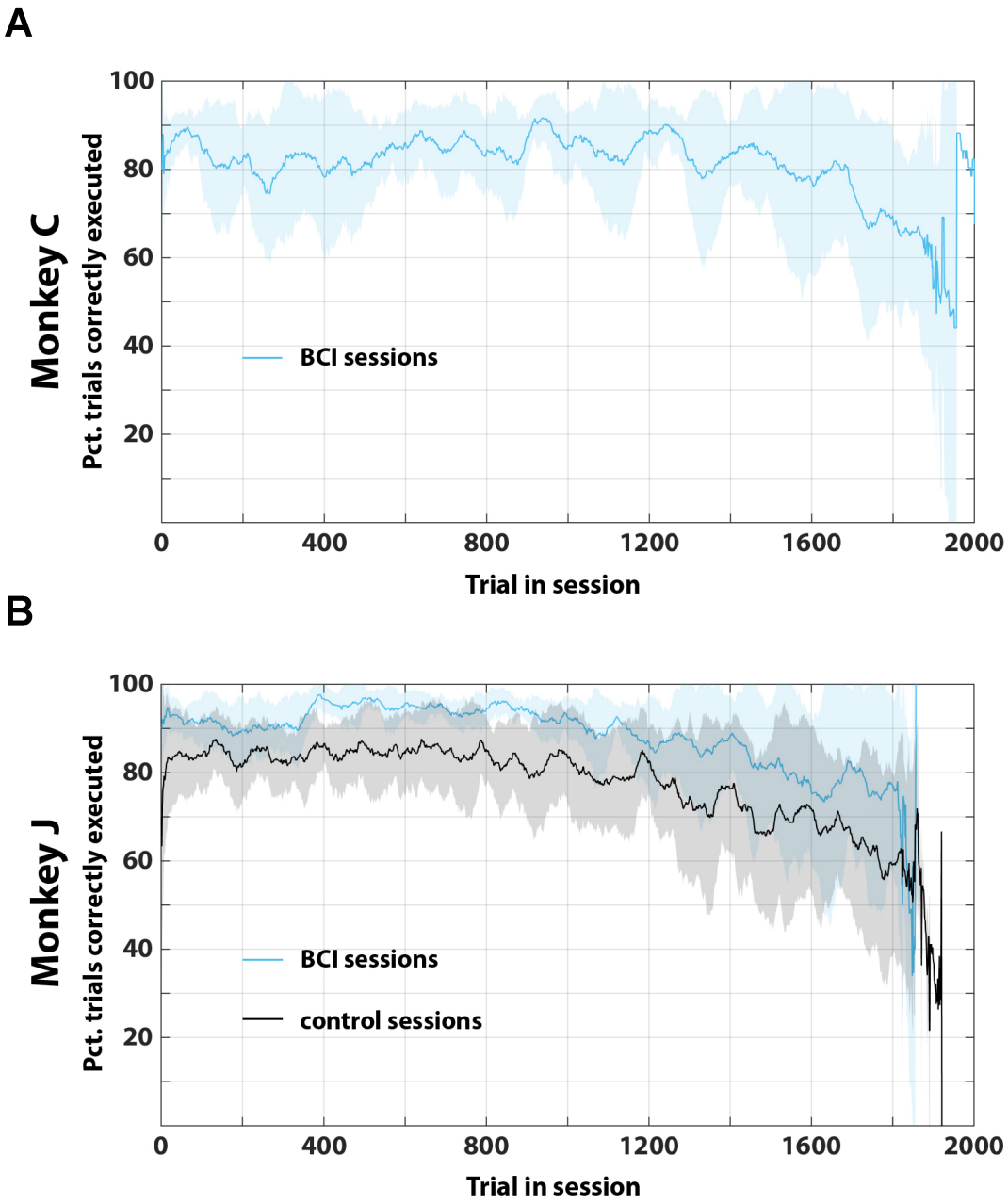

Figure 2.8. Behavioral performance in session for (A) monkey C, and (B) monkey J. Percent of correctly executed trials (successful fixation until end of the delay epoch) are plotted for all trials in session. Solid lines indicate mean percentage and shaded regions indicate standard error. Data are smoothed with a 51 trial window for ease of visualization. A: 10 consecutive BCI sessions are shown for monkey C (for lack of control sessions). B: 10 consecutive BCI sessions and 10 consecutive control sessions are shown for monkey J.

To estimate the effect of signal drift in parallel with motivation decline, a sliding window decoding analysis was applied to incorporate possible signal changes occurring during the recording session. An LDA decoder is re-built using the previous 300 correctly executed trials after every correctly executed trial. Using this adaptive LDA (termed ALDA) decoding scheme, the decoding performances are plotted in Figure 2.9 A and B for monkey C and J respectively, and smoothed over a [-100 100] trials window for ease of visualization.

Both monkeys saw a decoding performance boost using the adaptive approach, suggesting the presence of neural signal drift during the recording sessions. Monkey J's ALDA performance was on average 8.88 ± 3.70% better than the static decoding approach per session, and Monkey C's ALDA performance was on average 6.30 ± 3.30% better per session. Performance difference between ALDA and static decoders widens in the latter part of each session, indicating that the neural signal drift worsens within each session.

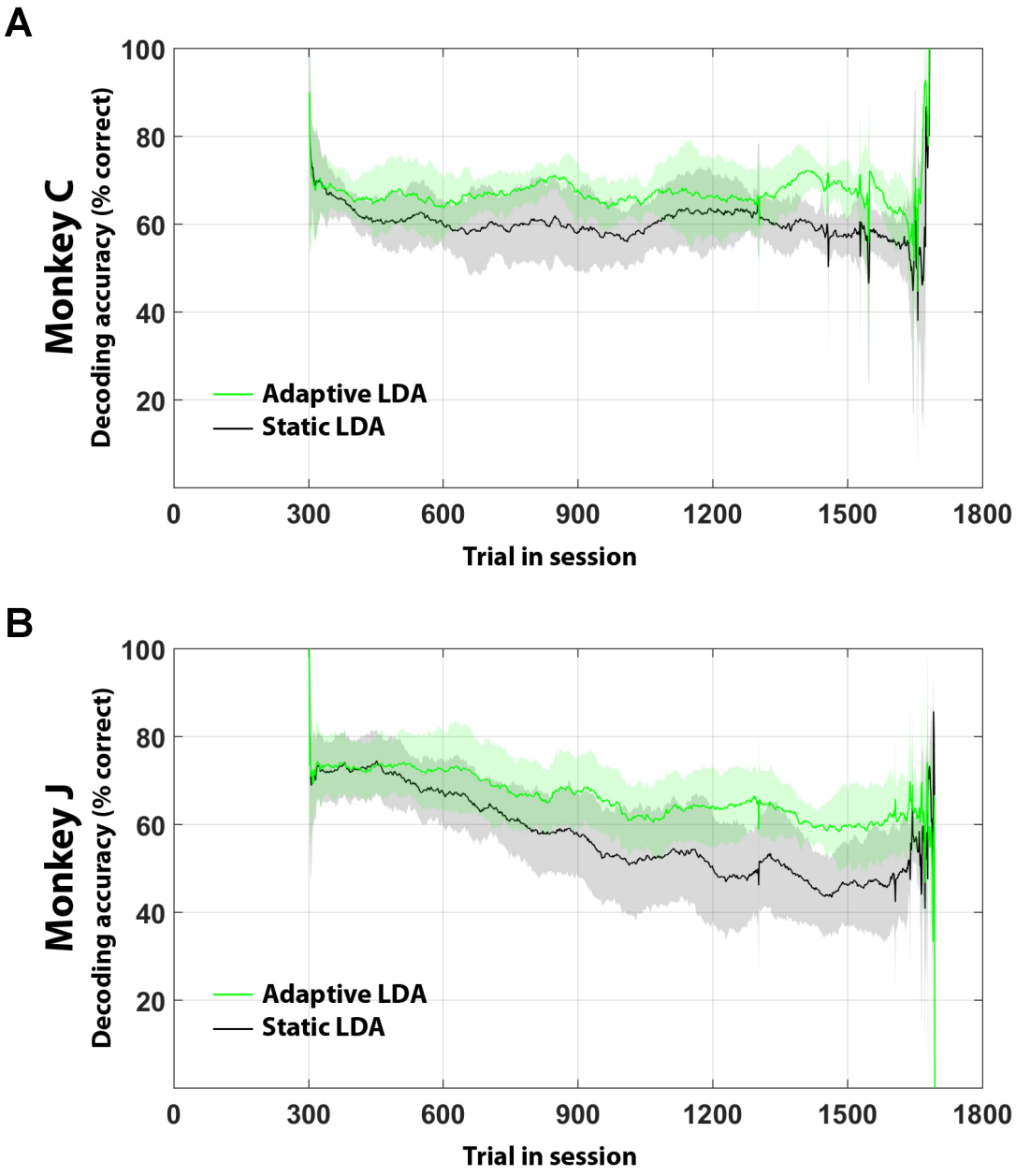

Figure 2.9. Performance comparison between adaptive decoding and static decoding for (A) monkey C, and (B) monkey J. Static decoding is the same as online BCI paradigm. Solid lines indicate mean percentage and shaded regions indicate standard error. Data are smoothed with a [-100 100] trials window for ease of visualization. 10 consecutive BCI sessions are shown for both monkeys.

2.3.8. Relationship between high-frequency LFP and multi-unit spikes

In addition to comparing decoding performances between LFP signals and discreet signals, we also compare the correlation in information contents between high-frequency LFP and multi-unit spikes on the same channel. Figure 2.10 shows the number of channels containing saccade direction information in high-frequency LFP in each implant region for each monkey, selected with ANOVA ($p < .05$).

The number of informative channels does not reflect the quality of discrete signals of the implant location, when comparing with the number of sorted single units in Table 2.1. For example, area SEF in monkey J has the largest number of sorted units, but the number of informative high-frequency LFP channels is comparable to the other two implant regions, which contain far fewer sorted units than SEF. For monkey C, area SEF contains just a few sorted single units but the highest number of informative high-frequency LFP channels, contrasting with area PFC which has far more sorted single units yet just a few informative high-frequency LFP channels.

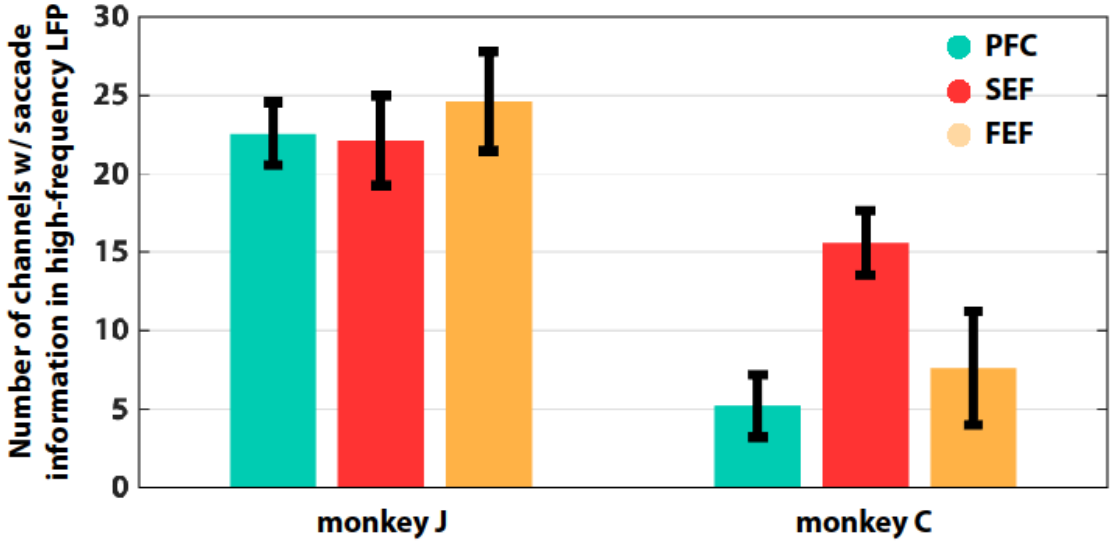

Figure 2.10. Number of informative channels for high-frequency LFP, for monkey J (left) and monkey C (right). Channels are selected using one-way ANOVA ($p < .05$).

Next, we looked at the correlation of saccade direction information between high-frequency LFP and MU+. Scatter plots of explained variances (one-way ANOVA) of high-frequency LFP and MU+ belonging to the same channel are shown in Figure 2.11 for monkey C and monkey J, respectively. Channels belonging to different implant locations are shown in different colors. For monkey J, area SEF does not show differences in saccade direction information between high-frequency LFP and MU+ overall, with some channels containing more information in MU+ and some channels more information in high-frequency LFP. While for area PFC and FEF, saccade direction information is more represented in high-frequency LFP, consistent with offline decoding performance comparisons between implant regions in Figure 2.6. Areas PFC and FEF in monkey J also contains fewer sorted single units than area SEF, indicating that the relative lack of saccade direction information in MU+ is potentially attributable to the

quality of the discrete signals in those two implant regions. For monkey C, despite having the largest number of sorted single units, area PFC contains relatively little saccade direction information in its MU+, and does not show differences in direction information between high-frequency LFP and MU+ overall as some channels contain more direction information in MU+ and others in high-frequency LFP. Area SEF contains only a few channels with sorted single units, and saccade information is more represented in the high-frequency LFP, potentially due to the quality of the discrete signals in SEF in monkey C.

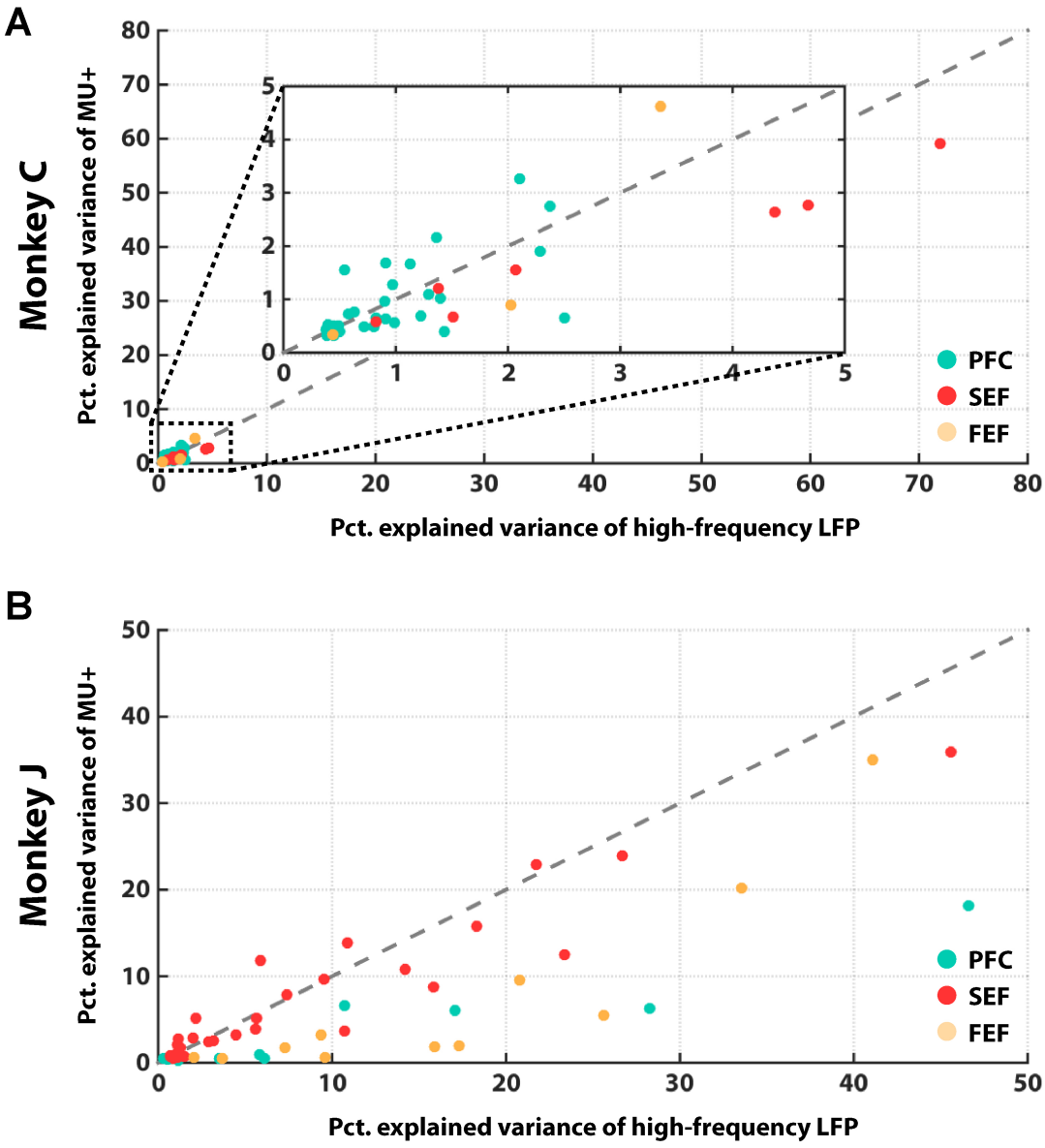

Figure 2.11. Scatter plot of explained variances of LFP and MU+, for (A) monkey C, and (B) monkey J. Explained variances are computed with ANOVA, and averaged across 10 sessions for both LFP and MU+. Dashed gray line marks x = y. A subset of channels in (A) that are enclosed by dashed black line are magnified and shown in the inset, for ease of visualization.

2.3.9. Whole trial decoding using high-frequency LFP

A sliding window of 50 ms duration was applied to the entire trial period to tease out the most information rich epochs in high-frequency LFP, using an LDA decoder and the first 300 trials of each BCI sessions with leave-one-out cross validation. In addition to using all implant regions; individual areas were separately analyzed to shed light on the most informative brain region during a delayed saccade task. Results for the two monkeys are shown in Figure 2.12; the patterns differ between the two subjects.

For both monkeys, saccade target information is registered during the cue period, and maintained throughout the entire trial when all areas are used as input for decoder, evidenced by the rise in decoding performance shortly after the start of cue presentation. Area SEF stands out as the sole region maintaining saccade information for monkey C, while all implanted regions maintain saccade information for monkey J, when individual areas are used as input. The two monkeys also differ in another aspect - area SEF in monkey C and area FEF in monkey J show an increase in decoding accuracy during the part of the response epoch after saccade execution (see next section for saccade reaction time and duration).

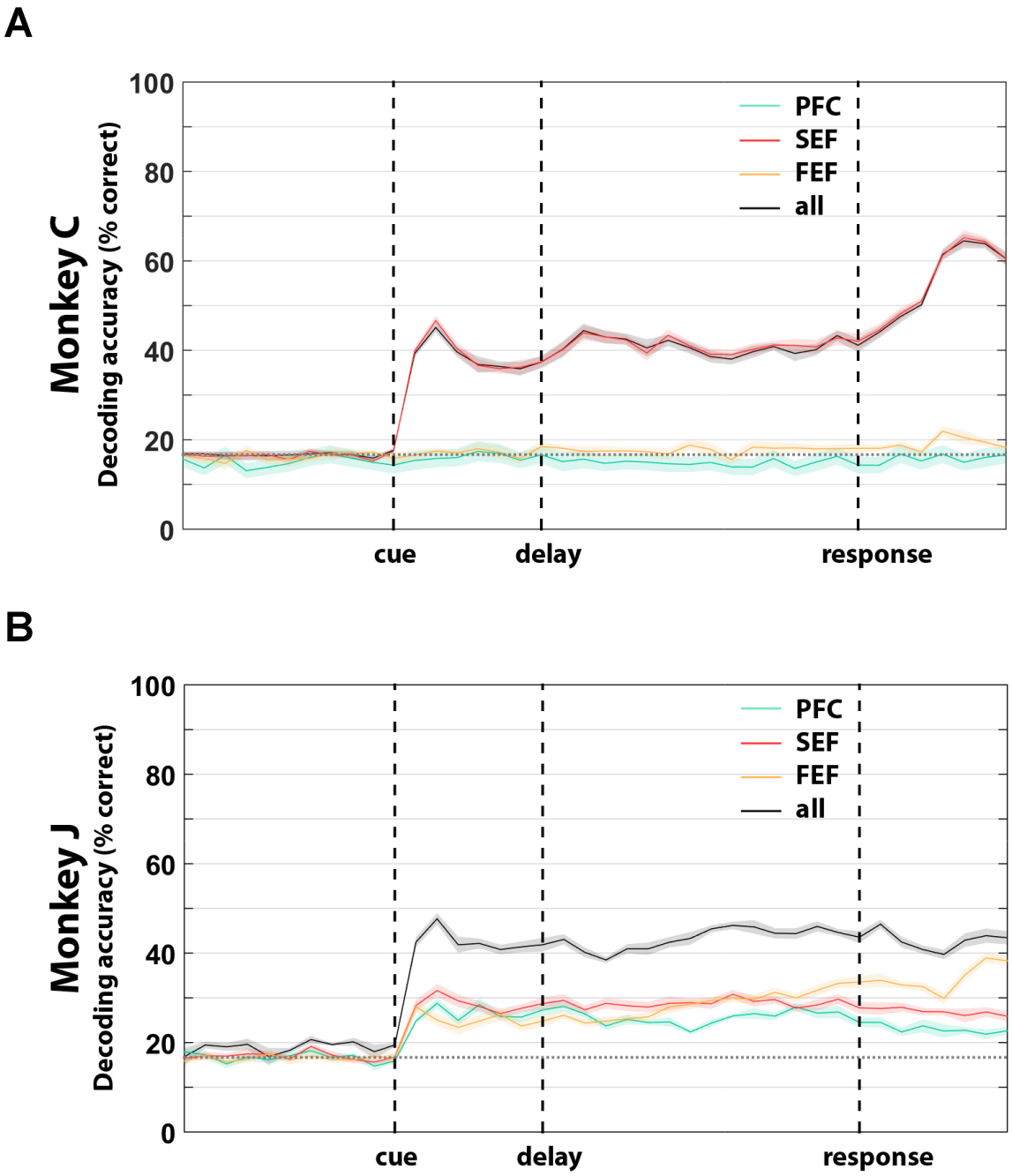

Figure 2.12. Whole trial decoding performance for both monkeys for (A) monkey C, and (B) monkey J. A sliding window of 50 ms duration is stepped every 50 ms through the entire trial period, using high-frequency LFP with an LDA decoder, and the first 300 trials (all eye-controlled) of each BCI session with leave-one-out cross validation.

2.3.10. Saccade timing and eye traces

Saccade reaction time and duration from the eye-control trials for both monkeys are stable across 10 analyzed sessions. Reaction time for monkey C is 150.61ms ±36.61ms with 9.14ms ± 9.72ms saccade duration. Reaction time for monkey J is 157.9ms ± 52.79ms with 6.67ms ± 5.58ms saccade duration.

Eye trace analysis reveals different patterns between monkeys, likely due to paradigm differences. For monkey C, the fixation point stayed on screen until the decoder had picked a target (referred to as the first version of the BCI paradigm). Monkey C had learned to withhold saccades during correct trials within 10 BCI sessions (Figure 2.13 A), but sometimes made saccades to the incorrectly decoded target that was shown on the screen during incorrectly decoded trials (eye traces of incorrectly decoded trials shown in Figure 2.14).

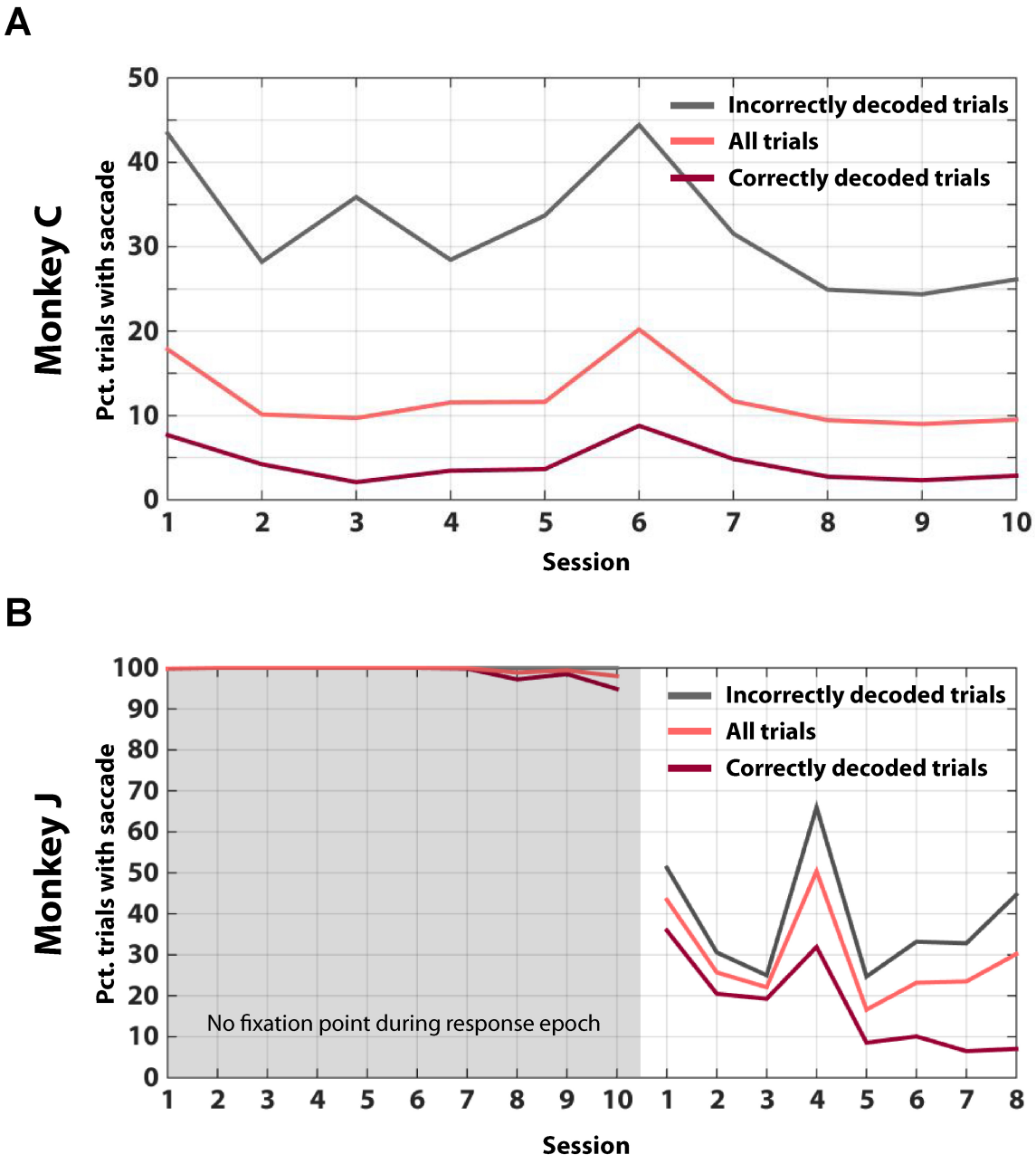

Figure 2.13. Percentage of trials with saccade for (A) monkey C and (B) monkey J. A: Percentage of trials with saccade for monkey C across 10 BCI sessions. B: Percentage of trials with saccade for monkey J, across 10 sessions of the second version of the BCI paradigm, and 8 more sessions of the first version of the BCI paradigm (same paradigm with monkey C). Shaded region indicates sessions during which the fixation point disappeared by end of the delay epoch to allow free eye movements, and non-shaded region indicates the same paradigm used for monkey C.

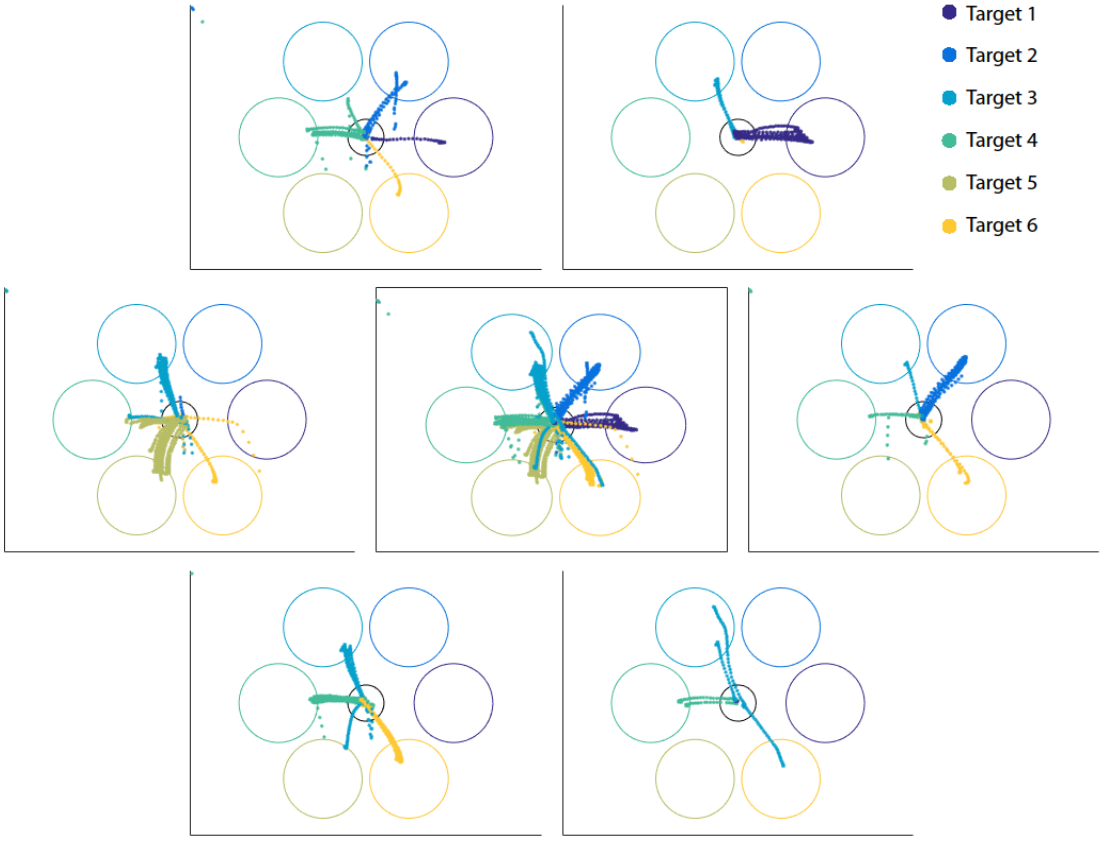

Figure 2.14. Eye traces of incorrectly decoded trials on the last day of the BCI paradigm for monkey C. In this BCI paradigm, the fixation dot remains on the screen until the decoded target is shown to discourage eye moments. In each plot, colored circles indicate location of six target regions, black circle in the center indicates fixation zone. The center subplot is a composite of all eye traces, and the six subplots surrounding it show only eye traces collected during trials with the corresponding true target locations (presented during cue epoch). Eye traces are color coded by the decoded target location. Monkey C had largely learned to withhold saccades during correct trials, but sometimes made saccades to the incorrectly decoded target that was shown on the screen during incorrectly decoded trials. For example, the subplot on the far right side show eye traces for all trials where target 1 is the true target, and monkey C made saccades to the incorrectly decoded target regions.

For monkey J, a slightly different BCI paradigm (referred to as the second version of the BCI paradigm) from that used for monkey C was tried first, with different saccade

behaviors observed (Figure 2.13 B). During this second version of the BCI paradigm (shaded region in Figure 2.13 B), the fixation point disappears at the end of the delay period to allow free eye movements, while intended saccade direction is being decoded. Monkey J developed a tendency of making saccades to the most often correctly predicted target in the same visual hemifield within the 10 BCI sessions. Specifically, the most often correctly predicted target in the right visual hemifield was target 2, and monkey J would frequently detour to target 2 before hitting the cued targets 1 or 6; the most often correctly predicted target in the left visual hemifield was target 3, and monkey J would often detour to target 3 before hitting cued target 4. Figure 2.15 shows the eye traces for correctly decoded trials during the first session of this version of the BCI paradigm, in which monkey J hit cued targets in straight trajectories, compared with Figure 2.16 showing the eye traces for correctly decoded trials during the last session (day 10) of the same version of the BCI paradigm, in which monkey J frequently hit cued targets in non-direct trajectories. For incorrectly decoded trials, monkey J usually performed a second saccade to the incorrectly decoded target that was shown on the screen during this version of the BCI paradigm.

The other version of the BCI paradigm for monkey J is identical to the BCI paradigm for monkey C (referred to as the first version of the BCI paradigm), and the eye traces show similar patterns as monkey C. However, while monkey C decreased saccade rate on all trials, monkey J learned to withhold saccade only during correctly decoded trials (non-shaded region in Figure 2.13 B). Session 1 and 4 during this BCI paradigm saw much

higher rates of saccade than the other sessions, potentially due to the fact that those two days were Tuesday and Monday sessions, usually corresponding with lack of motivation and worse performance after free access to water over the weekend.

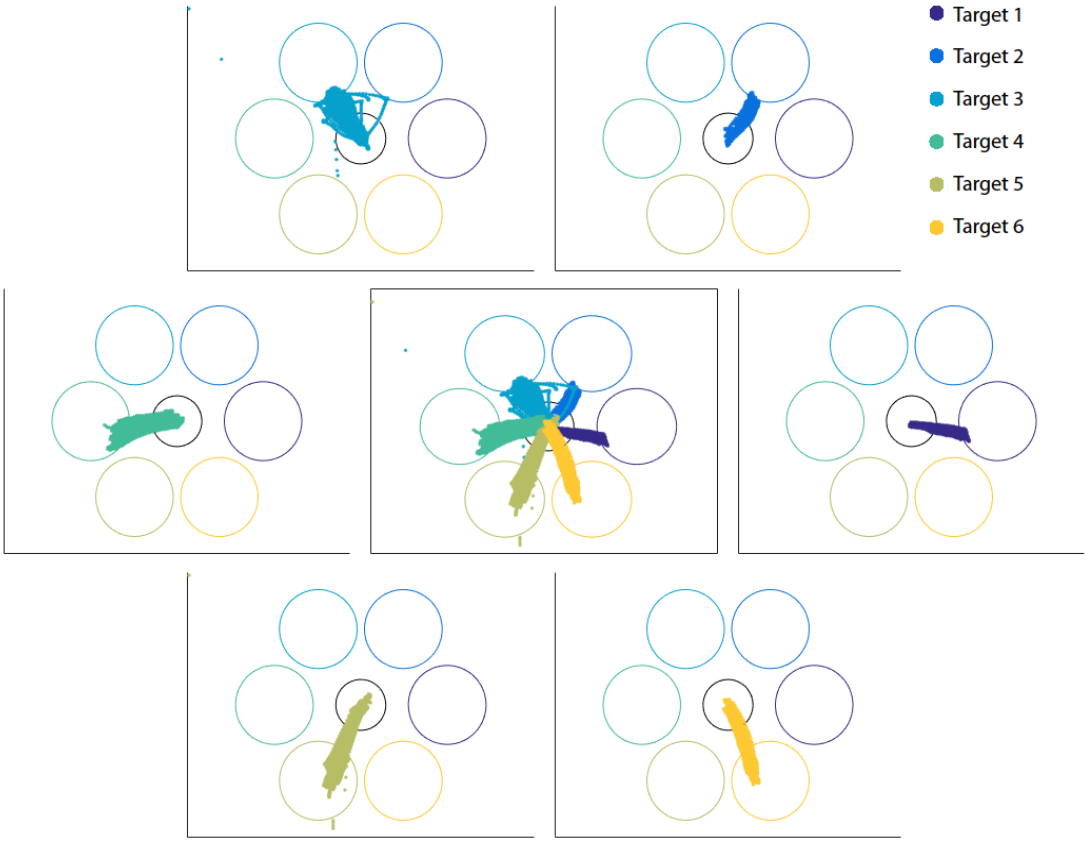

Figure 2.15. Eye traces of correctly decoded trials on the first day of the second version of the BCI paradigm, for monkey J. In this version of the paradigm (corresponding to the shaded region in figure 2.13 B), fixation dot disappears by the end of the delay period to allow for free eye movements. Monkey J produced straightforward trajectories to saccade to target. In each plot, Colored circles indicate location of six target regions, black circle in the center indicates fixation zone. The center subplot is a composite of all eye traces, and the six subplots surrounding it show only eye traces collected during trials with the corresponding true target locations (presented during cue epoch). Eye traces are color coded by the decoded target location.

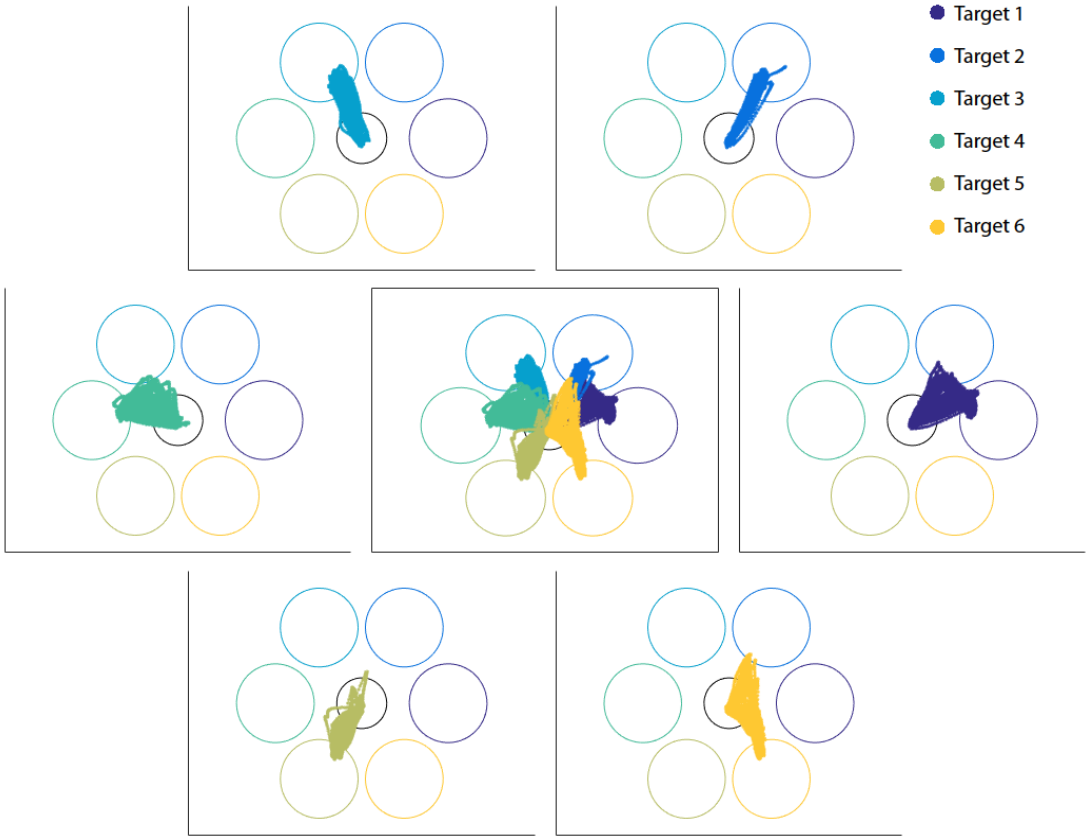

Figure 2.16. Eye traces of correctly decoded trials on the last day (day 10) of the second version of the BCI paradigm, for monkey J. In this version of the paradigm (corresponding to the non-shaded region in figure 2.13 B), the fixation dot disappears by the end of the delay period to allow for free eye movements. Monkey J had started producing curved saccade trajectories to compensate for the most often incorrectly decoded target. In each plot, Colored circles indicate location of six target regions, and colored dots indicate eye positions on screen. The center subplot is a composite of all eye traces, and the six subplots surround it show only eye traces that eventually landed in the corresponding target region.

2.4. Discussion

In contrast to previously developed BCIs that focus on replacing limb motor functions, the current study is one of the first to explore the potential of BCIs that involve microelectrodes implanted in the oculomotor system (see also Brincat *et al.*, 2013; Graf

and Andersen, 2014). Our results indicate that intended saccade directions can be predicted in real time with reasonably high accuracy (average of 66.7% correct in a 6-target task; 82.2% for contralateral targets), in the absence of any overt movement, from high-frequency LFPs recorded in frontal cortical regions, most notably SEF and FEF. This lays the groundwork for future BCIs that tap into the oculomotor system in order to perform tasks involving rapid serial selections from a set of spatially distributed targets. Such a system would be enormously useful for individuals suffering from locked-in syndrome since it could be used to rapidly navigate computer software, including AAC applications for restoring speech capabilities. We envision that an oculomotor BCI can be used either as a stand-alone system, or in combination with limb and/or other BCIs to provide an extra channel of control for AAC or for controlling movements of an external camera.

In addition to demonstrating the feasibility of an oculomotor BCI, we performed offline analyses aimed at identifying which oculomotor regions and neural activity measures provide the most information regarding intended saccade direction. While PFC, SEF, and FEF have all been implicated in voluntary oculomotor control, they have not been recorded in parallel and directly compared in the same experimental sessions before. We found that, overall, SEF and FEF provided the most informative signals for saccade target prediction. For both monkeys, neural spike rates from SEF were more informative than those from FEF and PFC, during both the memory delay epoch and the response epoch. Measures of LFP magnitude from SEF contained more information than those from FEF

and PFC in one monkey, and slightly less than that from FEF in the other monkey, potentially due to differences in signal quality or individual variability. As oculomotor regions heavily implicated in saccade planning and execution, FEF and SEF share similarities, but also exhibit notable differences in their neural properties. Both regions have been shown to exhibit broadly similar saccade related activities (Bruce *et al.*, 1985; Russo and Bruce, 2000; Tehovnik *et al.*, 2000), while SEF is also implicated in motor sequence planning (Tanji and Shima, 1994; Histed and Miller, 2006) and shows stronger sequence effects than FEF (Isoda and Tanji, 2003; Histed and Miller, 2006). SEF exhibits higher anti-saccade activities than pro-saccades (Johnston and Everling, 2008). FEF has long been known to encode saccade endpoints in vector form in retinocentric space (Bruce *et al.*, 1985; Tehovnik *et al.*, 2000), while SEF appears to encode saccade endpoints in multiple coordinate systems, and has been proposed to be involved in coordinate transformation (Tehovnik *et al.*, 2000; Martinez-Trujillo *et al.*, 2004). FEF exhibits stronger connectivity than SEF with lower-order saccade generating structures (Huerta and Kaas, 1990; Tehovnik *et al.*, 2000), and requires less current to elicit saccades than SEF under electrical stimulation (Tehovnik *et al.*, 2000). These findings indicate SEF is likely upstream from FEF, and more involved in the preparation rather than the motor production aspects of saccade generation. The high decoding performance in SEF even during the response epoch is notable given the above consideration. Our results suggest SEF plays a role no less significant than FEF in the execution of saccade, and can be a rich source signal for oculomotor BCIs.

Of the three brain regions studied, we found the least information regarding saccade direction in PFC for both monkeys. PFC has been implicated in memory-guided saccades, working memory, decision processes related to saccades (Chafee and Goldman-Rakic, 1998; Rainer, Asaad and Miller, 1998; Pierrot-Deseilligny *et al.*, 2004). PFC neurons also exhibit directional tuning (Funahashi, Bruce and Goldman-Rakic, 1991). Its neural signals have been used to decode saccade targets successfully offline (Markowitz *et al.*, 2011; Boulay *et al.*, 2015) - authors in (Markowitz *et al.*, 2011) targeted PFC and FEF together, and authors in (Boulay *et al.*, 2015) targeted specifically PFC. However, its exact role in saccadic tasks is less understood than that of FEF and SEF, and the current findings suggest that it contains relatively little stable information regarding saccade direction in the delayed saccade task.

During whole trial decoding, target information was kept since cue period for both monkeys, and remained stable into the response period. In agreement with previous offline analysis, only area SEF was informative for monkey C, and in fact was more informative during the post saccade period (Figure 2.10 A). For monkey J, all three areas maintained target information at about the same level, but area FEF peaked during the post saccade period. The results indicate that there exist individual variabilities and potentially signal quality differences that preclude strong conclusions about regional contributions to saccade production, especially during the post-saccade period.

To identify the best neural measures for decoding intended saccade direction, we

compared decoding performance for a set of discrete (spike-related), continuous (LFP-related), and hybrid neural signal measures. The reaching literature lacks consensus regarding whether single-neuron spike rates, multiunit spike rates, LFPs, or combinations of these signals are best for decoding purposes. Although spike rates have generally been used in arm movement BCIs (Wessberg *et al.*, 2000; Taylor, Tillery and Schwartz, 2002), conflicting results exist concerning whether spike rates or LFPs provide better signal measures for decoding. For example, while authors in (Bansal *et al.*, 2012) found spike rates to be superior to LFPs (including 100-200 Hz, 200-400 Hz bands) in the primary motor cortex (M1) and ventral premotor cortex (PMv) for decoding 3D arm end point and reach kinematics, authors in (Mehring *et al.*, 2003) reported that in M1, LFPs (< 150 Hz) can be equally or more effective than spike rates at decoding arm trajectories, and authors in (Stark and Abeles, 2007) found what they called multiunit activities between 300 Hz and 6000 Hz in M1, dorsal premotor cortex (PMd) and PMv to be the best signal for decoding reach and grasp related parameters. Furthermore, some studies suggest better decoding performance can be achieved by combining spiking activity and LFPs into a hybrid measure (Mehring *et al.*, 2003; Stark and Abeles, 2007; Bansal *et al.*, 2012).

Our results indicate that relevant decoding information is restricted to neither a specific frequency band nor a narrow temporal window within the delay period. Of the 11 neural measures compared, magnitude of the LFP in the relatively broad 80-500 Hz band (which we refer to as *high-frequency LFP*) provided the richest information of saccade direction intention across a range of decoders. The high-frequency LFP used herein differs from

those found to be the most informative in other LFP-based decoding studies, which have reported a wide variety of frequency ranges including sub-ranges of 0-150 Hz (So *et al.*, 2014), combinations of sub-ranges below 190 Hz (Schalk *et al.*, 2007), 25-90 Hz (Pesaran *et al.*, 2002), 50-300 Hz (Markowitz *et al.*, 2011), 70-200 Hz (Kubánek *et al.*, 2009), 76-150 Hz (Miller *et al.*, 2008), and 200-400 Hz (Zhuang *et al.*, 2010). Together with the current results, these findings suggest that the optimal neural activity measure for BCI purposes depends on the exact recording configuration used and brain areas implanted.

Our high-frequency LFP signals include the high gamma band (often defined as 70-150 Hz, though the upper bound can range up to 250 Hz). Prior studies indicate that power in the high gamma band is strongly correlated with population spiking activity near the recording electrode (Liu and Newsome, 2006; Belitski *et al.*, 2008; Ray *et al.*, 2008; Manning *et al.*, 2009; Ray and Maunsell, 2011b). The superior performance of high-frequency LFPs compared to other neural measures in our study may be attributable to their success at capturing the population spiking activity, including the smaller spikes that are not picked up during the thresholding and spike-sorting process. This is corroborated by two results in our study. First, offline decoding accuracies using spiking signals improved when non-isolable spikes were also included ('SU' vs. 'SU+' in Figures 2.4 and 2.5), indicating that useful signals were discarded as 'noise' during the spike sorting process. Second, for both monkeys, combining spiking activity with high-frequency LFPs does not result in more information than what already exists in the high-frequency LFPs

(Figure 2.4), indicating redundant information in the spiking signals and high-frequency LFPs. Relatedly, in an analysis not included in Figure 2.4, performance of an LDA decoder using high-frequency LFP (average decoder accuracy 82.32% with SD ± 4.52%) was compared to performance using LFP in the high gamma range (80-200 Hz, average decoder accuracy 69.87% ± 5.11%). The better performance of the high-frequency LFP indicates that substantial saccade information exists in the 200-500 Hz frequency range, also evidenced in the explained variances in this band (Figure 2.7), and the overall higher explained variance in high-frequency LFP band when compared with MU+ (Figure 2.11), perhaps because this range captures some aspect of population spiking activity not evident in the high gamma range.

It should be noted that, in one monkey, offline decoding performances in SEF using a discrete signal ('SU+') are comparable to those using high-frequency LFPs (Figure 2.6A, monkey J). However, when all three implant regions are pooled together, high-frequency LFPs still provide better performance (Figure 2.6B, monkey J). The contribution of individual implant regions to decoding performance do not appear to be additive, and potentially reflect synergistic interactions between all regions.

A major advantage of using LFP signals compared to spike-related signals in BCIs is their efficiency. They can be recorded at much lower sampling rates than spiking signals ($\leq$ 1 kHz vs. $\geq$ 20 kHz), allowing use of lower cost, lower power recording configuration. Feature extraction can be performed very rapidly, requiring only bandpass filtering and

rectification, in contrast to spiking signals, which require filtering, thresholding, waveform feature extraction, and spike sorting. In addition, spike sorting often requires end-user manual adjustment, which is obviated by using continuous signals. Thus, high-frequency LFP signals may allow for faster, lower cost, and easier to use BCIs. High-frequency LFP also provided consistently better performance across different types decoders in our analyses. While the LDA decoder had the highest performance, better decoders may well be developed in the future to cater to different needs of individual users. However, high-frequency LFP will likely remain one of the most informational rich input signals regardless of the decoder type.

To the best of our knowledge, there is only one other example of an eye-movement-based BCI in the current research literature. Graf and Andersen (Graf and Andersen, 2014) used SU spikes collected from five individually adjustable microelectrodes located in a different part of the saccade system, the lateral intraparietal cortex (area LIP). An average decoder accuracy of 32.2% for a delayed saccade task involving 8 targets (chance level 12.5%) was reported. Although this is lower than the average decoder accuracy of 66.7% in our 6-target BCI paradigm (chance level of 16.7%), differences in the recording configuration, signal selection, and decoders involved in the two studies prohibit strong conclusions regarding the relative suitability of LIP for an oculomotor BCI as compared to the frontal cortical regions implanted here.

It is notable that, in contrast to most arm/hand area BCI studies, we did not see a

significant performance increase with practice using the oculomotor BCI. In addition, change in the monkeys' behaviors was independent from change in decoding performance. Monkey C did learn to withhold overt saccade (Figure 2.13A), and the decoding performance remained stable across sessions. During the same version of BCI paradigm, monkey J learned to withhold saccades on correctly decoded trials, but still made corrective saccades on incorrectly decoded trials (Figure 2.13B, non-shaded region). During the second BCI paradigm (Figure 2.13B, shaded region), monkey J did not show any noticeable change in decoding performance, while observing a different strategy of making detoured saccades (Figure 2.16). Relatedly, when using a decoder with fixed parameters in their LIP-based oculomotor BCI, Graf and Andersen (Graf and Andersen, 2014) found a steady decrease in performance over time rather than an increase that would be indicative of motor learning. Together these findings suggest that the delayed saccade task may not be amenable to inducing plasticity in the oculomotor system. Graf and Andersen (Graf and Andersen, 2014) did note performance improvements within the same session with practice when using an adaptive decoder that continuously updated its parameters during BCI trials, but the degree to which these improvements reflected the non-stationarity of neural signals (Wu and Hatsopoulos, 2008) versus changes in neural firing properties resulting from motor learning remains unclear. In offline analysis for our BCI paradigm, signal drift was detected with an adaptive decoder, and worsened within the same session (Figure 2.9). Decoding performances were boosted by using an adaptive approach, suggesting that accounting for non-stationarity of the neural signals may be confused with performance improvements

resulting from true learning.

Although our results provide an initial “proof of concept” for an oculomotor BCI involving implants in SEF and FEF, key limitations need to be addressed before such a system could be considered for human implantation. First, although our BCI’s performance was well above chance, it is not high enough for effective use of (for example) an AAC application to restore speech communication. This suggests the need for more electrode channels in order to obtain an acceptable accuracy level, particularly in the information-rich SEF and FEF regions. Second, we saw no evidence of performance improvement with practice, indicating that the delayed saccade paradigm may not be well-suited for capitalizing on motor learning processes that lead to improvements in performance in many limb-related BCIs. Third, our findings indicate that contralateral targets are more accurately predicted than ipsilateral targets, suggesting that bilateral implantation of FEF and SEF would provide improved performance across the entire visual field over unilateral implantation.

3. SPECTRAL ANALYSIS OF BCI DELAYED SACCADE TASK

3.1. Introduction

One major advantage of this project is the use of simultaneous recordings from electrode arrays in multiple prefrontal regions involved in saccades, specifically the dorsolateral prefrontal cortex (referred to as PFC here), the frontal eye field (FEF), and the supplementary eye field (SEF). This arrangement provides an opportunity to study the oculomotor system from multiple considerations. First, very few studies have looked at interactions between oculomotor regions during eye movement production. Yet to understand how perceptions/actions arise in the brain, it has become increasingly important to study the system as a whole instead of its individual components (Varela et al., 2001). Second, the "communication through coherence" hypothesis (Fries, 2005, 2009; Womelsdorf and Fries, 2007) proposes that functional connectivity (and by extension, information processing) across multiple brain regions is mediated by different rhythms, by allowing concurrent action potentials arriving in a brain region to be received in a coherent/synchronous manner, thus creating strong population effects (Fries, 2005; Börgers and Nancy J Kopell, 2008). Neural oscillations can therefore be a reflection of the cognitive state or task parameters. Third, oscillations in different frequency bands have been implicated in working memory tasks in different brain regions (Siegel, Donner and Engel, 2012), for example: theta band (Sederberg et al., 2003; for reviews see Hsieh & Ranganath, 2014; Mitchell et al., 2008), delta band (Weiss & Rappelsberger, 2000), alpha/mu band (Jensen et al., 2002), beta band (Buschman & Miller, 2007; Saalmann et

al., 2007), and gamma band (Sederberg *et al.*, 2003; Womelsdorf *et al.*, 2006; Buschman and Miller, 2007). These oscillations may play a role in mediating information transfer in tasks involving visual working memory, such as the delayed saccade BCI paradigm. For instance, it is well known that beta band activity in motor areas is prominent during rest and dissipates during movement production, signifying a state of 'status quo' (Engel & Fries, 2010), while gamma band activity may reflect inhibitory neuron spiking activity (Cardin et al., 2009), and high gamma band (> 80Hz) activity likely reflects multi-unit spiking activities (Ray & Maunsell, 2011a). How these different frequency bands behave within the oculomotor system is not well understood. For example, beta band activity may start increasing as early as the onset of fixation if it indeed represents withholding of movement, or it may be prominent during the delay period if it facilitates movement preparation. To our knowledge, this study is the first to characterize large-scale functional connectivity in multiple prefrontal oculomotor regions.

We employ a few coupling measures to analyze the frequency contents of the data, in two domains: spike-field coupling and field-field coupling. After comparing different measures, we will present the results focused on spike-field coherence and field-field coherence. Spike-field coherence has been proposed to carry stimulus information across brain regions (Womelsdorf and Fries, 2007; Lakatos *et al.*, 2008; Schroeder and Lakatos, 2009), and correlate with relevant task parameters (Womelsdorf *et al.*, 2006; Siegel, Warden and Miller, 2009). Field-field coherence (usually referred to simply as "coherence") is the equivalent of correlation in the frequency domain, and can be used to

explore specific frequency interactions that are complementary to temporal domain correlations. Coherence measures have been extensively used in network analysis of neural data, particularly for oscillatory activities (Pereda et al., 2005). An increase in coherence suggests an increase of functional connectivity that marks certain behavioral or cognitive states, for instance beta band coherence has been implicated in top-down attention and gamma band in bottom-up attention (Buschman & Miller, 2007). Characterizing the functional connectivity can provide information regarding the behavioral or cognitive state of the subject.

This chapter aims to characterize the frequency domain functional connectivity in oculomotor brain regions in a delayed-saccade task. First spike-field coupling is described using single units and local field potentials from the same recording electrode, to show task relevant changes. Then field-field coupling is discussed for all pairs of electrodes, and summarized between implant regions. The coherence patterns of different frequency bands of interest on each channel were examined, compared and contrasted with each other, to tease out the frequency contents carrying information about target location.

3.2. Methodology

We describe five coupling measures here: coherence, spike-field coherence, phase-locking value, pairwise-phase consistency, and canonical coherence. Each measures the coupling strength of the phase and/or amplitude between neural signals (more details

below), which can be discrete (spikes), or continuous (field). They can be grouped based on whether it's a spike-field coupling measure, a field-field coupling measure, or both. Table 3.1 summarizes the coupling measures that can be used as spike-field and field-field coupling measures.

	Spike-field coupling	Field-field coupling
Coherence	No	Yes
Spike-field coherence	Yes	No
Phase-locking value	Yes	Yes
Pairwise-phase	Yes	Yes
Canonical coherence	No	Yes

Table 3.3. Coupling measures category.

The spike-field coupling measures described here were computed for sorted single units (method described in section 2.2) and LFP on the same recording electrode. The field-field coupling measures were computed for LFPs between different recording electrodes. With 96 channels per subject, there are 4560 unique pairs of channels for field-field coupling measures.

3.2.1. Coherence

Coherence measures the coupling strength of the power spectra between two signals. Coherence of a particular frequency band f between two signals, x and y, is defined as the following:

$$C_{xy}(f) = \frac{|S_{xy}(f)|}{\sqrt{S_{xx}(f)S_{yy}(f)}}$$

where S_{xy} is the cross spectrum between x and y, S_{xx} and S_{yy} are the power spectra of x and y respectively. It follows from the formulation that coherence involves both the amplitude and phase information of the spectra, and its value is bounded by:

$$0 \leq C_{xy} \leq 1.$$

A coherence value of 0 indicates a lack of any coupling at the frequency band of interest, while a value of 1 indicates complete coupling in phase and amplitude between two signals.

3.2.2. Spike-field coherence

Spike-field coherence (SFC) measures the coupling strength between spikes and the local field potential. Spikes may be influenced by the rhythmic activities in the on-going local field potential and as a result be coupled to particular frequency bands. There are different formulations and the one used here follows the same method as Fries et al. (2001):

$$SFC(f) = \frac{S_{STA}(f)}{\bar{S}_{LFP}(f)}$$

where S_{STA} is the power spectrum of the spike-triggered-average (STA) local field potential (i.e.: extract individual LFP segments, compute the average of all the LFP segments, then compute the power spectrum of this average), and $\bar{S}_{LFP}$ is the averaged power spectrum of each individual LFP segment triggered by a spike (i.e.: extract

individual LFP segments, take their power spectra, then compute the average of all the power spectra), at frequency f. Since the STA likely averages out the spectral content non-coupled to spikes and leaves the frequency content coupled to spikes, while $\bar{S}_{LFP}$ tends to retain all oscillatory components in the on-going LFP, the SFC can be intuitively understood as a ratio that accentuates the frequency band which strongly couples with spikes while suppressing irrelevant ones. It follows from the formulation that:

$$0 \leq SFC \leq 1.$$

An SFC value of 0 indicates the spike occurrences are random at the particular frequency band, while an SFC value of 1 indicates complete coupling in phase and amplitude.

3.2.3. Phase-locking value

Phase-locking value (PLV) discards the amplitude information in the power spectrum, and measures only phase coupling between two signals. PLV of a particular frequency f between signals x and y is defined as:

$$PLV_{xy} = \frac{1}{N}\left|\sum_{n=1}^{N} e^{i(\varphi_{x_i}-\varphi_{y_i})}\right|$$

where N is the number of samples being considered, and $\varphi_{x_i}/\varphi_{y_i}$ is the phase at frequency f of signal x/y computed for the i^{th} sample. It follows from the formulation that PLV is bounded by:

$$0 \leq PLV_{xy} \leq 1.$$

A PLV value of 0 indicates the two signals are completely out of phase at the particular frequency band, while a PLV value of 1 indicates complete phase synchronization

between signals x and y at frequency f. Under uniform signal power, PLV becomes coherence.

PLV can be computed for field-field coupling, as well as spike-field coupling, since it is a measure of the phase difference only. In the latter case, $\varphi_{x_i} - \varphi_{y_i}$ can be replaced by the LFP phase at the occurrence of the i^{th} spike, resulting in a metric of the phase locking strength between spikes and LFP.

3.2.4. Pairwise-phase consistency

The Pairwise-phase consistency (PPC) is an unbiased metric of phase coupling. Whereas the PLV is positively biased, the PPC is a bias-free and consistent estimator related to the squared mean resultant length (Vinck et al., 2010). Given N samples (for example, N spikes) with their phases $(\theta_1, \theta_2, \dots, \theta_N)$ extracted for frequency f, the PPC is defined as:

$$PPC = \frac{2}{N(N-1)} \sum_{j=1}^{N-1} \sum_{k=j+1}^{N} \cos(\theta_j - \theta_k).$$

In other words, PPC is a metric of population angular differences between unique pair of samples at frequency f. It follows from the formulation that it's bounded by:

$$-1 \leq PPC \leq 1.$$

A value of 1 indicates complete phase synchronization; a value of 0 indicates absence of consistent phase relationship; and a value of -1 indicates the signals are consistently out of phase. It's worth noting that PPC trades bias for variance. While it is an unbiased metric of the population parameter, its variance is higher than PLV when the sample size is small, which may become an issue for sparsely firing units. From simulation and

observation, it seems > 40 samples is a safe lower cut-off. Similar to PLV, PPC can be computed for field-field, as well as spike-field couplings.

3.2.5. Canonical coherence

Canonical coherence is the frequency domain equivalent of canonical correlation. It is a measure of the coupling strength between two sets of signals $x = (x_1, x_2, \dots, x_p)$, and $y = (y_1, y_2, \dots, y_q)$ of random variables, and is useful in characterizing covariance structures between two groups of signals instead of just a single pair of signals, for which correlation is commonly used. Before describing canonical coherence, it's helpful to first clarify canonical correlation. Canonical correlation is the maximum amount of correlation between linear combinations of x and y:

$$Ccorr(x, y) = \underset{a,b}{argmax}\ corr(a^T x, b^T y) = \underset{a,b}{argmax} \frac{a^T \Sigma_{xy} b}{\sqrt{a^T \Sigma_{xx} a}\sqrt{b^T \Sigma_{yy} b}}.$$

Computing canonical correlation amounts to finding vectors a and b that maximize the correlation between $a^T x$ and $b^T y$, which is solved using singular value decomposition on the standardized covariance matrices $\Sigma_{xx}, \Sigma_{xy}, \Sigma_{yy}$ and Σ_{yx}. Here a^T denotes the transpose of vector a.

The equivalent characterization in the frequency domain follows the same formulation as described in the time domain, only that instead of looking for the maximum amount of correlation between linear combinations of time domain signals x and y, we are looking

for the maximum amount of coherence between linear combination of frequency domain representations X and Y at frequency f. Let:

$$C(\alpha, \beta) = corr(\alpha^* X, \beta^* Y) = \frac{\alpha^* \mathrm{S}_{XY} \beta}{\sqrt{\alpha^* \mathrm{S}_{XX} \alpha}\sqrt{\beta^* \mathrm{S}_{YY} \beta}}.$$

Since $C(\alpha, \beta)$ can be complex, the canonical coherence is defined as the optimization of the maximum squared value:

$$Ccoh(X, Y) = \underset{\alpha,\beta}{argmax}\, C(\alpha, \beta)\; C^*(\alpha, \beta)$$

where $\mathrm{S}_{XY}, \mathrm{S}_{XY}, \mathrm{S}_{XY}$ are the cross-spectral matrices of X and Y at frequency f, and α^* denotes the conjugate transpose of α.

The proof of solution to this optimization problem involves using the Lagrange multiplier and singular value decomposition detailed in (Stephens, 2015). The steps to solving for $Ccoh(X, Y)$ at frequency f are:

1. Compute the cross-spectral matrices S_{XX}, S_{YY}, S_{XY}, S_{YX}.

2. Compute $Q_{XY} = S_{XX}^{-1/2} S_{XY} S_{YY}^{-1/2}$.

3. Decompose Q_{XY} into $Q_{XY} = U\Sigma V^*$ using singular value decomposition.

4. Pick the first singular value σ_1, and its corresponding first left and right singular vectors u_1 and v_1.

5. The canonical coherence is given by σ_1, and the optimal linear combination vectors α and β are solved by $\alpha = S_{XX}^{-1/2} u_1$, $\beta = S_{YY}^{-1/2} v_1$.

3.2.6. Signal processing for spike-field coupling measures

To compute spike-field coupling measures (SFC, PLV, and PPC), spikes from all trials with the same cued saccade target (at least 300 trials per target, for 6 targets) were combined so as to have a large enough number of spikes for reasonable estimates of each spike-field coupling measure. They were then binned into 100 ms windows, and stepped every 50 ms in trial. LFP traces of 512 ms duration centered on each spike were then extracted from the same recording electrode for all spikes within the same window.

Spike-Field Coherence The spike-triggered average (STA) for that time step was then obtained as the average of all the LFP traces. Its power spectrum (S_{STA}) was then computed with the multitaper method, using a signal length of 512 samples, 1 kHz sampling rate, and 1 taper, which results in a frequency resolution of about 1.95 Hz. To compute the average power spectrum of the LFPs ($\bar{S}_{LFP}$), power spectrum for each extracted LFP segment was computed with the same multitaper parameters. All the power spectra were then averaged to yield the average LFP power spectrum ($\bar{S}_{LFP}$). For each frequency and time window, the SFC at selected frequency was then computed as $SFC(f) = \frac{S_{STA}(f)}{\bar{S}_{LFP}(f)}$.

Phase-Locking Value The power spectra for all LFP traces were computed with the same multitaper parameters as described for spike-field coherence. Then, for each frequency and time window, the complex phases were extracted from the power spectra, then summed and averaged to yield the PLV value for spike-field coupling measure.

Pairwise-Phase Consistency The power spectra for all LFP traces were computed with the same multitaper parameters as described for spike-field coherence. For each frequency and time window, the phases at which the spikes occurred were then extracted from the power spectra to compute the PPC using the equation described in section 3.2.4.

3.2.7. Signal processing for field-field coupling measures

To obtain a spectrotemporal representation, field-field coupling measures were applied to LFPs for all trials with the same cued saccade target (at least 300 trials per target, for 6 targets), windowed in 512 ms duration, and stepped every 50 ms. To reduce spectral leakage into neighboring bands, the multitaper method was used (Bokil et al., 2010). LFPs from all channels were then analyzed using multitaper method, a signal length of 512 samples, 1 kHz sampling rate, and 1 taper, which resulted in a frequency resolution of about 1.95 Hz. Using trials with the same cued saccade target yielded at least 300 multitaper coefficients (from at least 300 trials) per target condition for every frequency and time window. Power spectra for all 96 channels and cross-spectra between all 4560 pairs of channels were obtained for each monkey from the multitaper coefficients.

Coherence The coherence values for each frequency and time window for all 4560 pairs of channels were then computed using the formula described in section 3.2.1, using the power spectra and cross-power spectra.

Phase-locking Value The complex phase differences between each channel pair were then extracted from the cross-spectra of all 4560 pairs of channels per monkey, summed and averaged across trials (at least 300) to produce the PLV for each frequency and time point.

Pairwise-Phase Consistency Phases were extracted from the power spectra of all 96 channels to compute the PPC between all 4560 pairs of electrodes using the equation described in section 3.2.4, where N was the number of trials used (at least 300 per target condition).

Canonical Coherence The 96 channels were organized into 3 groups based on which brain region (PFC, SEF, or FEF) they were implanted in, yielding 3 groups each consisting of 32 channels per monkey. This produced 3 unique pairs of groups: PFC-SEF, PFC-FEF, and SEF-FEF. Using methods described in section 3.2.5, and with multitaper parameters described for field-field coupling measures above, canonical coherence was computed for each pair of groups, to provide a brain region level description for each frequency and time window.

3.3. Results

3.3.1. Spike-field coupling

Of the measures introduced above, spike-field coherence (SFC), phase locking value (PLV), and pairwise-phase consistency (PPC) can be applied to quantify spike-field coupling strength. In the analysis, all spike-field coupling measures were computed for sorted single units and LFPs from the same recording electrode.

Caveat Before presenting results, it's worth pointing out one caveat for this analysis. In order to provide an unbiased estimate for SFC, PLV, and PPC, the number of spikes needs to be sufficiently large. Spike train to field coherence has been shown to be

positively dependent on the number of spikes (Zeitler et al. 2006; Grasse & Moxon 2010; Lepage et al. 2011; Vinck et al. 2012). All three measures suffer from inflated results when the number of spikes used in the computation is small. PPC in particular suffered the most from a small number of spikes since it achieves an unbiased estimate by trading bias with variance, therefore needed a higher number of spikes to reduce the variance of the estimation. In our data, despite pooling spikes from all trials with the same cued saccade target, we still saw artifacts in the spectrotemporal graphs of the spike-field coupling measures manifesting as extremely high values across almost all frequency bands. This frequently happened when the spike count was low for a particular time window. Figure 3.1 shows an example of this artifact that can clearly be seen directly before delay onset, where all three coupling measures have high positive values across almost the entire frequency spectrum as an artifact of insufficient number of spikes used in estimation. PPC in particular suffered the most as the entire spectrotemporal plot contains patches of extremely high values.

The extremely low number of spikes occurred during different epochs on different channels, adding to difficulty in interpreting results. While resampling methods such as bootstrapping and jackknife exist, the extremely low number of spike counts (e.g. spike counts were smaller than 5 for the second half of the delay period, in the bottom panel in Figure 3.1 where pooled spike counts are shown) would not provide much benefit, as the number of samples (spikes) was far smaller than the number of iterations required for an effective resampling procedure, which is typically in the thousands. To help interpret the

coupling measure estimates, the figures presented below for spike-field coupling measures are generally accompanied with spike counts for visual inspections where low spike counts occur in trial. We picked a threshold of 40 spikes per bin to filter out channels that might suffer from this artifact, as 40 seemed a conservative threshold that worked for all three measures. An example of how frequently this issue occurs, during one session analyzed for monkey C, 9 out of 38 sorted single units had spike counts that were consistently above 40 throughout the entire trial after pooling across trials of the same target location, while the rest of the sorted single units only had enough spikes some of the time (e.g. the unit in Figure 3.1 only had high spike counts in the response epoch, while remaining relatively quiet during the rest of the trial). In another example, in a session analyzed for monkey J, 16 out of 56 sorted single units had spike counts that were consistently above 40 throughout the entire trial.

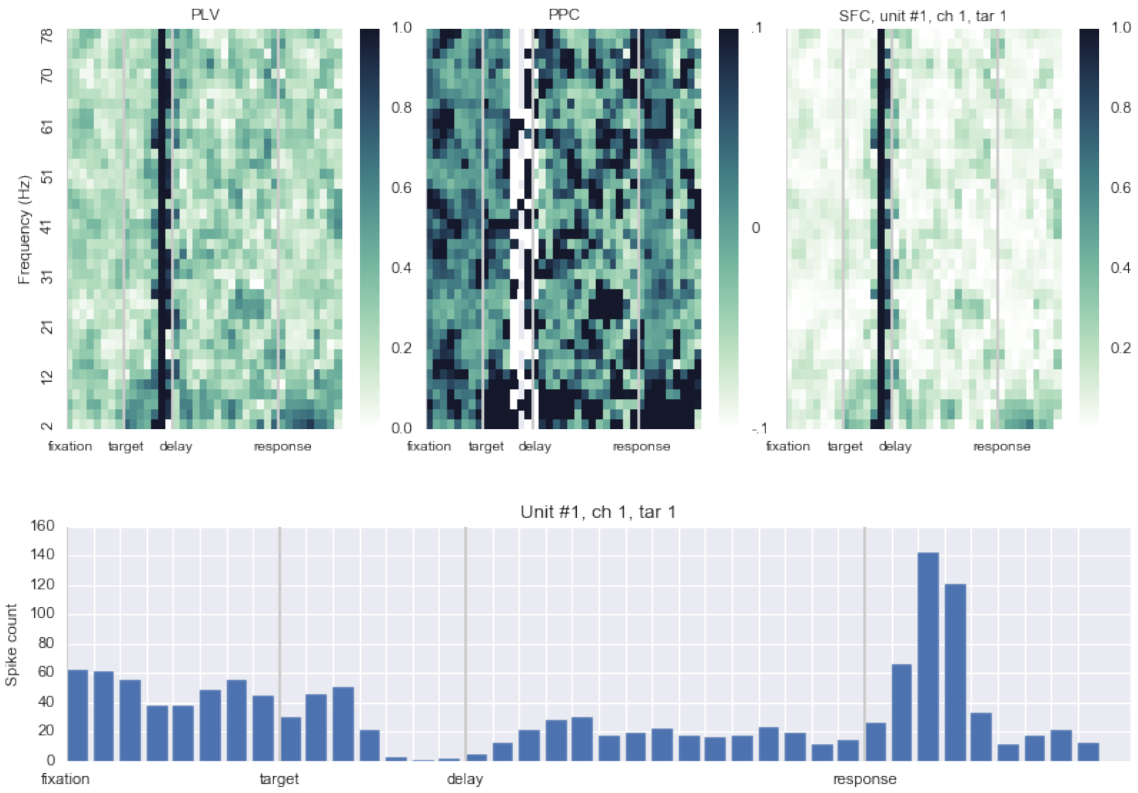

Figure 3.1. Artifact in spike-field coupling measures obtained from insufficient number of spikes. An example single unit from a PFC channel, monkey C. Bottom panel shows the spike count in each window with 100 ms duration, slided every 50 ms, summed over all the trials for target 1, from one session of monkey C. Top panels show the spectrotemporal representation of the three spike-field coupling measures: phase-locking value (PLV), pairwise-phase consistency (PPC), and spike-field coherence (SFC), from left to right, with separate color bars for each measure. Y-axis from each top panel marks frequencies from 2 Hz to 80 Hz. Gray lines on the x-axis in all panels mark the onset of different epochs in trial: fixation, cue, delay, and response. For windows with low spike counts (e.g., right before onset of the delay epoch), all three coupling measures have high positive values across the entire frequency spectrum, as an artifact of insufficient number of spikes used in estimation. PPC in particular suffer the most.

All measures reported for field-field couplings so far, coherence, PLV, and PPC, show similar trends observed in all frequency bands of interest. One example in Figure 3.2 is shown, where the spike-field coupling measures and the spike counts were computed from all trials for one target direction. This unit was recorded from a PFC channel in

monkey C, and exhibited increases in spike-field coupling in the low frequency ranges concentrated around 2-4 Hz, right after target onset, delay, and response epochs. These increases in spike-field coupling do not appear to be correlated with low spike counts (unlike the unit in Figure 3.1), as the second half of the delay period contains the lowest spike counts, yet none of the three coupling measures show increase in coupling. Similar to this unit, other units also exhibit a tendency to increase spike-field coupling directly after epoch onsets.

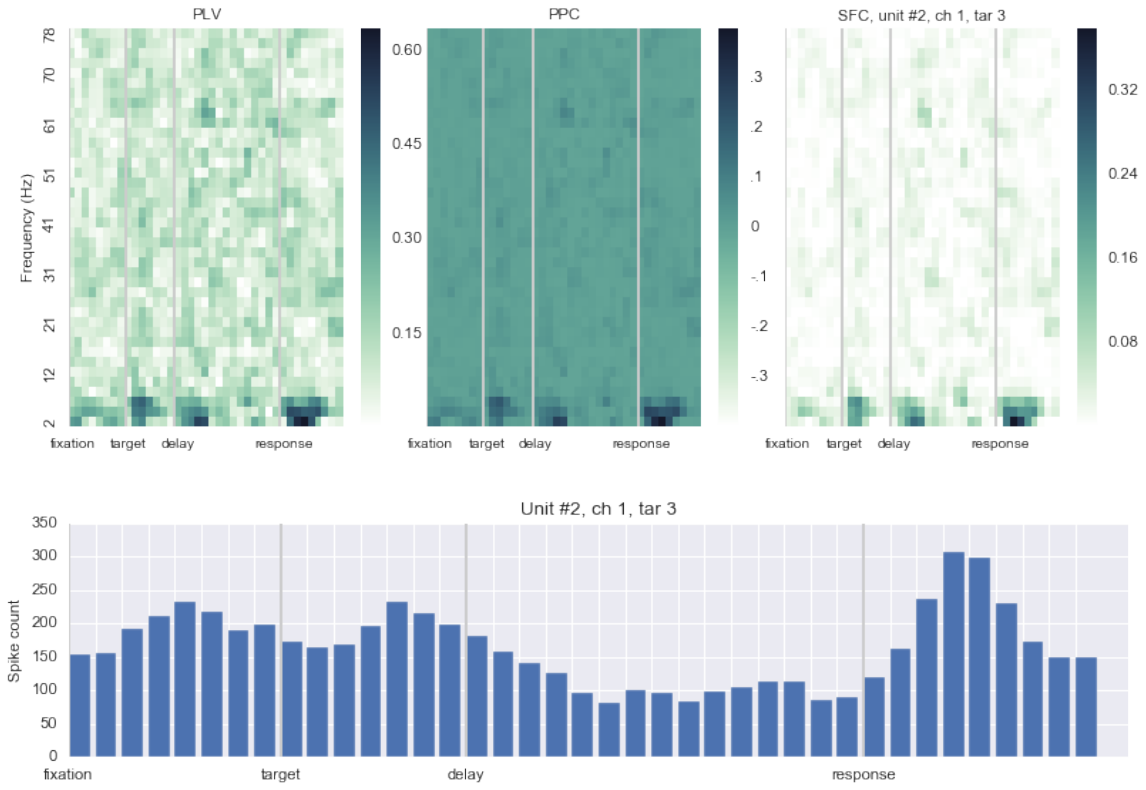

Figure 3.2. Example spike-field coupling measures of one unit from a PFC channel for monkey C. In this example, increases in spike-field coupling are present in the low frequency ranges concentrated around 2-4 Hz, right after epoch beginnings, uncorrelated with where the spike-counts are low. Bottom panel shows the spike count in each time window with 100 ms duration, slided every 50 ms, summed over all the trials for target 3, from one session of monkey C. Top panels show the spectrotemporal representation of the three spike-field coupling measures: phase-locking value (PLV), pairwise-phase consistency (PPC), and spike-field coherence (SFC), from left to right, with separate

color bars for each measure. Y-axis from each top panel marks frequencies from 2 Hz to 80 Hz. Gray lines on the x-axis in all panels mark the onset of different epochs in trial: fixation, cue, delay, and response.

Monkey C's sorted single units were mostly from area PFC, while area SEF contained channels that had the most saccade information. In addition to the tendency to increase spike-field coupling in < 4 Hz band during the beginning of target and response epochs, one unit from a SEF channel also exhibited increasing spike-field coupling in the 2-6 Hz range, in the target and response epochs (Figure 3.3A). Interestingly, this increase occurred for targets that were in the contralateral visual field (shown in Figure 3.3B).

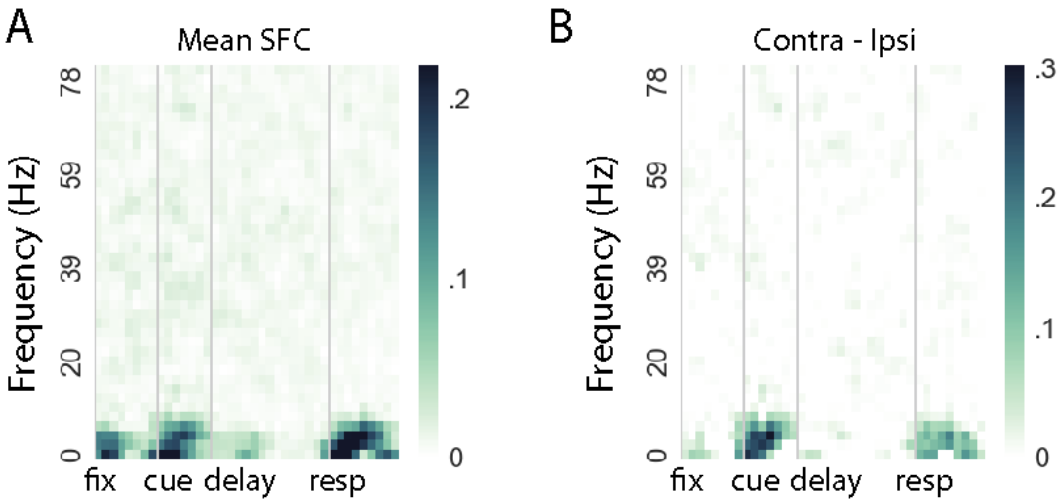

Figure 3.3. Spike-field coherence of one SEF unit for monkey C. On this SEF channel, increases in spike-field coherence (SFC) concentrated in 2-4 Hz in the beginning of target and response epochs like most other channels. Unlike most other channels, an additional distinct increase in the 2-6 Hz range was found during the target and response epochs, and is much stronger for targets in the contralateral visual field. A: mean SFC of all target conditions. B: mean difference in SFC between contralateral and ipsilateral targets.

Units for monkey J largely exhibited the same tendency to increase coupling strengths that were concentrated below 4 Hz, immediately after epoch onset. In addition, two units

from SEF also showed increased coupling strength in the beta band that lasted through the delay epoch for contralateral targets, one of which is shown in Figure 3.4.

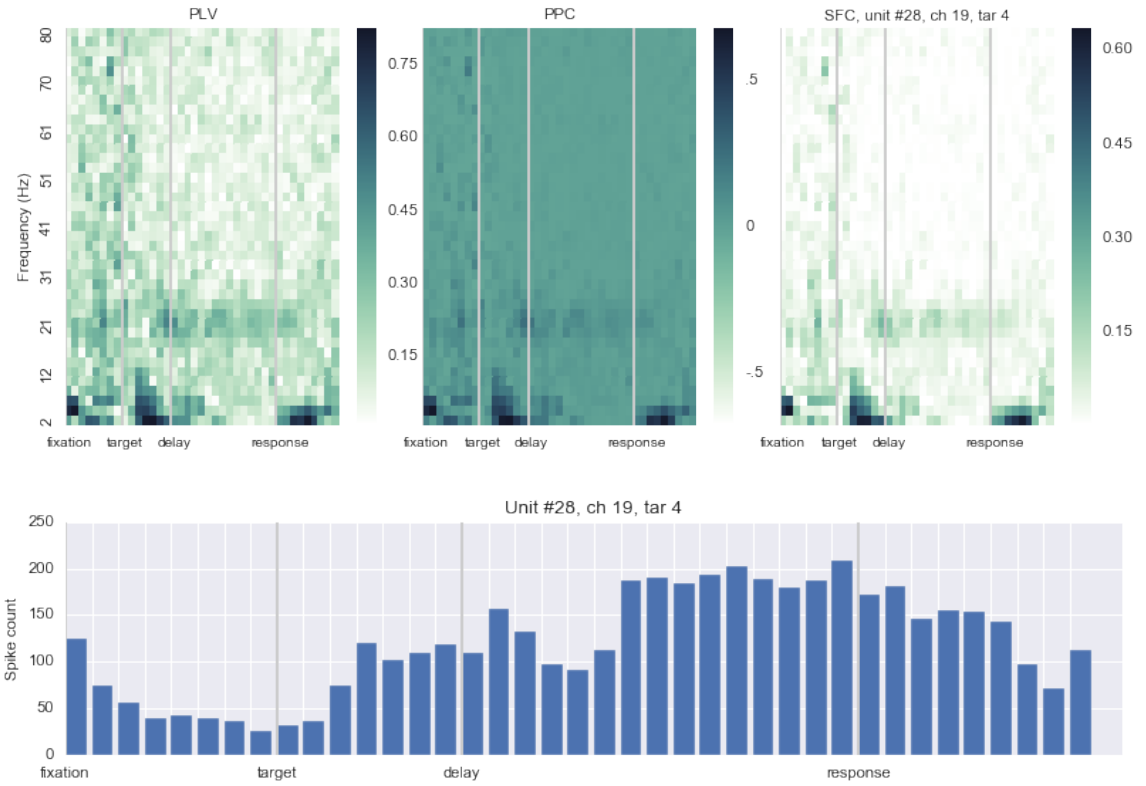

Figure 3.4. Increased spike-field coupling in beta band, on one SEF channel for monkey J. In addition to the increased coupling strength concentrated in 2-4 Hz, and 4-6 Hz, beta band also exhibited a sustained increase in coupling strength that started at the onset of the delay epoch. Bottom panel shows the spike count in each window with 100 ms duration, slided every 50 ms, summed over all the trials for target 2, from one session of monkey C. Top panels show the spectrotemporal representation of the three spike-field coupling measures: phase-locking value (PLV), pairwise-phase consistency (PPC), and spike-field coherence (SFC), from left to right, with separate color bars for each measure. Y-axis from each top panel marks frequencies from 2 Hz to 80 Hz. Gray lines on the x-axis in all panels mark the onset of different epochs in trial: fixation, cue, delay, and response.

In theory (Vinck *et al.*, 2010, 2012), SFC, PLV, and PPC reflect different aspects of spike-field coupling. In this work, they were found to be highly correlated with each

other, therefore highly redundant measures reflecting the same relationship between spikes and the local field potentials. Figure 3.5 shows scatterplots of all three measures plotted against each other, with Pearson correlation coefficients and two-tailed p-values reported to quantify how linear the relationship between coupling measures is, and how significant the linear relationship is (a Pearson correlation coefficient of 1 implies that the relationship between variables is perfectly linear, and 0 implies lack of any linear relationship). In this analysis, only units with a sufficient number of spikes (> 40 spikes in each individual time bin after pooling trials with the same target) were included, and combined across all frequencies (1-80 Hz), all time bins, as well as all six target conditions. For both monkeys, all three pairs of coupling measures (SFC - PLV, SFC - PPC, PLV - PPC) had high Pearson correlation coefficients, and showed significant linear correlations.

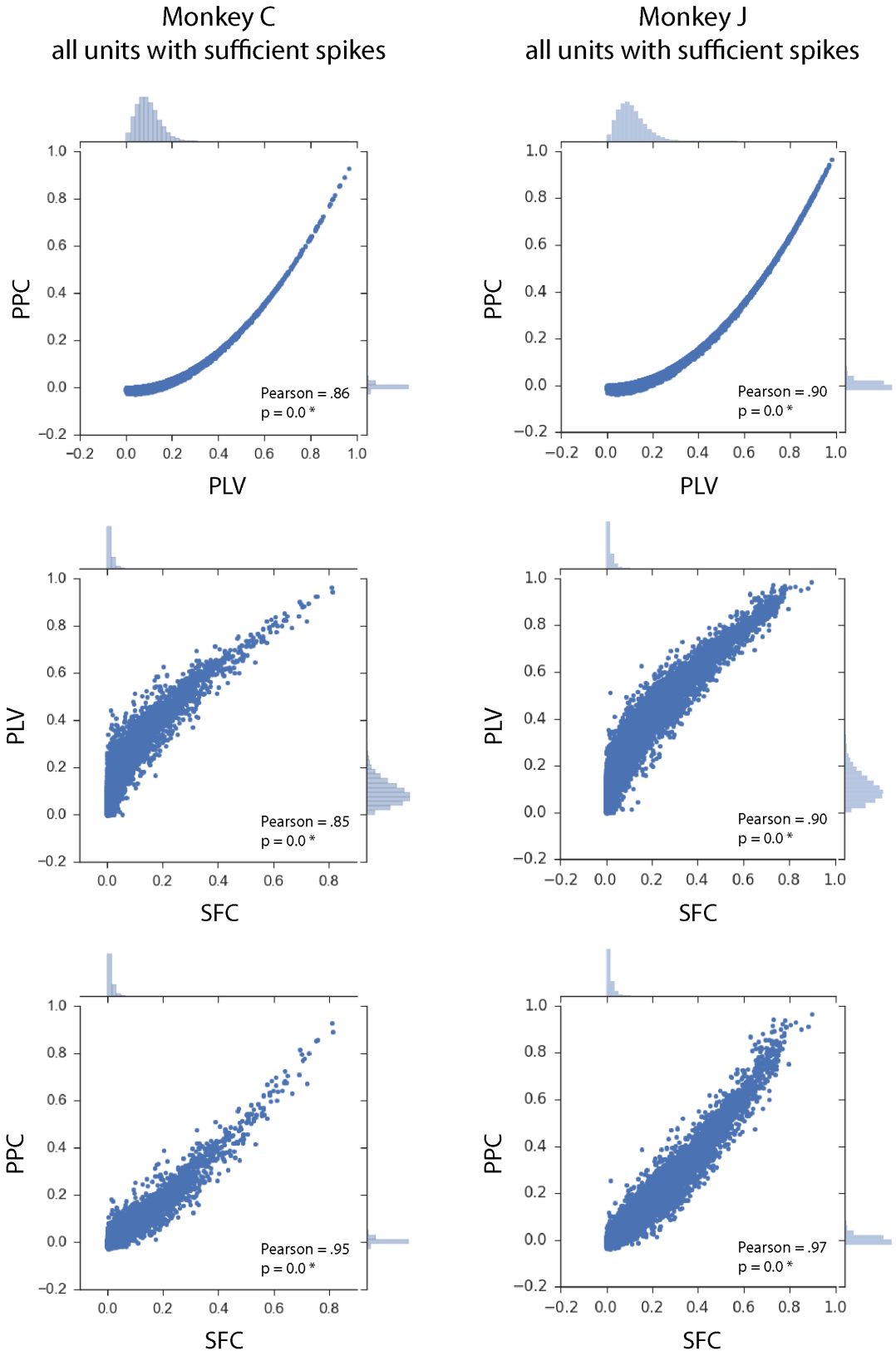
Monkey C
all units with sufficient spikes
Monkey J
all units with sufficient spikes
PPC
PLV
Pearson = .86
p = 0.0 *
PLV
PPC
Pearson = .90
p = 0.0 *
PLV
SFC
Pearson = .85
p = 0.0 *
PLV
SFC
Pearson = .90
p = 0.0 *
PPC
SFC
Pearson = .95
p = 0.0 *
PPC
SFC
Pearson = .97
p = 0.0 *

Figure 3.5. Scatterplots of three pairs of spike-field coupling measures: PPC-PLV, PLV-SFC, and PPC-SFC. All pairs show significantly high linear correlations, for both monkeys. Pearson correlation coefficient and two-tailed p-value are reported for each individual scatterplot. Histograms of the two coupling measures are shown on the top and right side of each scatterplot, for the coupling measures on the x-axis and y-axis, respectively.

Because all three measures were highly redundant, only SFC was used to summarize changes in spike-field coupling strength in trial in Figure 3.6A. For both monkeys, the average increase in spike-field coupling occurred mostly in the frequency range below 8 Hz, during the fixation epoch, the cue epoch, and especially the response epoch. This is consistent with the previous examples shown in Figures 3.2, 3.3, and 3.4, where coupling strengths below 8 Hz increased right after epoch onsets, when visual cue either disappeared from the display screen, or was added to it, to signal to the monkeys about epoch change (Figure 2.2 shows visual stimulus presentation in difference epochs. The increased coupling strength can potentially indicate responses to visual stimulus change, or reflect a cognitive state change registered by the change in visual stimulus. Laterality of the target location also appears to have an effect on spike-field coupling. For both monkeys, spike-field coupling is stronger for contralateral targets (Figure 3.6B) during the cue period in the frequency band < 8 Hz, consistent with results in Figure 3.3B. The prevalence of this spike-field coupling increase in the low frequency band across multiple brain regions indicates it is a broad effect, potentially generated by the same underlying neural mechanism.

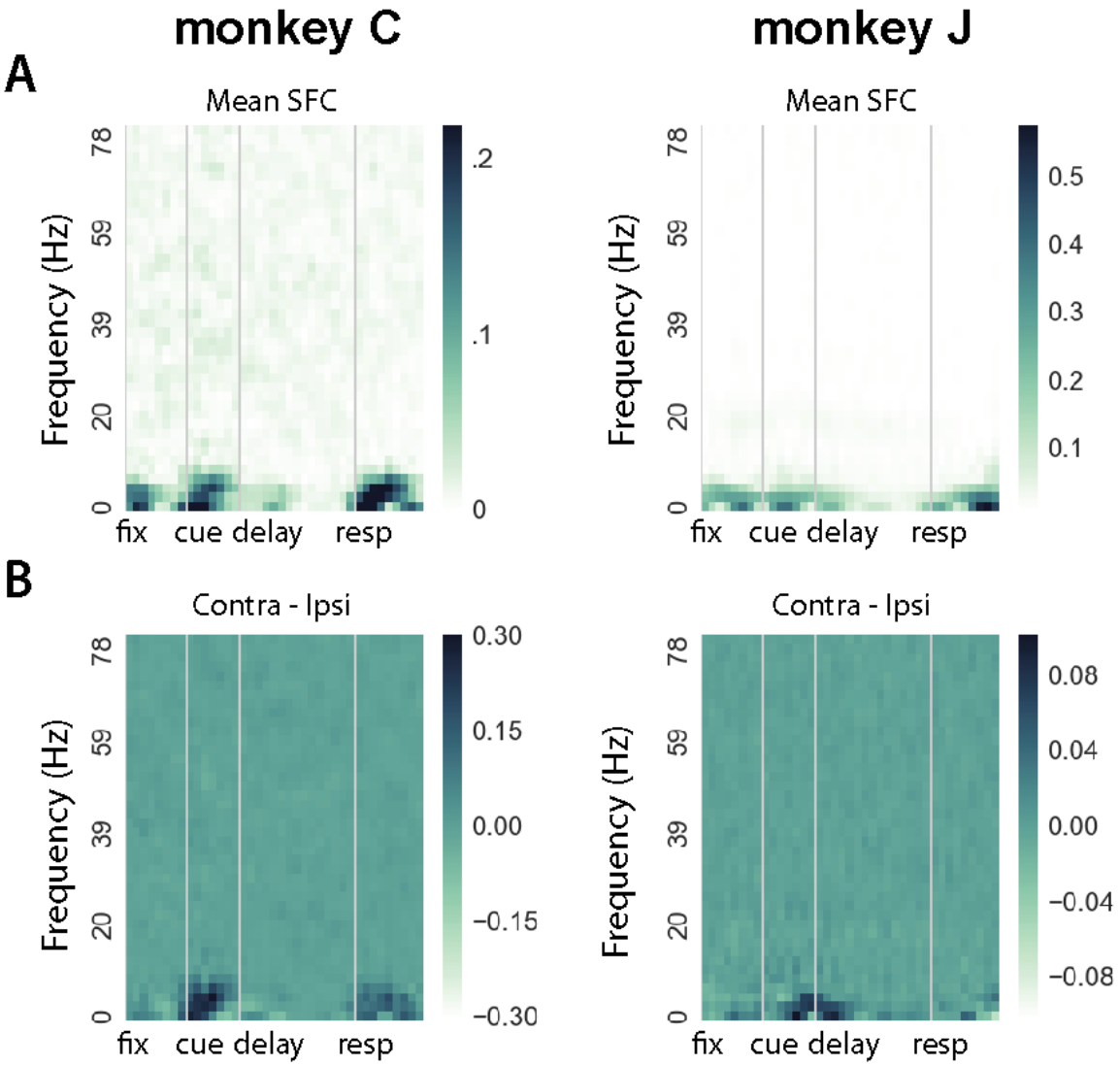

Figure 3.6. Spike-field coupling strength in trial, both monkeys. A: average spike-field coherence (SFC) across six target conditions. B: average SFC difference between contralateral and ipsilateral targets. Y-axis show frequencies from 0 Hz to 80 Hz. Gray lines on the x-axis mark the onset of different epochs in trial: fixation, cue, delay, and response.

3.3.2. Field-field coupling measures

Unlike spike-field coupling measures that were applied to spikes and LFPs on the same recording electrodes, field-field coupling measures were computed for LFPs from

different recording electrodes. Each monkey was implanted with three 32-channel arrays, therefore a total of 4560 unique pairs of channels to inspect per monkey.

Similar to results from spike-field coupling, coherence, PLV, and PPC were found to be highly redundant to each other. Figure 3.7 shows the scatterplots of the three measures computed for one example pair of channels for each monkey, with high values of Pearson correlation coefficients and significant p-values (two-tailed). High Pearson correlation coefficients and significant p-values were found for all pairs of channels for both monkeys. Because all three measures are highly redundant to each other, we chose to only report coherence hereafter, since it provides a natural segue into canonical coherence.

We found highly dynamic interactions between all the channels. Different frequency bands exhibited different coupling patterns, between different brain regions and task epochs. Due to the complexity of the data, the order of results will be presented as follows, for each monkey: first, we pick one channel to anchor subsequent results, and present coupling strength in coherence between this channel and another selected channel; we then look for a frequency band of interest, and show coupling profile on a larger scale, between the same channel and all other channels in the frequency band of interest; the results are then summarized for both monkeys based on each implant region; lastly, canonical coherence results are presented to provide a complementary description of the interactions in different frequency bands between implant regions.

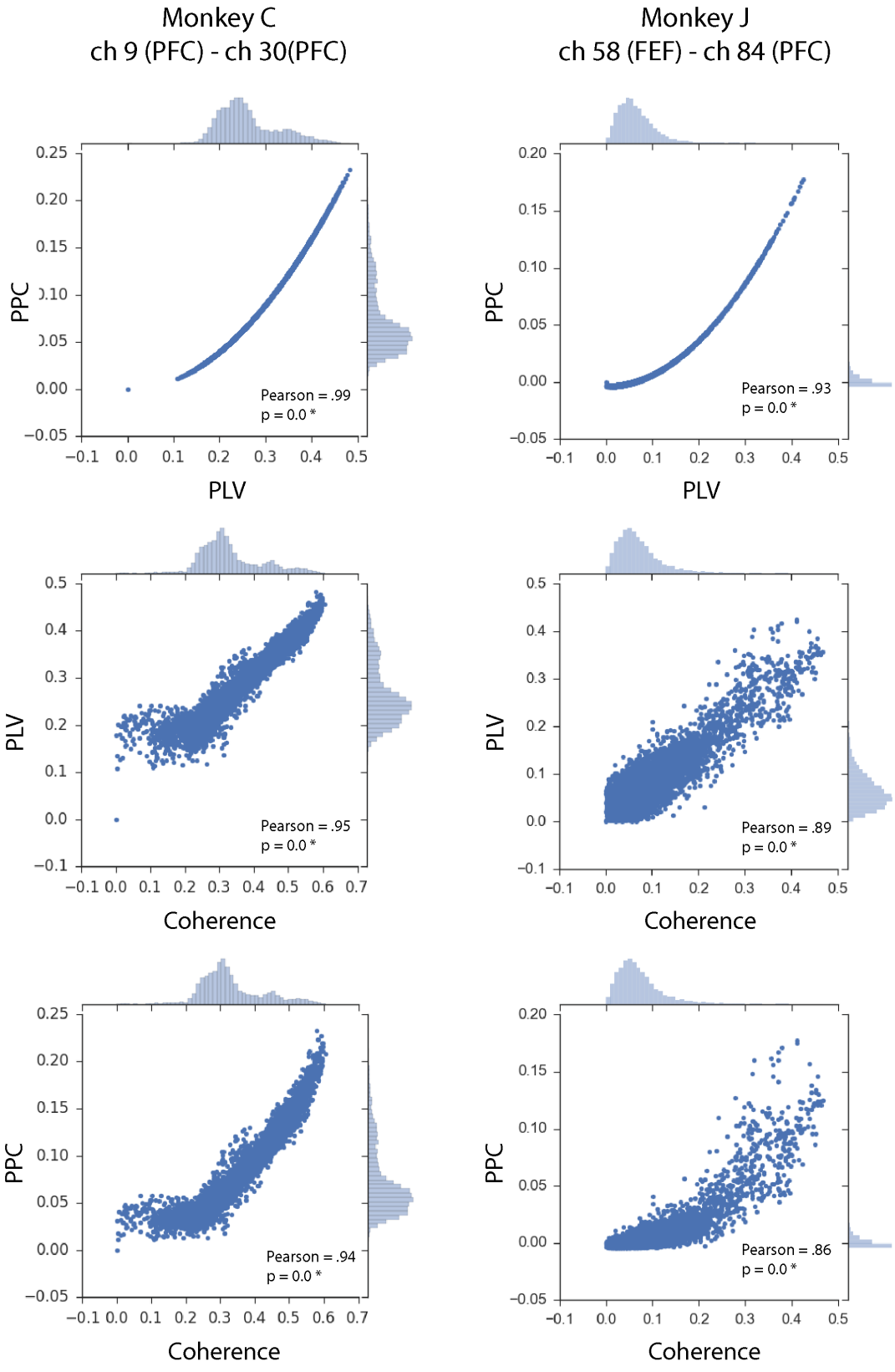
Monkey C
ch 9 (PFC) - ch 30(PFC)
Monkey J
ch 58 (FEF) - ch 84 (PFC)
PPC
PLV
Pearson = .99
p = 0.0 *
PLV
PPC
Pearson = .93
p = 0.0 *
PLV
Coherence
Pearson = .95
p = 0.0 *
PLV
Coherence
Pearson = .89
p = 0.0 *
PPC
Coherence
Pearson = .94
p = 0.0 *
PPC
Coherence
Pearson = .86
p = 0.0 *

Figure 3.7. Scatterplots of three pairs of field-field coupling measures: PPC-PLV, PLV-Coherence, and PPC-Coherence. All pairs show significantly high linear correlations, for both monkeys. Pearson correlation coefficient and two-tailed p-value are reported for each individual scatterplot. Histograms of the two coupling measures are shown on the top and right side of each scatterplot, for the coupling measures on the x-axis and y-axis, respectively.

Coherence and power spectrum

For monkey C, channel 9 from the PFC was picked as the example channel to facilitate further results and discussion. Coherence between channel 9 (PFC) and channel 30 (PFC) is shown for each of the six target conditions, and the explained variance (one-way ANOVA) in the coherence for target locations is also shown in Figure 3.8. Coherence in the beta band peaked during the delay period for contralateral targets, which are the three panels on the right, and is generally high during fixation and the cue epochs. Explained variance in this pair of channels showed a distinct cluster during the middle of the delay period in the beta band range, indicating that their functional coupling in the beta was affected by the laterality of the targets.

We now extend the coherence analysis, to include pairs of channels between channel 9 and all the channels for monkey C (Figure 3.9), with a focus on beta band since it was shown to be target selective and therefore highly relevant to the paradigm. Results from all 95 pairs of channels (i.e. between channel 9 to the other 95 channels) were combined and shown in Figure 3.9.

On channel 9 (PFC), beta band power was target selective during the delay epoch and to a lesser extent during the cue epoch (Figure 3.9, 'Power spectrum explained variance'). Generally, PFC channels exhibited target selectivity during the delay period (Figure 3.9, 'Explained variance power [15 30] Hz', all channels in PFC show increased explained variance during the delay period).

Coherence in the beta band from channel 9 to all other channels largely exhibited the same trend (Figure 3.9, 'Coherence [15 30] Hz', in which coherence between channel 9 and all other channels peak at roughly the same time during the delay period). Interestingly, even though coherence increased between channel 9 and all other channels during the delay period, target selectivity in the beta band coherence existed mostly between channel 9 and other PFC channels (Figure 3.9, 'Explained variance coherence [15 30] Hz', only PFC channels show peaks in explained variance during the delay period), suggesting that the beta band coherence was primarily a local function with area PFC.

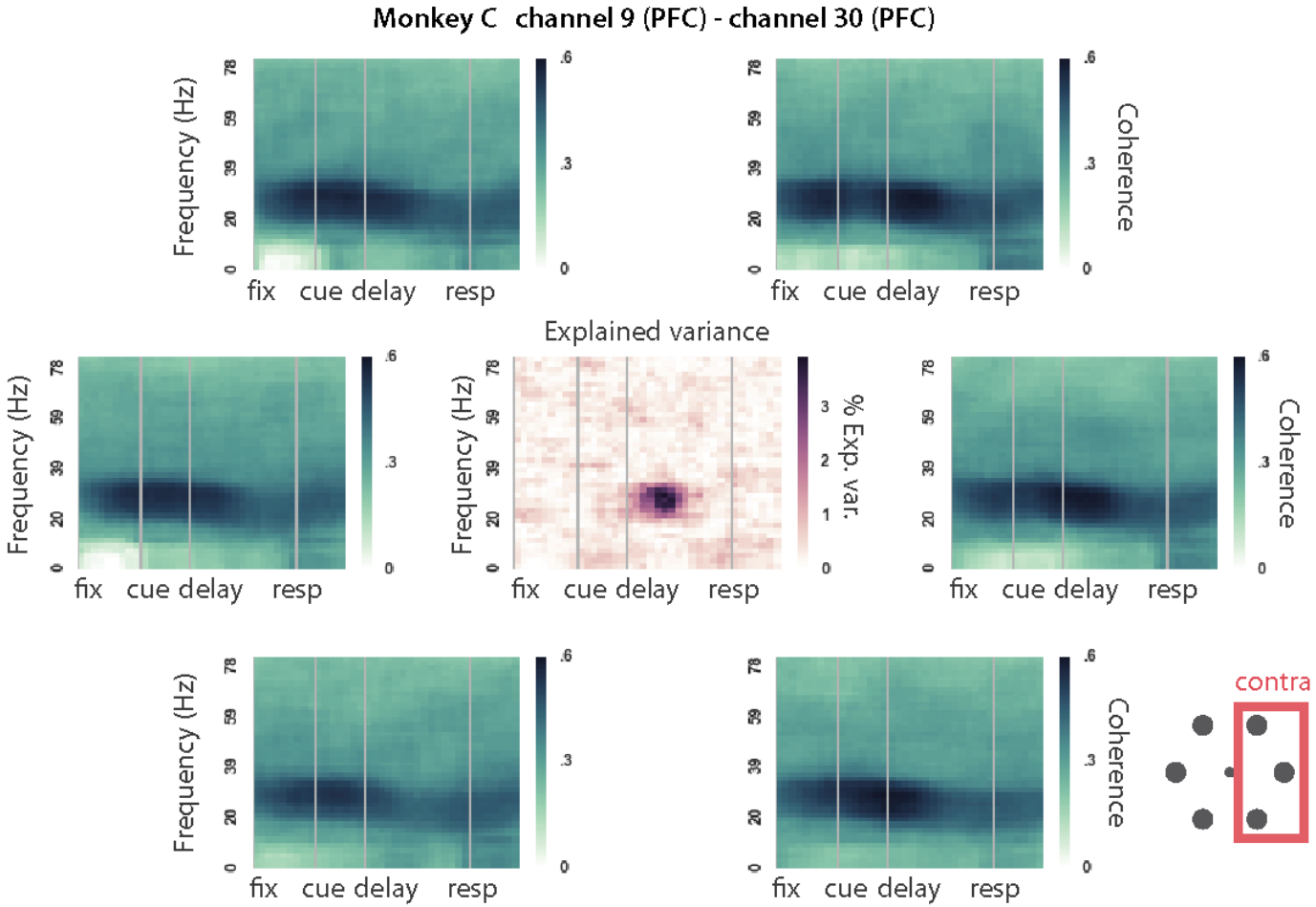

Figure 3.8. Coherence between channel 9 (PFC) and channel 30 (PFC) for monkey C. Each one of the six outlying panels shows coherence in trial for its corresponding target location. Central panel: explained variance in coherence. Gray lines on the x-axis mark the onset of different epochs in trial: fixation, cue, delay, and response. Contralateral target locations ('contra') are indicated in a red rectangle in the bottom right.

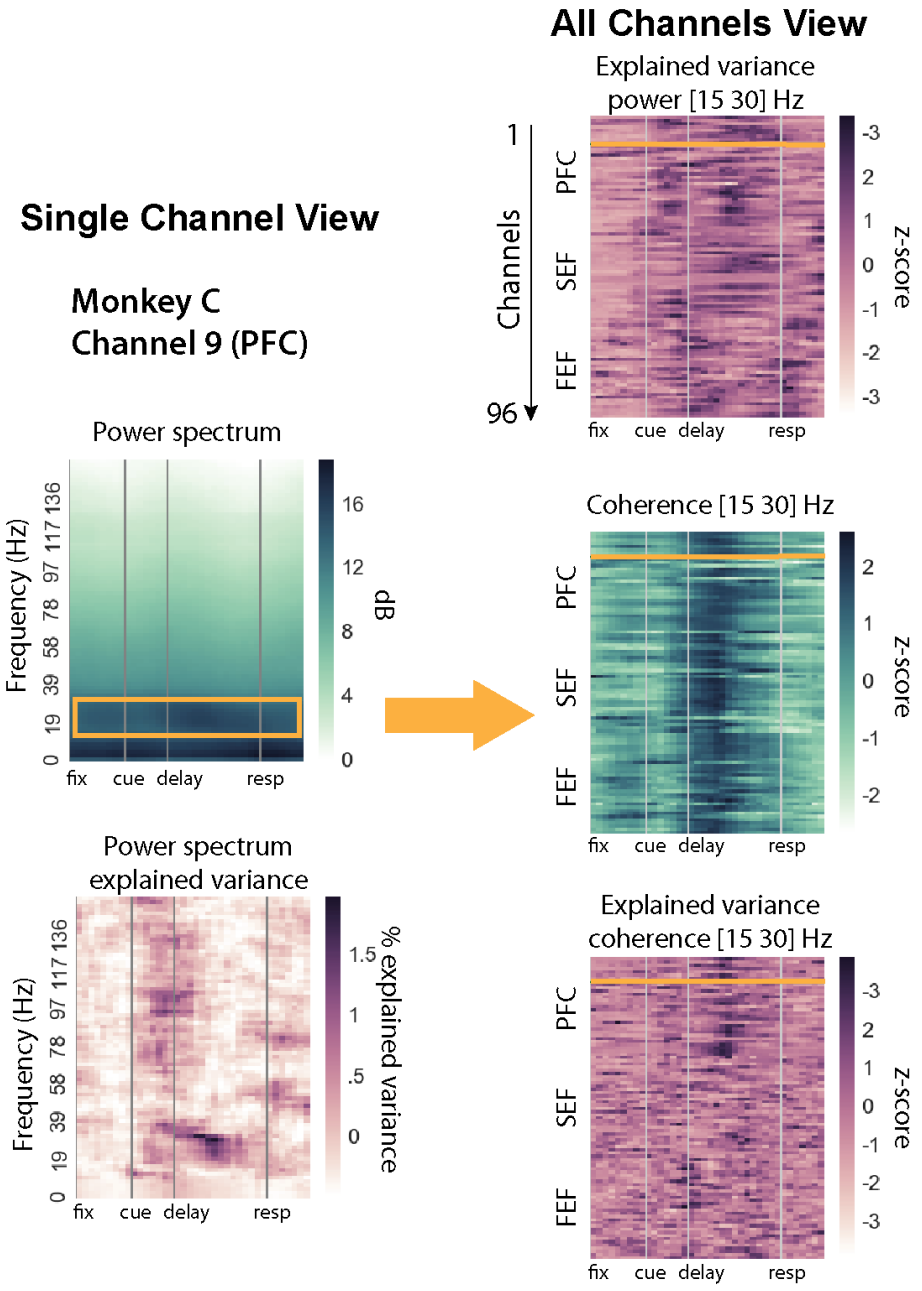

Figure 3.9. Coupling strength in 13-30 Hz frequency band from channel 9 (PFC) to all other channels, monkey C. Panels on the left side show the average power spectrum of all target conditions ('Power spectrum', top left) and its explained variance ('Power spectrum explained variance', bottom left) of the channel. Orange box highlights 13-30 Hz in the spectrogram. Panels on the right side show explained variance in the 13-30 Hz power spectrum across all channels ('Explained variance power [13 30] Hz', top right), average coherence from channel 9 to all other channels for all target conditions ('Coherence [13 30] Hz', middle right), and explained variance in coherence ('Explained

variance coherence [13 30]', bottom right). Y-axis in the right panels marks all electrodes ordered by their implant location. Orange line indicates channel 9's position and its array location. All measures in the right panels were z-score normalized for ease of visual comparison. Gray lines on the x-axis mark the onset of different epochs in trial: fixation, target, cue, and response.

For monkey J, channel 58 from the FEF was picked as the example channel to facilitate the discussion. Coherence between channel 58 (FEF) and channel 84 (PFC) is shown in Figure 3.10 for each of the six target conditions, as well as its explained variance (one-way ANOVA). Similar to the example channel used for monkey C, coherence in the beta band also exhibited target selectivity for this pair of channels during the delay epoch. Coherence in the beta band was sustained throughout the delay epoch for targets on the ipsilateral side ($0°, 300°$) throughout the entire delay, whereas for targets located at $120°$ and $180°$ on the contralateral side, coherence was stronger in the early delay epoch and dissipated more quickly. Explained variance for this pair of channels was concentrated in the latter half of the delay epoch in the beta band, and also in the 8-12 Hz range (alpha/mu band) in the response epoch.

We now extend the coherence analysis to include pairs of channels between channel 58 and all other channels for monkey J (Figure 3.12), also with the beta band selected as the frequency band of interest, similar to the example channel for monkey C. Results from all 95 pairs of channels (i.e. between channel 58 to the other 95 channels) were combined and shown in Figure 3.11.

On channel 58 (FEF), power in the beta band was target selective in the latter half of the

delay period (Figure 3.11, ‘Power spectrum explained variance’). Generally, for FEF channels, beta band showed the strongest selectivity of target location in the cue epoch, and milder selectivity late in the delay period (Figure 3.11, ‘Explained variance power [15 30] Hz’). By comparison, target selectivity for SEF channels peaked around delay onset, and showed a second increase towards the end of the delay epoch. While for PFC channels, target selectivity peaked during the early delay period. Differences in target selectivity pattern in this example also suggest that the beta band serves different functions for each brain region, as target information shows very distinct patterns in each region, consistent with the example channel for monkey C.

Coherence in the beta band between channel 58 (FEF) and channels in the FEF and SEF were similar (Figure 3.11, ‘Coherence [15 30] Hz). But between the same channel and PFC channels, coherence peaked in the transition period between the cue and the delay epochs. The coherence pattern did not necessarily translate into target selectivity, as the late delay epoch showed the strongest target selectivity in coherence with slightly earlier timing between channel 58 and FEF channels, than between channel 58 and SEF channels, while no clear target selectivity was observed in the coherence between channel 58 and PFC channels (Figure 3.11, ‘Explained variance coherence [13 30] Hz’, FEF channels show earlier peaks than SEF channels, and no clear peak is seen for PFC channels). Again, similar to the example channel for monkey C, coupling in the beta band was very dynamic between brain areas, and potentially serves different roles in each region.

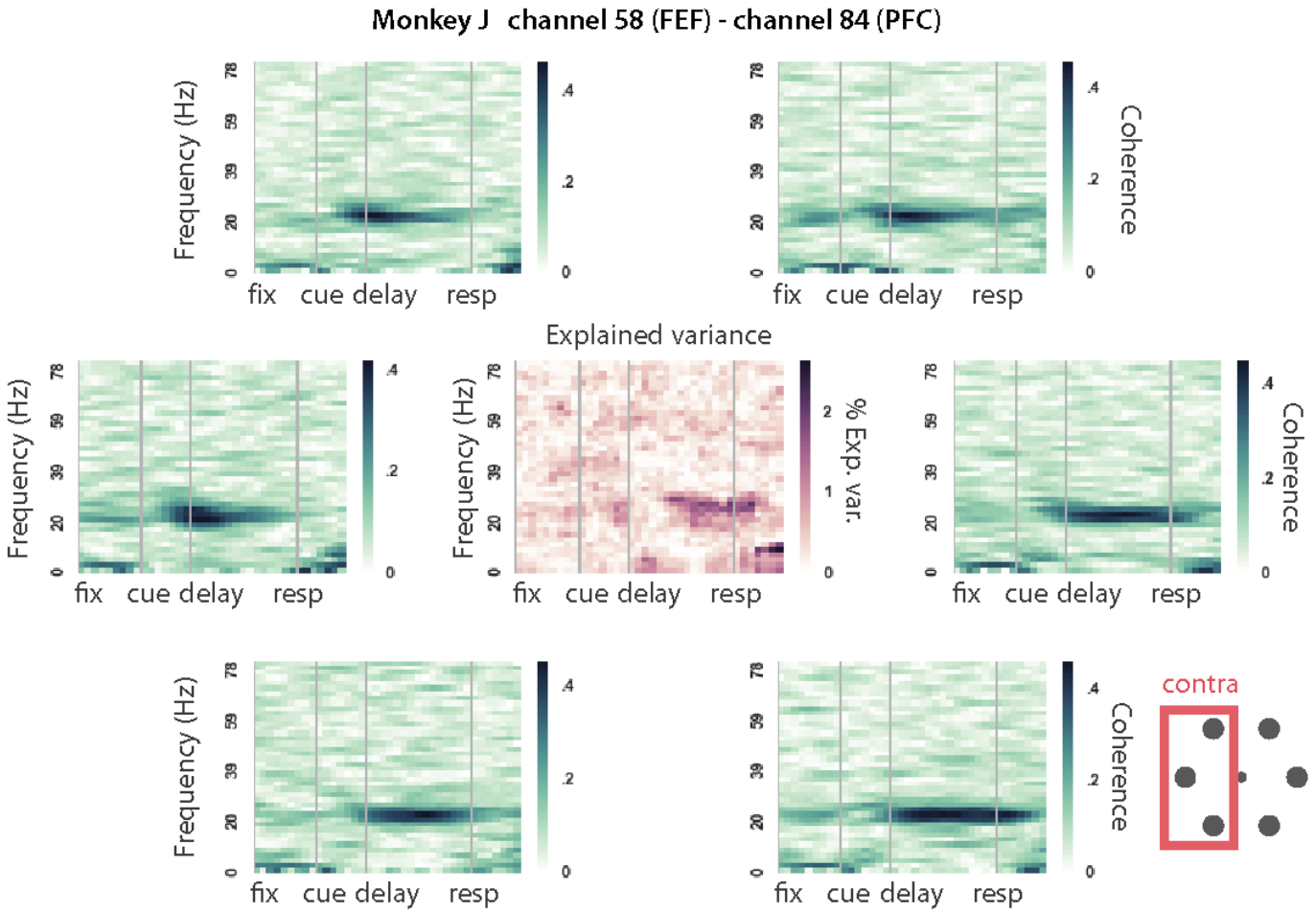

Figure 3.10. Coherence between channel 58 (FEF) and channel 84 (PFC) for monkey J. Each one of the six outlying panels shows coherence in trial for its corresponding target location. Central panel: explained variance in coherence. Gray lines on the x-axis mark the onset of different epochs in trial: fixation, cue, delay, and response. Contralateral target locations ('contra') are indicated in a red rectangle in the bottom right

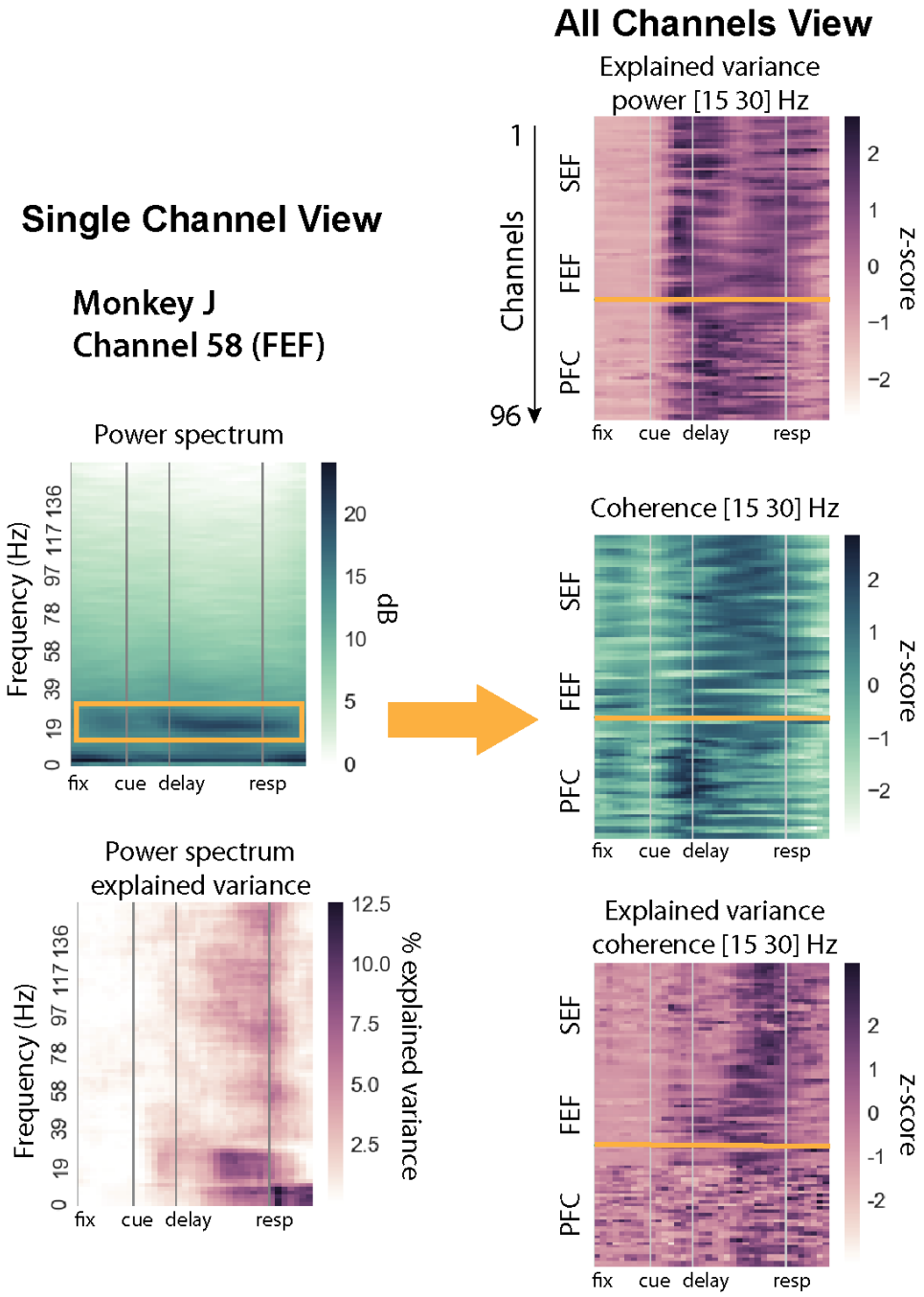

Figure 3.11. Coupling strength in 13-30 Hz frequency band from channel 58 (FEF) to all other channels, monkey J. Panels on the left side show the average power spectrum of all target conditions ('Power spectrum', top left) and its explained variance ('Power spectrum explained variance', bottom left) of the channel. Orange box highlights 13-30 Hz in the spectrogram. Panels on the right side show explained variance in the 13-30 Hz power spectrum across all channels ('Explained variance power [13 30] Hz', top right), average coherence from channel 58 to all other channels for all target conditions

('Coherence [13 30] Hz', middle right), and explained variance in coherence ('Explained variance coherence [13 30]', bottom right). Y-axis in the right panels marks all electrodes ordered by their implant location. Orange line indicates channel 58's position and its array location. All measures in the right panels were z-score normalized for ease of visual comparison. Gray lines on the x-axis mark the onset of different epochs in trial: fixation, target, delay, and response.

From these two example channels, we observed that the target information distribution patterns in the beta band were highly similar for channels from the same region ('Explained variance power [15 30] Hz', Figure 3.9 and 3.11). The same observation holds true for target information in coherence in the beta band ('Coherence [15 30] Hz', 'Explained variance coherence [15 30] Hz', Figure 3.9 and 3.11). Even though the amount of target information can differ between different channels on the same array, the overall trend (e.g., peaks and troughs) is largely similar on an area to area basis. For this dataset, this observation is generalizable to all frequency bands considered. Therefore, we can summarize the distribution of target information that existed in the power spectra and coherence, for each area, by averaging across all channels in the same area, while not losing much detail in individual channels.

Target information (quantified as explained variance) in the power spectra of all channels from the same implant region was averaged for each time-frequency point, for each monkey, and shown in Figure 3.12. For both monkeys, beta band, alpha/mu band, and <10 Hz band displayed target information, however the patterns were distinct between two subjects. Noticeably for monkey C, the beta band stands out during the delay epoch in PFC only, while the alpha/mu band stands out during the cue and response epochs in

SEF. For monkey J, the low gamma (30-60 Hz) was relevant during early delay epoch in SEF and later delay epoch in FEF, while the beta band target information peaked late in the cue epoch in FEF, early in the delay epoch in SEF, and sustained throughout the delay epoch in PFC.

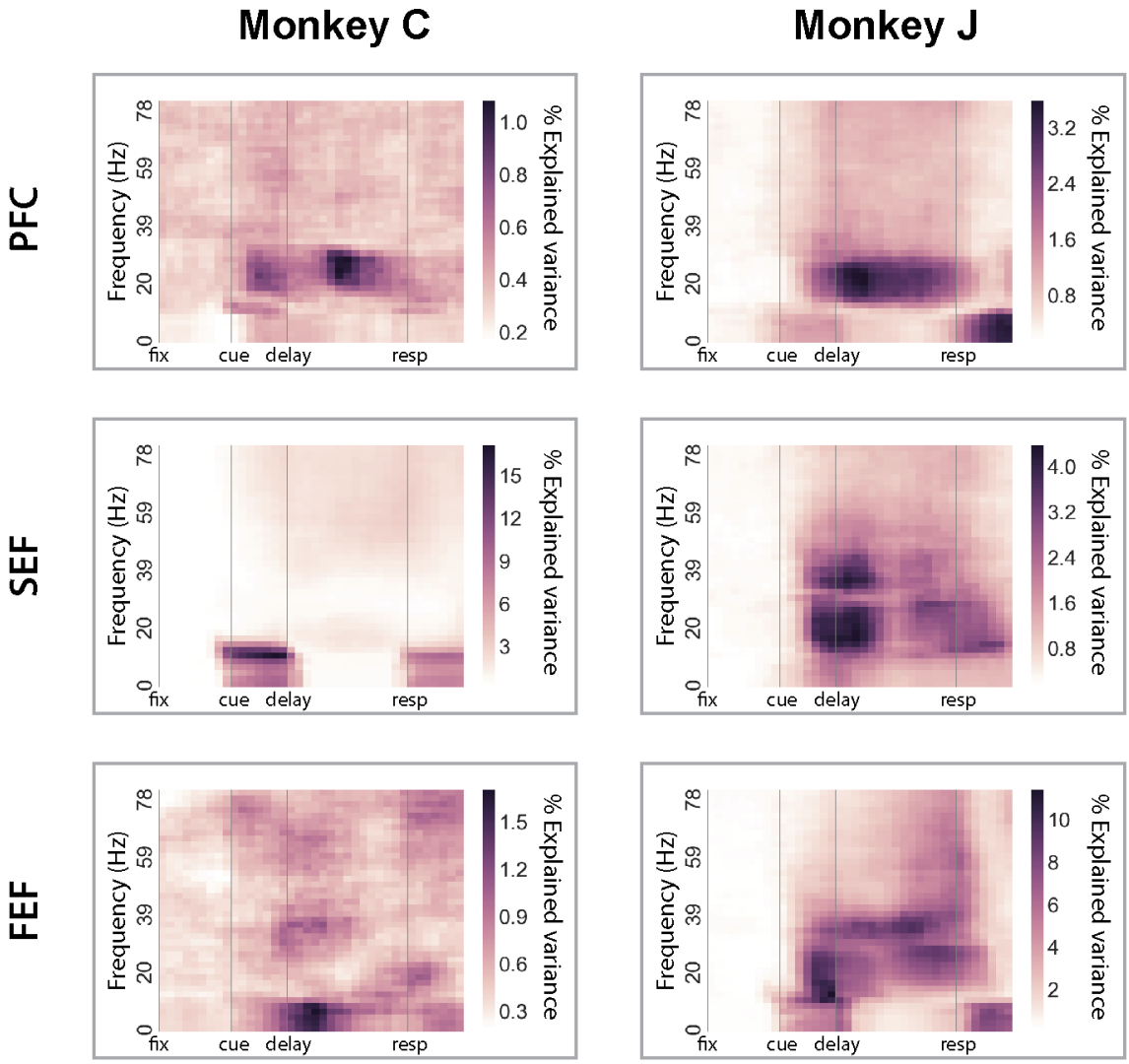

Figure 3.12. Target information distributions in LFP power, for PFC, SEF, and FEF. Mean percent explained variance of all channels in the same area is plotted for each area in each monkey.

To show target information in the coherence, the explained variance between channels from the same implant area (within-region), or between channels from different implant areas (inter-region) was averaged for each time-frequency point, to produce the mean explained coherence for six pairs of areas (within-region pairs: PFC-PFC, SEF-SEF, FEF-FEF, inter-region pairs: PFC-SEF, PFC-FEF, SEF-FEF) shown in Figure 3.13 for monkey C, and Figure 3.14 for monkey J.

The beta band was found to contain target information for both monkeys. In agreement with target information in the power spectrum, coherence in the PFC- PFC area pair in monkey C showed increased explained variance in the cue and mid-delay epochs. The PFC-FEF pair also contained increased target selectivity in the late delay epoch, but to a smaller extent as it contained less percent explained variance. Since target information (explained variance) was the highest in area PFC in the power spectrum, beta band target selectivity present in the coherence most likely originated within PFC itself. If we are allowed to assume that information flows from high content region to low content region, the implication is that the information flow was most likely directed from PFC to FEF during the delay epoch.

For monkey J, all pairs of areas show target selectivity in the beta band, predominantly during the delay epoch. Consistent with target information distribution in the power spectra (Figure 3.12), three distinct clusters in the beta band explained variance were observed. One was centered on late cue or very early delay epochs (Figure 3.14, SEF-

SEF, SEF-FEF, and FEF-FEF pairs). Another cluster was centered on early delay period and sustained throughout the delay period (Figure 3.14, PFC-PFC and PFC-SEF). The third cluster showed peaks in the late delay period (Figure 3.14, PFC-FEF, SEF-SEF, SEF-FEF, and FEF-FEF). For the spectrotemporal location of the first cluster, target information in the power spectra was highest in FEF, second weakest in the coherence of FEF-FEF pair, weaker in SEF-FEF, PFC-FEF, and SEF-SEF pairs. Again, assuming that information flows from high content region to low content region, the direction of target information flow was most likely from FEF to SEF and PFC. Using the same inference logic, target information was most likely from PFC to SEF for the second cluster, and from FEF to SEF and PFC for the third cluster. Thus for monkey J, target information flow in the beta band was likely in multiple directions during different epochs, originating from FEF in the late cue epoch, from PFC during the early delay epoch, and from FEF during the late delay epochs.

So far we have mostly discussed the beta band for the two example channels picked, yet the alpha/mu band (8-12 Hz) is also distinctive. For monkey C, the alpha/mu band power as well as < 8 Hz band power were strongly target selective during the cue and response epochs in all pairs of areas involving SEF (i.e., PFC-SEF, SEF-SEF, and SEF-FEF), and in the < 12 Hz band for FEF-FEF (Figure 3.12, SEF for Monkey C show increased target information during the cue and response epochs). While area PFC also showed target selectivity during the cue and response epochs, it was much weaker than in SEF. Coherence in the alpha/mu band contained target information during the cue and response

period, in SEF-PFC and SEF-FEF pairs (Figure 3.13), suggesting that target information was directed from SEF to PFC and FEF during the cue and response epochs. For monkey J, target selectivity is not as clearly confined to the alpha/mu band as in the case for monkey C. Target information is generally distributed in the < 12 Hz band during the cue and response epochs, similar to FEF-FEF area pair for monkey C. Target selectivity was strongest in FEF during the response epoch and milder during the cue epoch (Figure 3.12). PFC also shared the same trend but was less target selective than FEF. When taking in the consideration that target information in coherence in the < 12 Hz band was stronger for SEF-FEF and PFC-FEF than for other inter-region pairs (Figure 3.14), the flow of target information was most likely directed from FEF towards SEF and PFC. To summarize, the inferred direction of target information flow in the < 12 Hz band, was from SEF to the other two areas for monkey C, and from FEF for monkey J. Therefore, these findings indicate that the < 12 Hz band (including alpha/mu) could originate from different areas, but potentially serve similar purposes since it is active during the cue and response period regardless of the area of origination.

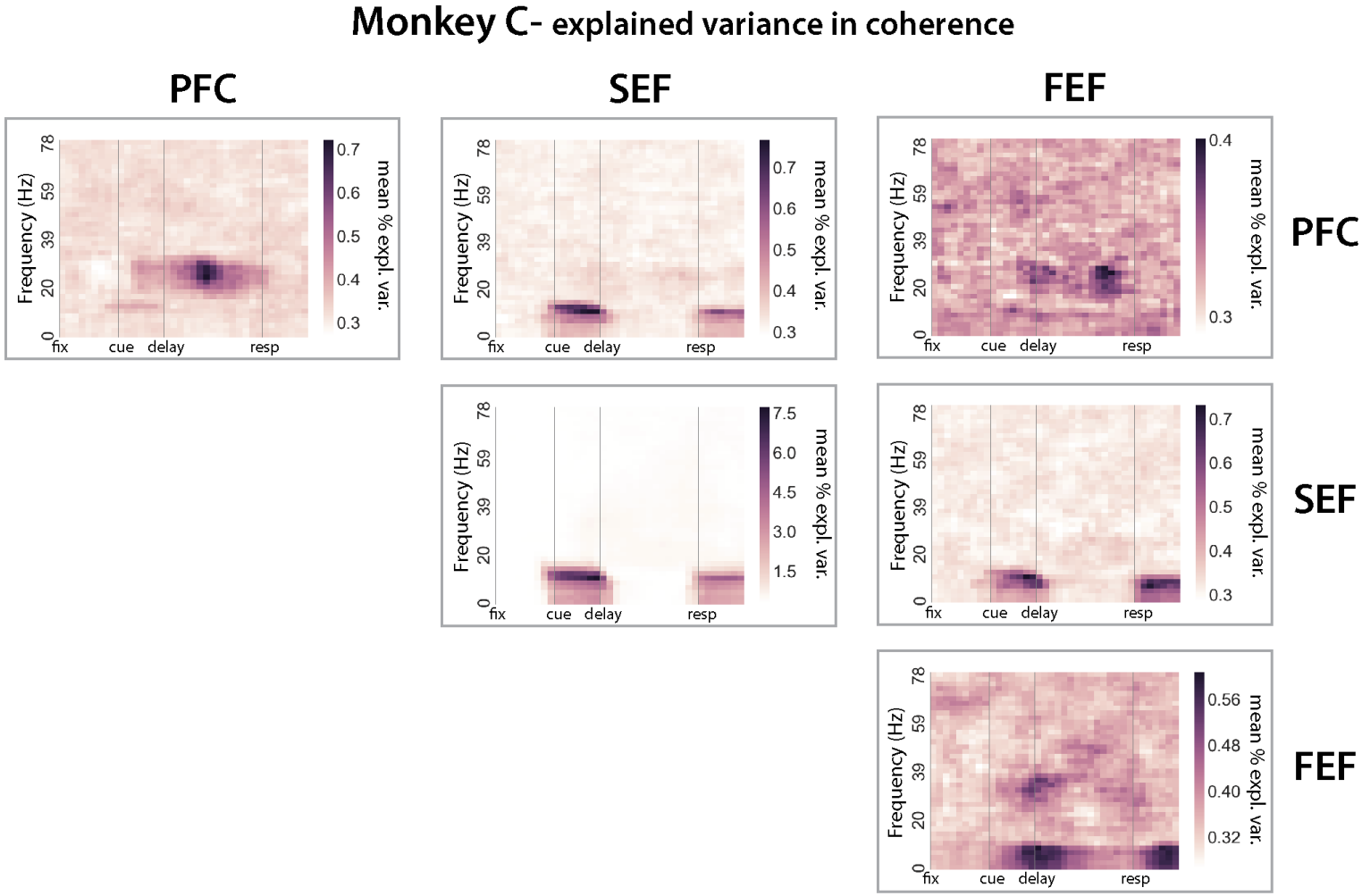

Figure 3.13. Target information in coherence for all pairs of implant areas, monkey C. Explained variance in the coherence of all pairs of channels within-region, and inter-region is averaged and shown, for six pairs of implant areas: PFC-PFC, PFC-SEF, PFC-FEF, SEF-SEF, SEF-FEF, and FEF-FEF. Each panel is placed in the corresponding area-area location.

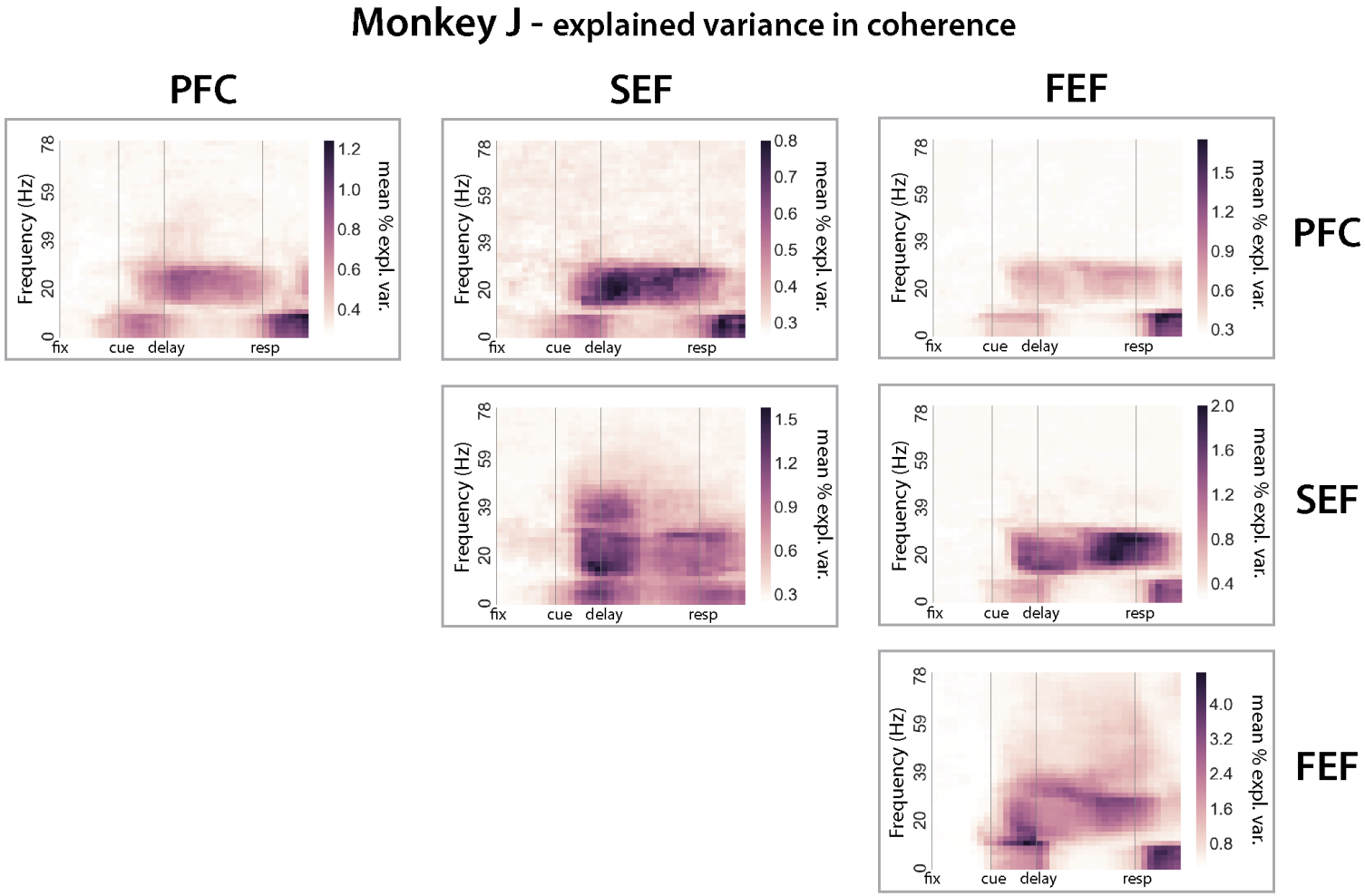

Figure 3.14. Target information in coherence for all pairs of implant areas, monkey J. Explained variance in the coherence of all pairs of channels within-region, and inter-region is averaged and shown, for six pairs of implant areas: PFC-PFC, PFC-SEF, PFC-FEF, SEF-SEF, SEF-FEF, and FEF-FEF. Each panel is placed in the corresponding area-area location.

Coherence between pairs of channels within the same implant area (within-region) was generally stronger than coherence between pairs of channels between different implant areas (inter-region) across all frequencies. Figures 3.15 and 3.16 show the distribution of coherence values in the beta band collected from pairs of channels according to their implant areas, for the duration of the entire trial for both monkeys. Both monkeys had higher means for within-region than for inter-region coherence distributions (indicated with red lines in Figures 3.15 and 3.16). We quantified the differences between the within-region and inter-region distributions, using Kullback-Leibler (KL) divergence, for which higher values indicate greater differences between the two distributions (KL divergences labeled in Figures 3.15 and 3.16 in both directions). We also tested for differences between distribution means using the rank sum test (indicated in Figures 3.15 and 3.16). KL divergences and rank sum tests were computed for 3 pairs of within-region distributions (1 for each area): PFC-PFC paired with SEF-SEF, PFC-PFC paired with FEF-FEF, SEF-SEF paired with FEF-FEF; and 6 pairs of inter-region distributions (2 for each area): PFC-PFC paired with PFC-SEF, PFC-PFC paired with PFC-FEF, SEF-SEF paired with PFC-SEF, SEF-SEF paired with SEF-FEF, FEF-FEF paired with PFC-FEF, FEF-FEF paired with SEF-FEF. For monkey C, all within-region coherence distribution means were significantly higher than inter-region distributions (e.g., PFC-PFC distribution is significantly different from PFC-SEF and PFC-FEF distributions), and KL divergences were lower between within-region distributions than inter-region distributions (average KL divergence of within-region distribution pairs in both directions: 0.09, average KL divergence of inter-region distribution pairs in both

directions: 3.15). For monkey J, while only PFC and FEF areas had significantly different distribution means (i.e., the PFC-PFC distribution mean was significantly higher than the PFC-FEF distribution mean, and the FEF-FEF mean was significantly higher than the PFC-FEF mean), the KL divergences were generally higher between inter-region distributions than within-region distributions (average KL divergence of within-region distribution pairs in both directions: 0.23, average KL divergence of within-region distribution pairs in both directions: 1.11). These results suggest coherence is predominantly an effect within the same brain region.

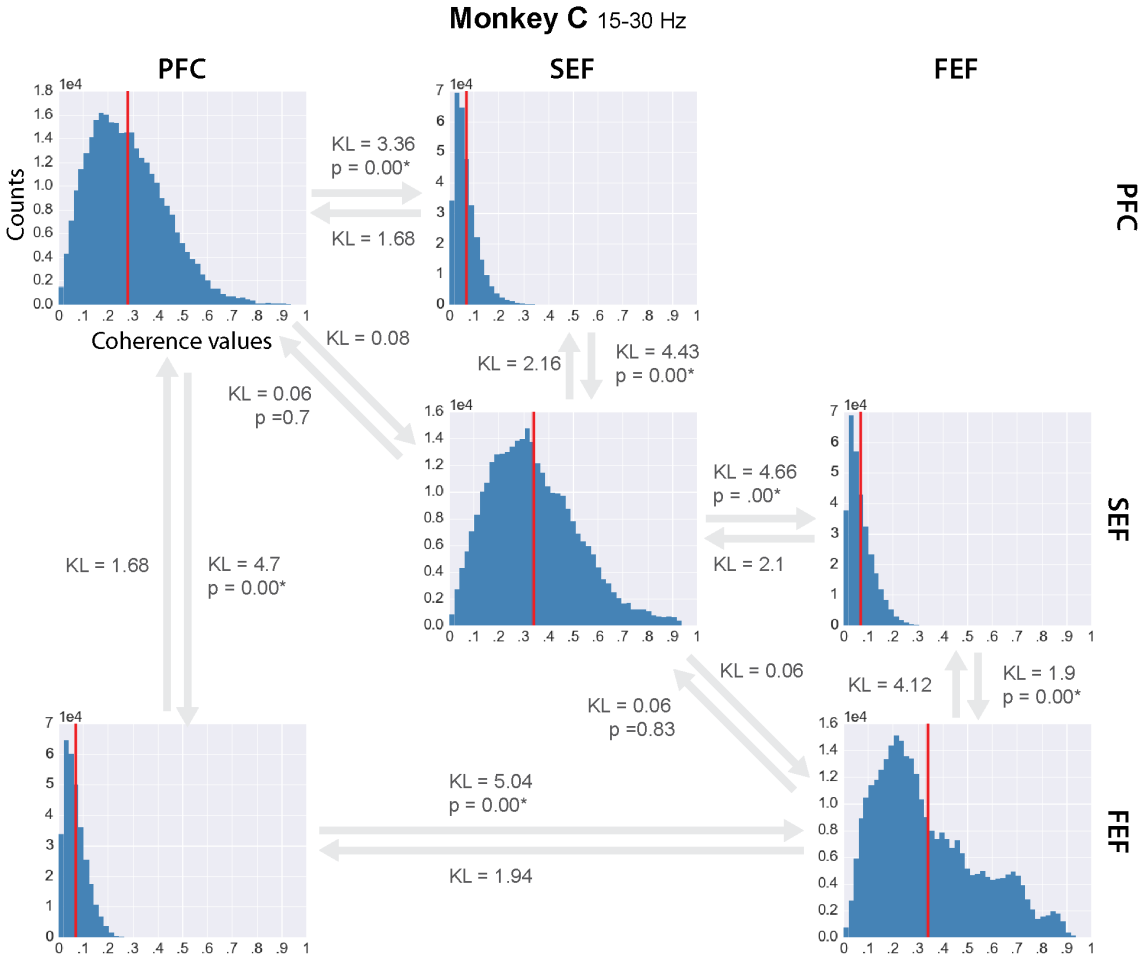

Figure 3.15. Distribution of coherence values in the 15-30 Hz beta band by implant regions, monkey C. Coherence values in the 15-30 Hz band are pooled from all trials. Red lines indicate mean of the distribution. Kullback-Leibler (KL) divergence values are labeled between distributions in the direction of the arrow, and p-values of rank sum tests are indicated. KL divergence from PFC-PFC to FEF-FEF and in the reverse direction: 0.1 and 0.16, rank sum p-value: 0.55 (unlabeled in the figure for visualization purposes).

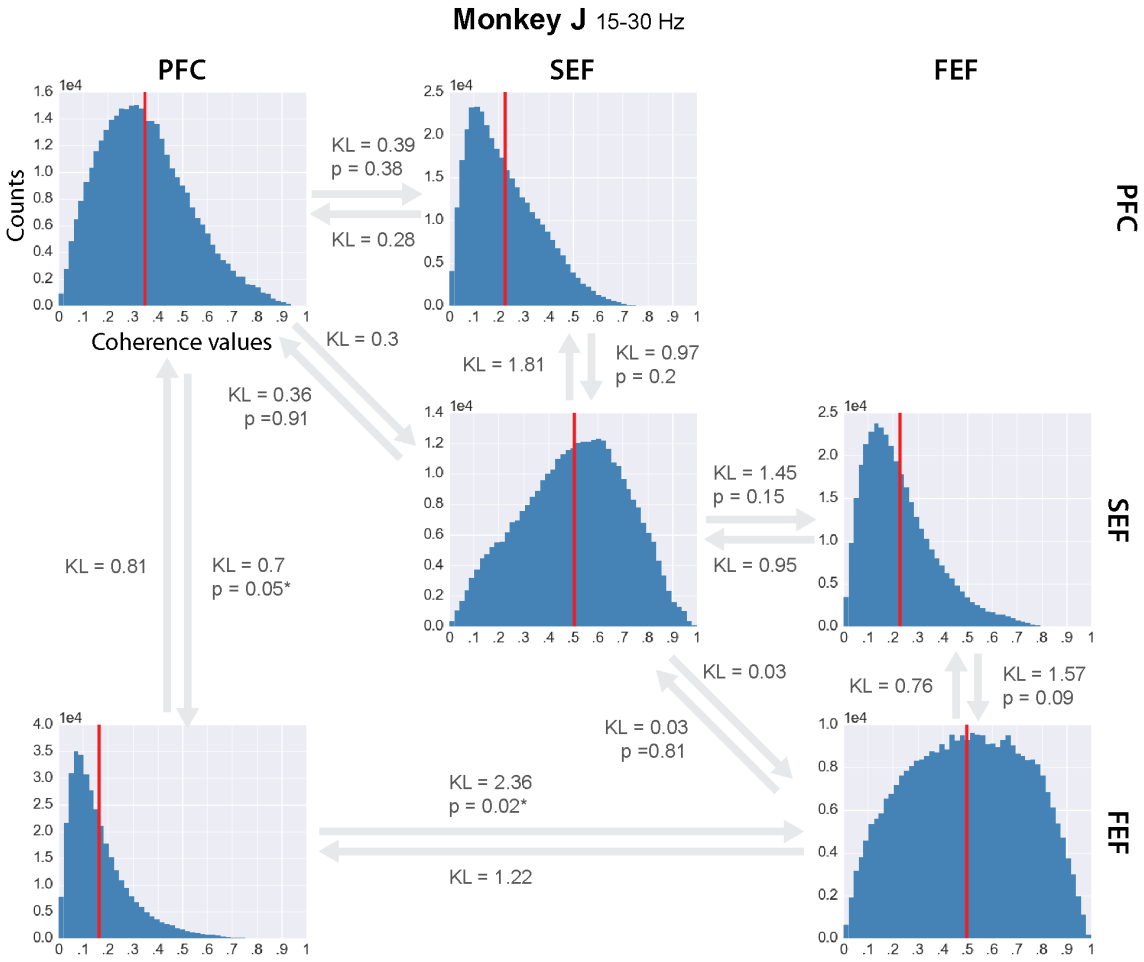

Figure 3.16. Distribution of coherence values in the 15-50 Hz beta band by implant regions, monkey J. Coherence values in the 15-30 Hz band are pooled from all trials. Red lines indicate mean of the distribution. Kullback-Leibler (KL) divergence values are labeled between distributions in the direction of the arrow, and p-values of rank sum tests are indicated. KL divergence from PFC-PFC to FEF-FEF and in the reverse direction: 0.26 and 0.4, rank sum p-value: 0.84 (unlabeled in the figure for visualization purposes).

Canonical coherence

One of the challenges faced in this exploratory data analysis is the combinatorial explosion of the number of channel pairs as the number of individual recording channels increases. As the dimensionality of the data grows, we lose the ability to represent a large

network of data in an intuitive manner for visualization and interpretation. For 96 channels from 3 different brain regions per monkey, we are looking at a network of 4560 unique pairs of channels, each with different frequency bands and distinct task epochs that form a network with high dimensionality. In this work, the use of canonical coherence provided a simplification to reduce the complexity of the network, by reducing the number of pairings from 4560 pairs of channels to 3 pairs of brain regions (a 1520-fold reduction in the number of dimensions). Instead of the cumbersome task of characterizing the interactions between each channel pair individually, the result from canonical coherence represents where the maximum covariance occurs in the spectrotemporal domain between pairs of different brain regions that each contain a number of channels. In other words, canonical coherence captures correlations in multivariate sets of variables, in this case 3 groups of channels, each from a distinct brain region. The coherence analysis serves to scrutinize individual pairs of channels in the network from a microscopic scale, while canonical coherence analysis aims to capture effects in the network from a macroscopic scale. Therefore, canonical coherence analysis provides a complementary description to coherence, which was found to be predominantly an effect within the same brain region, by quantifying between-region interactions. Since the three pairwise field-field coupling measures used (coherence, PLV, and PPC) were shown to be highly redundant, results of canonical coherence should also be considered as a valid extension of PLV and PPC in this work.

Canonical coherence was computed for 3 pairs of groups of channels: PFC-SEF, SEF-

FEF, and PFC-FEF. Each group of channels contained all the channels implanted in the same brain area; thus, every group contained 32 channels per monkey (Figures 3.17 and 3.19). Generally for both subjects, < 8 Hz band (1-4 Hz delta, 4-8 Hz theta) showed increased coupling strength during the fixation, cue, and response epochs, while beta band (20-30 Hz) showed increased coupling strength during the fixation and delay epochs. In the alpha/mu band (8-12 Hz), coupling strength increased during the beginning of the fixation epoch, the cue epoch, and during the response epoch. Laterality of the target conditions had an effect on both subjects (Figure 3.18 and 3.20). For both monkeys, coupling strength in the alpha/mu range increased during the cue epoch for contralateral targets, and in the delta range during the onset of the delay epoch. The details for each individual subject and the differences between them are described below.

The average canonical coherence of all six target conditions for monkey C is shown in Figure 3.17. For monkey C, the following frequency bands of interest stand out: beta (20-30 Hz), alpha/mu, theta, and delta. Out of these frequency bands, beta band canonical coherence was prevalent between all pairs of areas, with two distinct clusters within a trial: one during the fixation epoch, and another during the delay epoch. Increased coupling strength in the alpha/mu band was observed during the cue epoch between PFC and SEF. The strongest increase in functional coupling was observed in the < 8 Hz range including the delta and theta bands during the response period, between all pairs of areas.

Inspecting canonical coherence for each target condition also revealed an effect of

laterality, presented in Figure 3.18. Canonical coherence for each target condition between all three pairs of brain areas can be found in the Appendix (Section 3.5). The average difference in canonical coherence between contralateral target conditions and ipsilateral target conditions was computed, which revealed an effect in the < 12 Hz (1-4 Hz delta, 4-8 Hz theta, and 8-12 alpha/mu) band. When the target location was in the contralateral visual field, coupling strength was stronger in the theta band during the cue epoch, and in the delta band at delay onset, between all three pairs of brain areas.

For monkey J, patterns in functional coupling shared similarities but also showed differences from that of monkey C. The average canonical coherence of all target conditions is shown in Figure 3.19. The pattern in the beta band was largely similar to that of monkey C, with two distinct clusters within a trial: one during the fixation epoch, and the other during the delay period. Increase in coupling in the < 8 Hz band was observed during the cue epoch for PFC-FEF. Meanwhile, coupling in the same < 8 Hz band showed a decrease during the delay period for PFC-FEF and SEF-FEF. Where the coupling pattern differed from that of monkey C was an increase in coupling in the gamma range (30-60 Hz), observed during the delay epoch for SEF-FEF.

Laterality of targets also had an effect on coupling for monkey J (Figure 3.20), which was different from monkey C. When targets were located in the contralateral visual field, coupling in the 4-8 Hz band and the15-20 Hz band was stronger during cue and early epochs for PFC-FEF and SEF-FEF, in the < 4 Hz band during the delay epoch for PFC-

FEF and SEF-FEF. The beta band also showed laterality effect, although only for one monkey, between around delay onset for SEF-FEF and PFC-FEF.

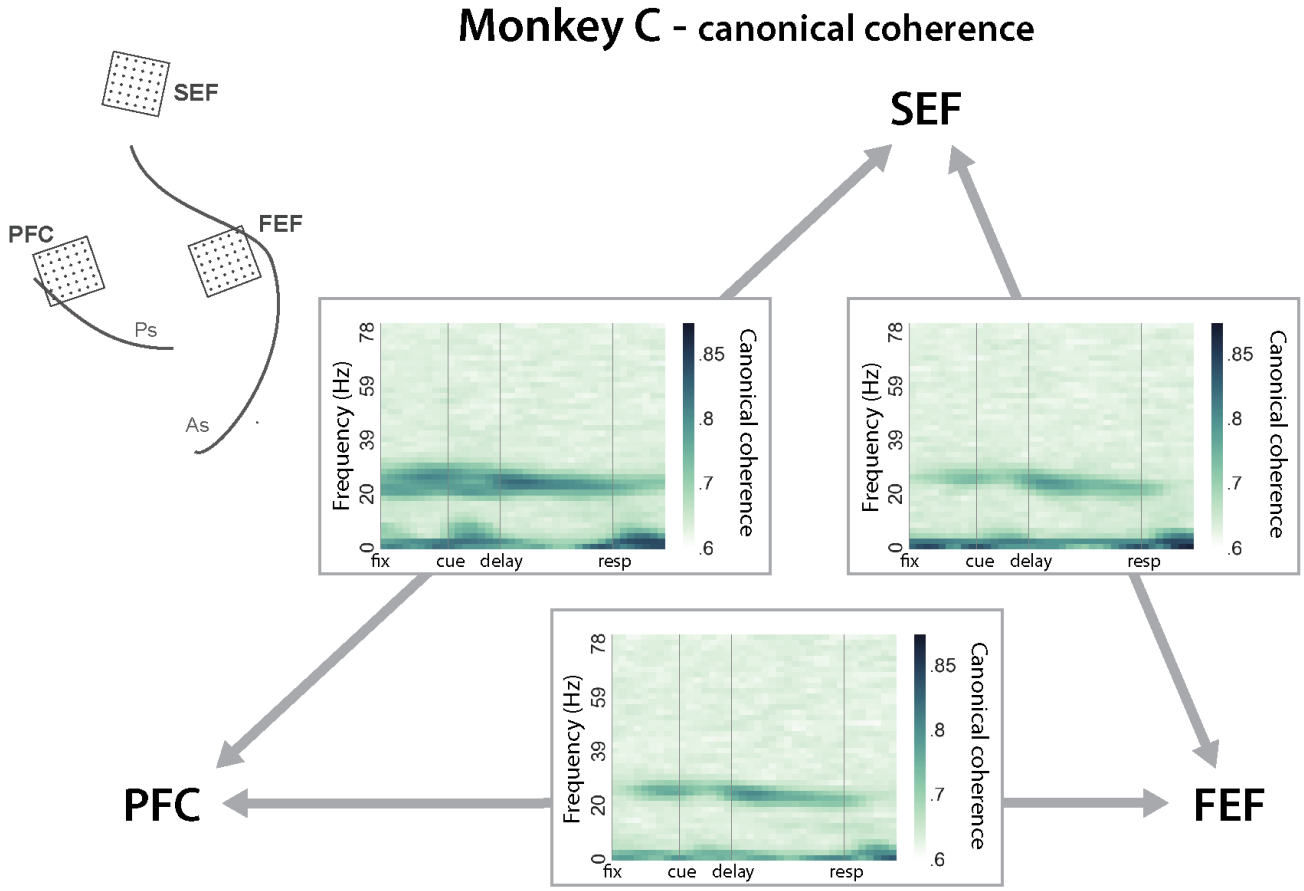

Figure 3.17. Canonical coherence between channels from PFC, SEF, and FEF, monkey C. Canonical coherence for each plot was averaged across all target conditions. Implant locations are shown on the top left corner of the figure. Y-axis marks frequencies from 0 to 80 Hz. Gray lines on the x-axis mark the onset of different epochs in trial: fixation, target, delay, and response.

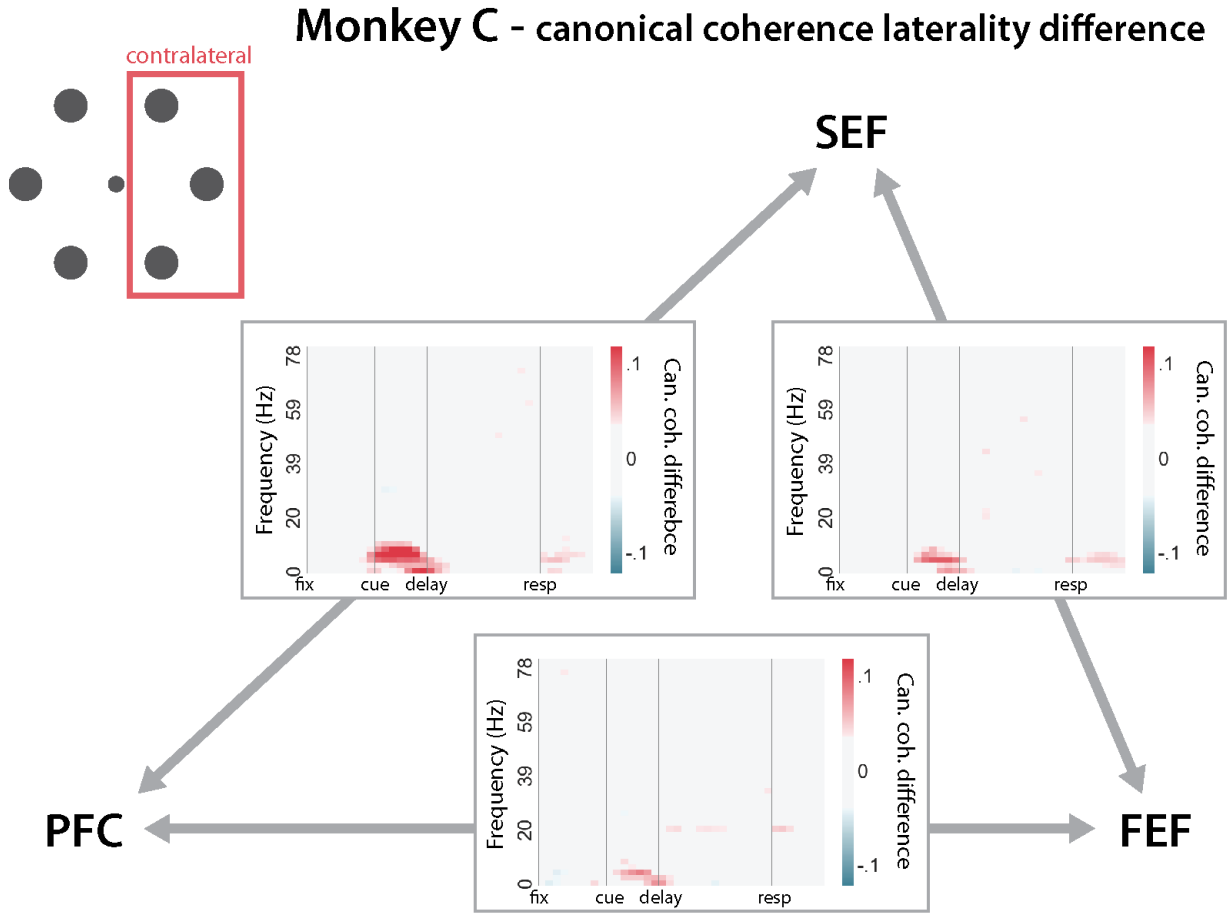

Figure 3.18. Laterality difference in canonical coherence between channels from PFC, SEF, and FEF, monkey C. Average difference in canonical coherence between contralateral targets and ipsilateral targets. Contralateral targets are indicated in red box on the top left. Y-axis marks frequencies from 0 to 80 Hz. Gray lines on the x-axis mark the onset of different epochs in trial: fixation, target, delay, and response.

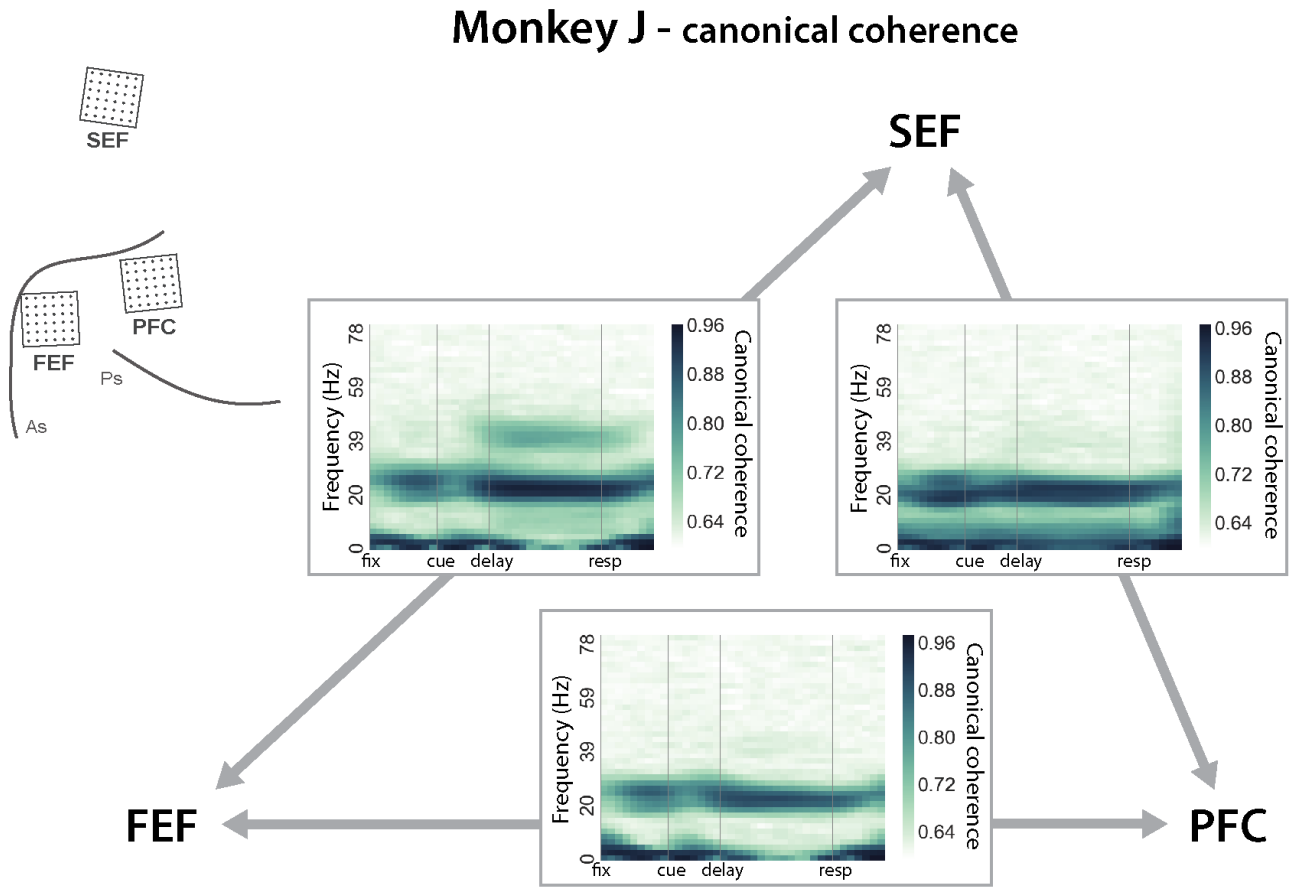

Figure 3.19: Canonical coherence between channels from PFC, SEF, and FEF, monkey J. Canonical coherence for each plot was averaged across all target conditions. Implant locations are shown on the top left corner of the figure. Y-axis marks frequencies from 0 to 80 Hz. Gray lines on the x-axis mark the onset of different epochs in trial: fixation, target, delay, and response.

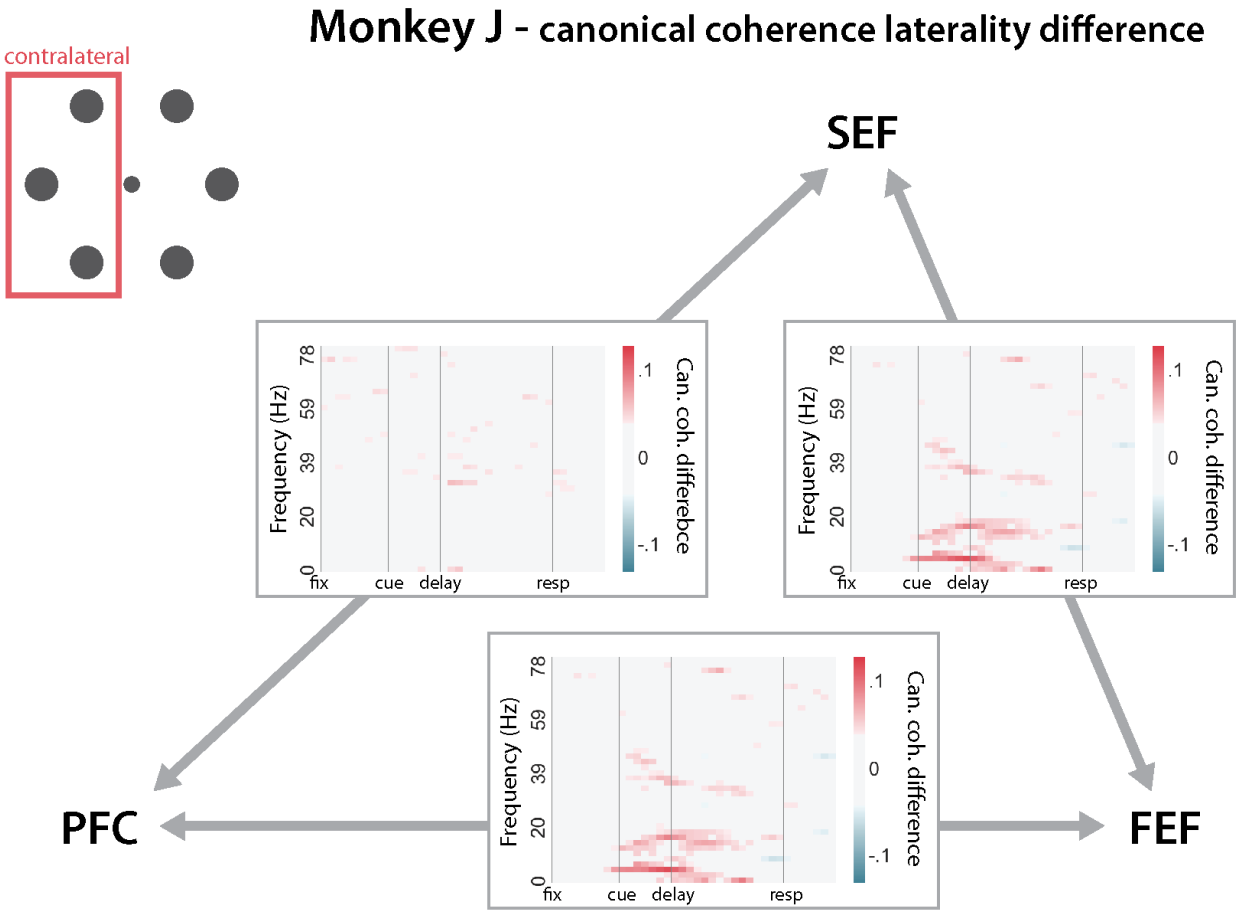

Figure 3.20. Laterality difference in canonical coherence between channels from PFC, SEF, and FEF, monkey J. Average difference in canonical coherence between contralateral targets and ipsilateral targets. Contralateral targets are indicated in red box on the top left. Y-axis marks frequencies from 0 to 80 Hz. Gray lines on the x-axis mark the onset of different epochs in trial: fixation, target, delay, and response.

3.4. Discussion

The current study is one of the first involving simultaneous large-scale chronic recordings in multiple prefrontal oculomotor regions. We explored interactions between neural signals in two broad categories: spike-field coupling and field-field coupling, to study changes in neural synchrony and functional connectivity in the frequency domain. Dynamic coupling patterns emerged from the study in multiple frequency bands, on both the single electrode scale and the whole region scale.

Spike-field coupling analysis was performed between spikes and LFPs on the same recording electrode. On average, increased spike-field coupling was present in the < 4 Hz band (delta) in both monkeys. This increased spike-field coupling mostly occurred right after epoch onsets during the task (e.g., Figures 3.2, 3.3, and 3.4), potentially reflecting responses to changes in the visual cues, such as when the target was presented during the cue period, or when the fixation dot disappeared in the response epoch to signal saccade execution or neural decoder choice. Besides the average spike-field coupling increase in the < 4 Hz band, some units also showed increased coupling in other frequency bands, such as in the 2-6 Hz band (Figures 3.3 and 3.4), or in the beta band (Figure 3.4). On average, spike-field coupling in the cue epoch (for monkey C) or delay epoch onset (for monkey J) was stronger when targets were presented in the contralateral visual field (Figure 3.6 B). The spike-field coupling results here are consistent with other reports of spikes providing information about ongoing LFPs typically in the < 10 Hz range (Belitski *et al.*, 2008, 2010; Rasch *et al.*, 2008; Nauhaus *et al.*, 2009; Whittingstall and

Logothetis, 2009). Low frequency bands have also been shown to be strongly modulated by stimulus (Luo and Poeppel, 2007; Lakatos *et al.*, 2008; Kayser *et al.*, 2009; Schroeder and Lakatos, 2009). For example, Lakatos and colleagues showed (Lakatos *et al.*, 2008) that delta-band oscillations in the primary visual cortex was entrained (phase-locked) to the rhythm of oscillatory input stimulus, and resulted in a response gain of task relevant events. Our results support the notion that slow oscillations are entrained by stimuli. In addition, they are influenced by the laterality of the stimuli, and manifest across multiple brain-regions, which suggest functional coupling on a macroscopic scale.

Field-field coupling revealed a very dynamic interaction. Field-field coupling analysis in this study was performed between pairs of all electrodes, resulting in a high dimensional network and 4560 unique pairs of electrodes. Functional coupling was found to be the strongest between channels from the same implant region. First, coherences between one channel and other channels of the same region generally varied in the same way (e.g., Figures 3.9 and 3.12, 'Coherence [15 30] Hz'). Second, distributions of coherence values revealed differences between within-region and inter-region couplings for both monkeys, where the means were higher for within-region distributions, and the KL divergences between within-region distributions were on average lower than between inter-region distributions (Figures 3.14 and 3.15). Lastly, target information that existed in within-region coherence was also generally higher than in inter-region (Figure 3.13 and 3.14). These findings suggest that coherence is predominantly an effect within the same brain region.

The direction of information flow could be inferred from the distribution of target information in coherence. SEF in monkey C showed high target selectivity in the alpha/mu band during the cue epoch, while coherence in the same frequency band contained target information between SEF and PFC, SEF and FEF, suggesting that target information was directed from SEF to the other two regions. Using the same logic (see detailed reasoning in section 3.2.2), target information in the same frequency band was most likely directed from FEF to SEF and PFC during the cue epoch for monkey J. In the beta band, PFC in monkey C was most likely directing target information to FEF, consistent with results from the canonical coherence analysis in which all three regions showed strong coherence in the beta band. For monkey J, target information flow in the beta band was likely in multiple directions, from PFC to SEF during the early delay epoch, and from FEF to SEF and PFC during the cue and late delay epochs. Thus, the flow of target information, inferred from both the strength of coherence and the distribution of target information in coherence, revealed different directions in different frequency bands, different task epochs, as well as differences between monkeys.

For both monkeys, strong coherence was found in the beta band from canonical coherence analysis. Beta band coherence was stronger during the fixation and delay epochs. In the literature, oscillation in the beta band is strongly linked to movement. There are multiple hypotheses regarding its functional role. Engel and Fries proposed it as a ‘status quo’ signal for maintaining inhibitory control or coordinating preparatory activity before movement (Engel and Fries, 2010). It has been implicated in top-down

attentional modulation (Buschman and Miller, 2007; Wang, 2010). It has also been suggested to serve as a medium in long-range communications (Kopell *et al.*, 2000). Results from this study are consistent with multiple proposed roles of the beta band. Stronger beta coherence during the fixation and delay periods indicate it was potentially related to maintaining inhibition of movements as well as top-down control, as the monkeys needed to remain focused during these task epochs. Information in beta coherence between the three implant regions also suggests that beta oscillation was involved in communications between brain regions. However, the distribution of target information in the beta band in this study was multifaceted, as it was dependent on the implant region as well as task epoch, and the flow of target information was multidirectional. Our study suggests that beta oscillation serves different roles in different brain regions and task contexts, and it is difficult to attribute its properties to a single purpose.

The results from canonical coherence analysis showed agreement with results from spike-field coupling analysis in the < 10 Hz band. With the exception of the delay epoch, increased coupling strength in this frequency range was found for all task epochs, potentially pointing to the same underlying neural mechanism responsible for this coupling increase across different neural signals. In future work, spike-field coupling can be extended to between spikes and LFPs on different recording electrodes (Wong *et al.*, 2016), and compared with field-field coupling.

3.5. Appendix

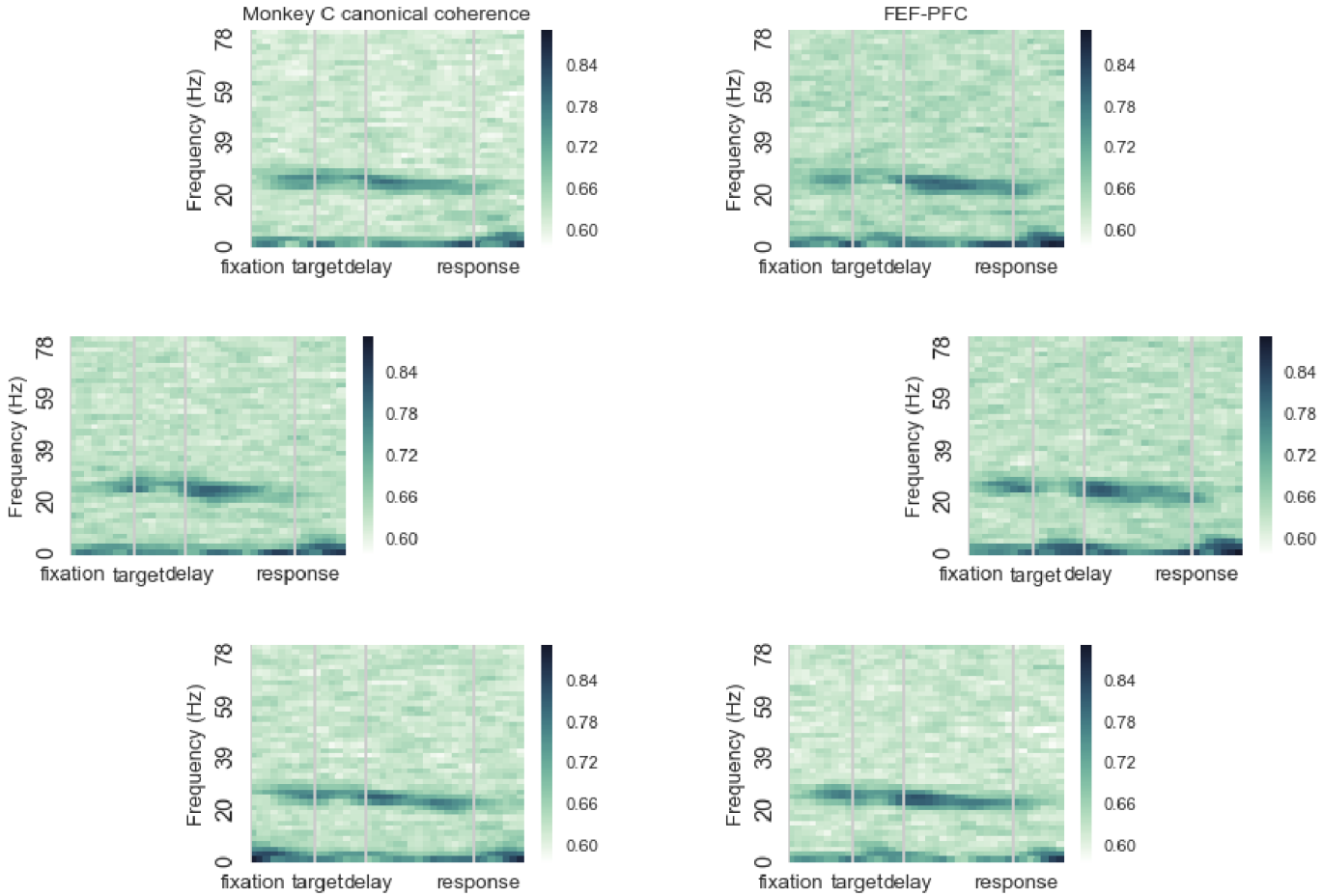

Figure 3.5.1. Canonical coherence between PFC and FEF, for 6 target conditions, monkey C. Each plot shows the spectrotemporal representation of the canonical coherence, computed from all the trials for each target, and placed at the corresponding target position.

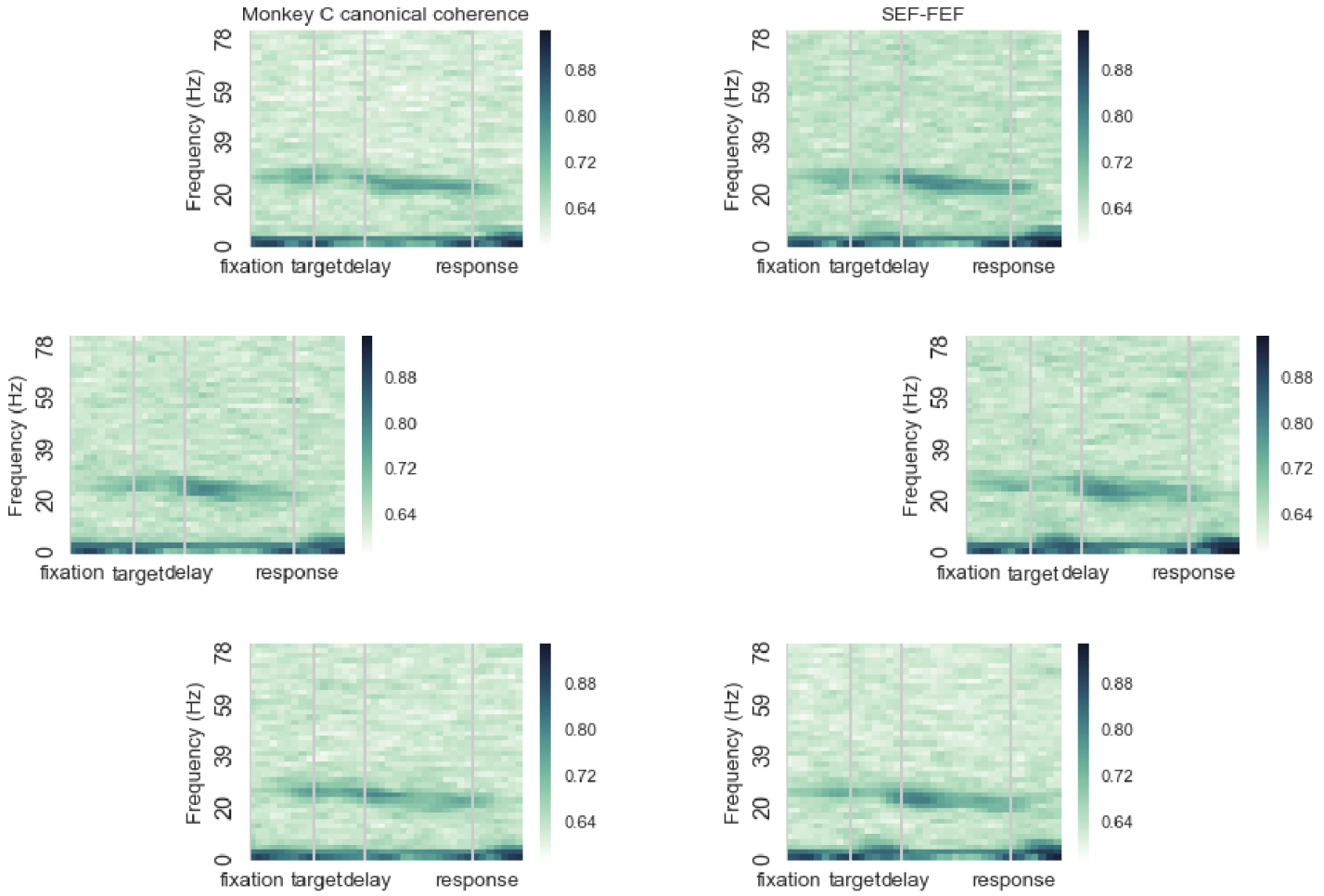

Figure 3.5.2. Canonical coherence between SEF and FEF, for 6 target conditions, monkey C. Each plot shows the spectrotemporal representation of the canonical coherence, computed from all the trials for each target, and placed at the corresponding target position.

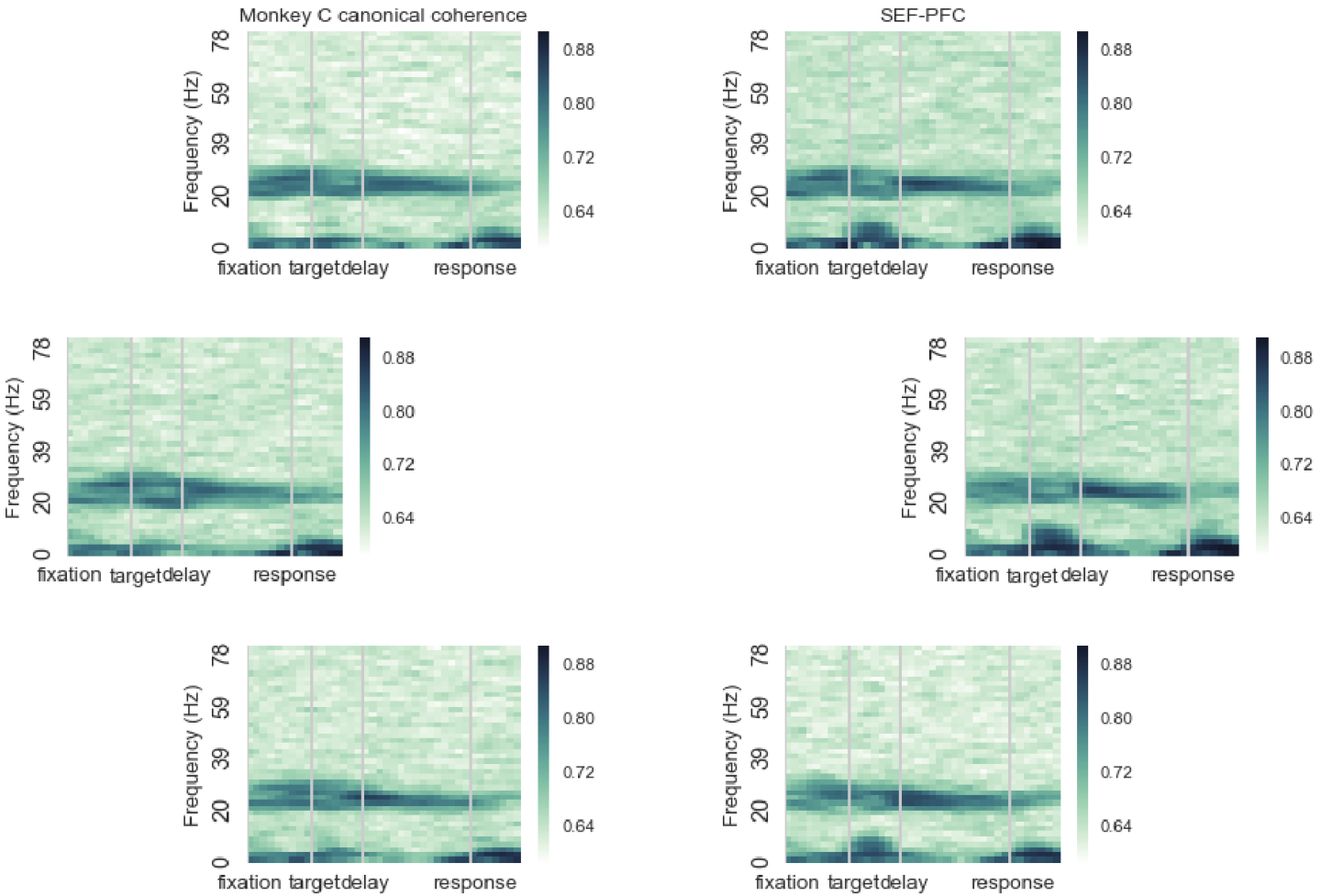

Figure 3.5.3. Canonical coherence between PFC and SEF, for 6 target conditions, monkey C. Each plot shows the spectrotemporal representation of the canonical coherence, computed from all the trials for each target, and placed at the corresponding target position.

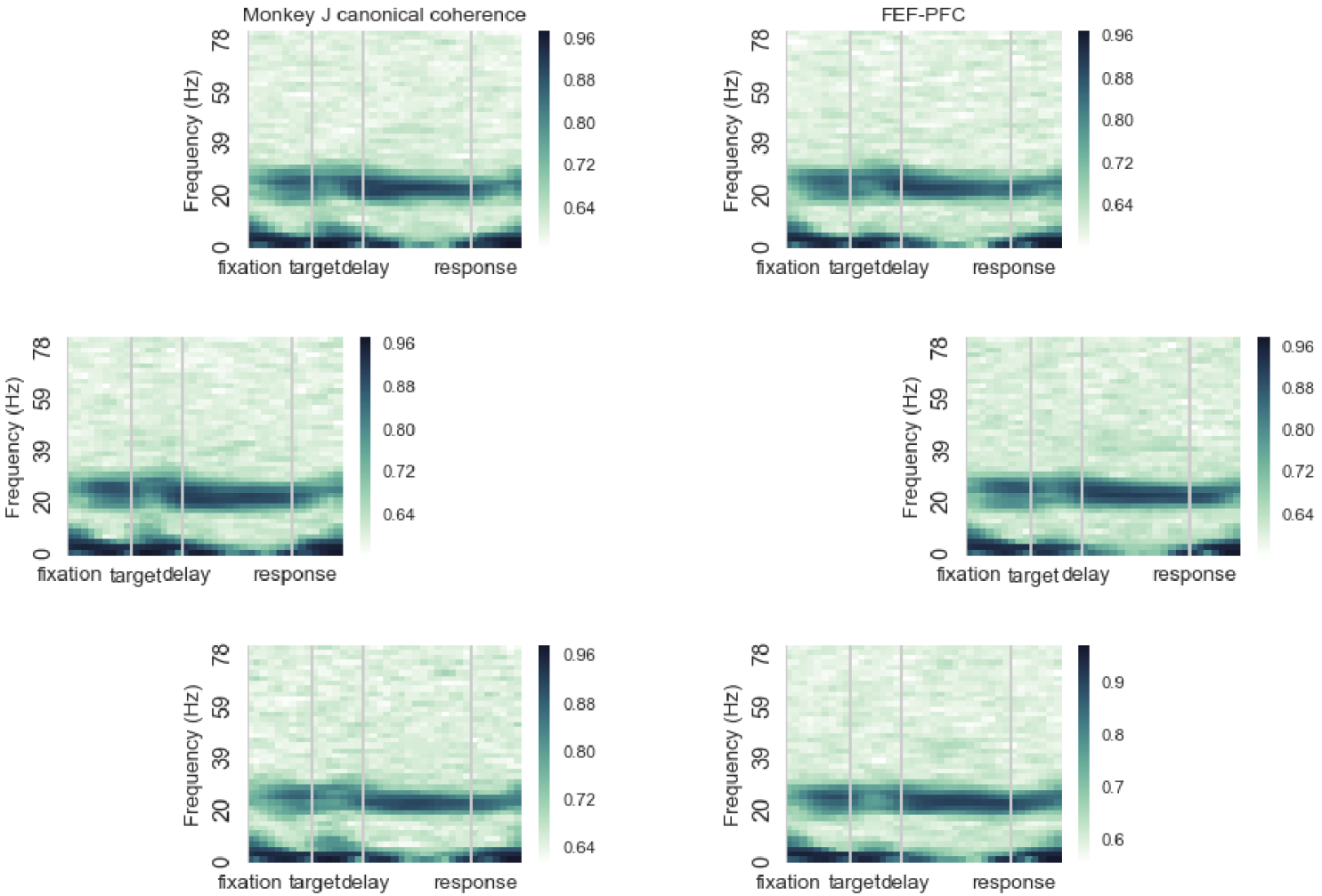

Figure 3.5.4. Canonical coherence between PFC and FEF, for 6 target conditions, monkey J. Each plot shows the spectrotemporal representation of the canonical coherence, computed from all the trials for each target, and placed at the corresponding target position.

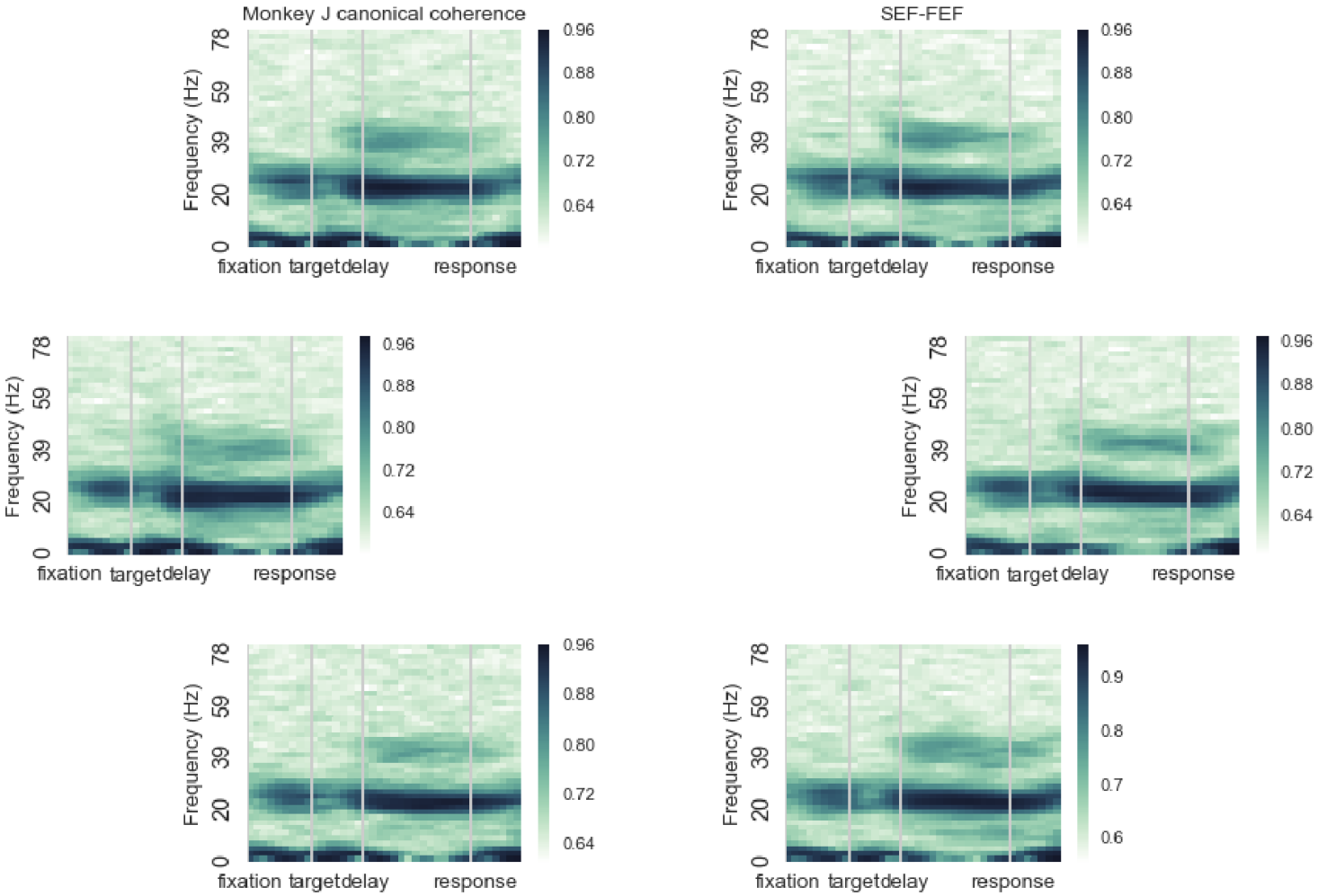

Figure 3.5.5. Canonical coherence between SEF and FEF, for 6 target conditions, monkey J. Each plot shows the spectrotemporal representation of the canonical coherence, computed from all the trials for each target, and placed at the corresponding target position.

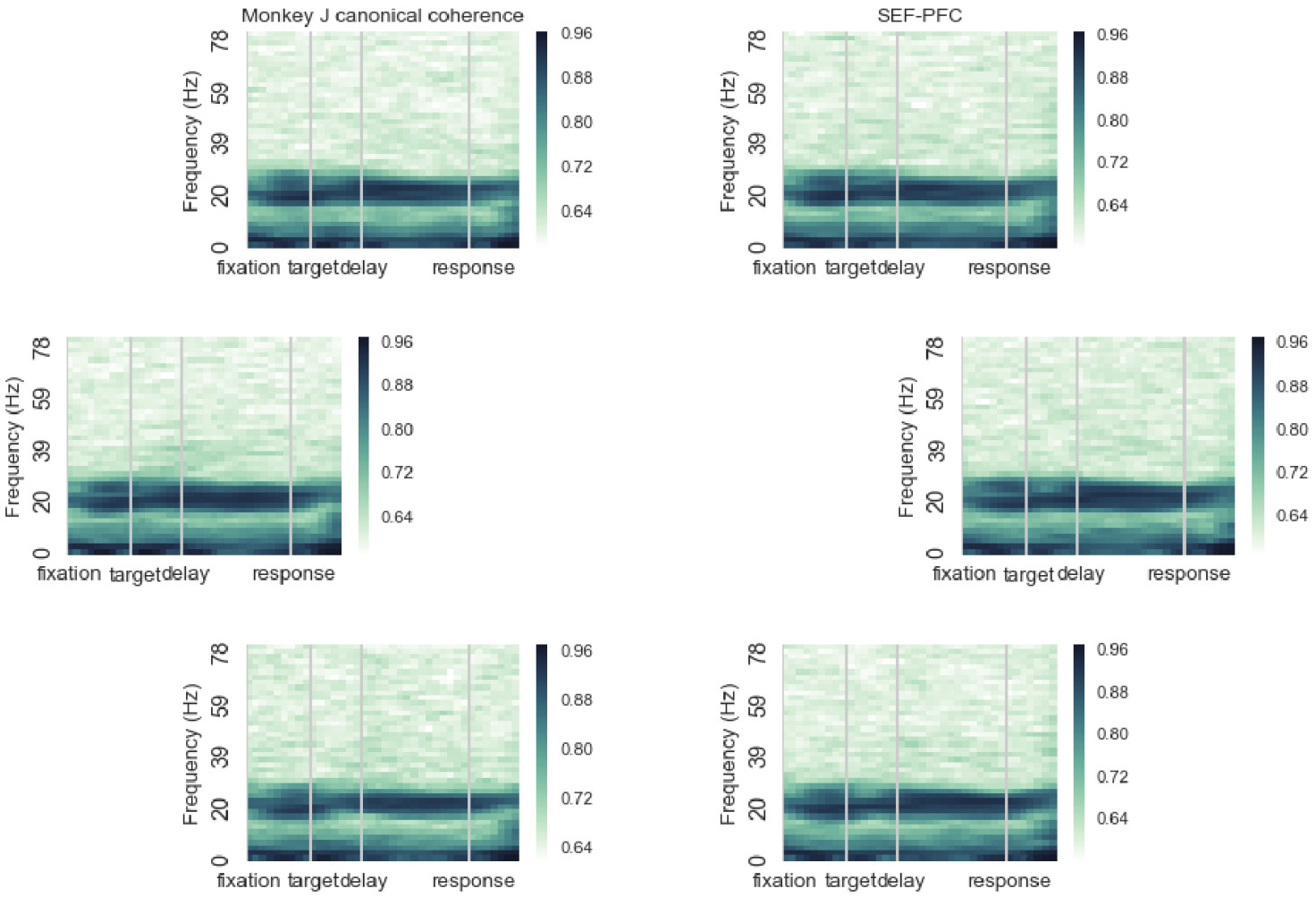

Figure 3.5.6. Canonical coherence between PFC and SEF, for 6 target conditions, monkey J. Each plot shows the spectrotemporal representation of the canonical coherence, computed from all the trials for each target, and placed at the corresponding target position.

4. CONCLUSION

This dissertation concerns the development of an intracortical oculomotor brain-computer interface (BCI). While most intracortical BCI applications have focused on replacing lost limb functions resulting from damaged neuromuscular tissues, the oculomotor system might be better suited for rapid serial selection tasks due to its distinct behavioral and neural properties. In Chapter 1 we introduced the concept and general overview of BCIs, provided a review of the oculomotor regions targeted in the current study. Chapter 2 focused on the detailed motivation, implementation, and results of the oculomotor BCI experiment. Chapter 3 described the functional connectivity between recorded brain regions on both electrode-electrode scale and region-region scale.

4.1. Oculomotor BCI

Unlike previous studies reporting a variety of signal types being optimal for decoding, we found that high-frequency LFP in the 80-500 Hz range provided the best decoding performance, regardless of decoder choice. Further analysis revealed that saccade target information was distributed in a wide frequency range, and differed between different channels, which contributed to the success of using the high-frequency LFPs. We further looked at area-specific target information in different signal types, and compared between the delay and response epochs. Overall areas SEF and FEF stood out as the most information-rich region, during both the delay and response epochs. Unlike previously

reported BCI studies, we did not observe any improvement in decoding performance with more practice, which suggests that the oculomotor system can be particularly efficient for BCI purposes, not demanding much effort from the users.

There were two particular challenges encountered in the BCI paradigm. One was a loss of motivation from the monkeys within the same recording sessions. Behavioral analysis indicated that both monkeys suffered a gradual decline in motivation/focus as the session progressed. Another issue was signal drift. Using an adaptive analysis, decoding performances for both monkeys improved when decoders were retrained after each trial rather than when they were only trained during the beginning of the BCI session. The effect of the adaptive decoder was apparent starting from the beginning of the BCI trials (around trial no. 300), whereas behavioral analysis showed a decline in motivation/focus starting around the middle of each session (around trial no. 1000). Therefore the effects of motivation loss and signal drift were distinctive from each other, and can be addressed separately.

4.2. Functional connectivity

Functional connectivity analysis was applied to neural signals on all channels to reveal any patterns that emerged in the spectrotemporal domain. Spike-field coupling measures were computed between spikes and LFP signals on the same recording electrode. Field-field coupling measures were computed between LFP signals on different recording

electrodes, and performed on two scales: electrode-electrode scale, and region-region scale.

Spike-field coherence analysis largely revealed increased coherence in the frequency range < 10 Hz, and most probably associated with visual stimuli. Field-field coherence on an electrode-electrode scale (measured in coherence) was found to be predominantly an effect within the same brain region. The coherence patterns were complex and dynamically changing in the task. However, coupling patterns were highly similar from one channel in one region to a group of channels in another region. For all three regions, coupling strength was modulated by the location of visual stimulus, both within-region, and inter-region. On a region-region scale, both subjects showed strong coherence in the beta band during the fixation and the delay epochs. In agreement with spike-field coherence, region-region scale coherence pattern also revealed strong coupling strength in <12 Hz range during fixation, cue and response epochs, and likely associated with visual stimuli as well. There were at least two dissociable components in the functional coupling: one that was associated with task epochs (e.g., beta band coherence), another that was modulated by the location of the visual target (e.g., coherence in beta, alpha/mu, gamma bands). This dissociation in functional connectivity has not been reported for these regions in the literature, and suggests that each frequency bands may have independent sources that modulate those rhythms.

4.3. Future directions

The analysis and results of this dissertation suggest that oculomotor BCI can be effective in serving as a communication channel. We have shown that target information existed in a very broad LFP band that can be extracted from a variety of decoders. Furthermore, unlike previously reported studies, the oculomotor BCI may not require any training from the end user. This could potentially reduce both time and human cost for the BCI community. Future work could explore other aspects of oculomotor BCI, such as controlling for signal drift using an adaptive approach, and reducing strain placed on the subjects due to motivation loss.

Further functional connectivity analysis could be performed, to analyze coupling between spikes and LFPs on different electrodes, compare and contrast similarities and differences in the coupling strength between spike-field coupling and field-field coupling. Future experiments could be designed to further explore the dissociable components in functional coupling, and their potentially independent mechanism of origin.

BIBLIOGRAPHY

Armstrong, K. M., Chang, M. H. and Moore, T. (2009) 'Selection and maintenance of spatial information by frontal eye field neurons.', *The Journal of neuroscience*, 29(50), pp. 15621–9. doi: 10.1523/JNEUROSCI.4465-09.2009.

Bansal, A. K., Truccolo, W., Vargas-Irwin, C. E. and Donoghue, J. P. (2012) 'Decoding 3D reach and grasp from hybrid signals in motor and premotor cortices: spikes, multiunit activity, and local field potentials.', *Journal of neurophysiology*, 107(5), pp. 1337–55. doi: 10.1152/jn.00781.2011.

Belitski, A., Gretton, A., Magri, C., Murayama, Y., Montemurro, M. A., Logothetis, N. K. and Panzeri, S. (2008) 'Low-frequency local field potentials and spikes in primary visual cortex convey independent visual information.', *The Journal of neuroscience*, 28(22), pp. 5696–709. doi: 10.1523/JNEUROSCI.0009-08.2008.

Belitski, A., Panzeri, S., Magri, C., Logothetis, N. K. and Kayser, C. (2010) 'Sensory information in local field potentials and spikes from visual and auditory cortices: time scales and frequency bands', *Journal of Computational Neuroscience*. Springer US, 29(3), pp. 533–545. doi: 10.1007/s10827-010-0230-y.

Bokil, H., Andrews, P., Kulkarni, J. E., Mehta, S. and Mitra, P. P. (2010) 'Chronux: a platform for analyzing neural signals.', *Journal of neuroscience methods*, 192(1), pp. 146–51. doi: 10.1016/j.jneumeth.2010.06.020.

Börgers, C. and Kopell, N. J. (2008) 'Gamma oscillations and stimulus selection.', *Neural computation*, 20(2), pp. 383–414. doi: 10.1162/neco.2007.07-06-289.

Boulay, C. B., Pieper, F., Leavitt, M., Martinez-Trujillo, J. and Sachs, A. J. (2015) 'Single-trial decoding of intended eye movement goals from lateral prefrontal cortex neural ensembles.', *Journal of neurophysiology*, 115(1), p. jn.00788.2015. doi: 10.1152/jn.00788.2015.

Brincat, S. L., Salazar-Gómez, A. F., Jia, N., Panko, M., Miller, E. K. and Guenther, F. H. (2013) 'Development of an intracortical eye movement-based brain-computer interface', in Millán, J. del R., Gao, S., Wolpaw, J. R., and Huggins, J. E. (eds) *Proceedings of the Fifth International Brain-Computer Interface Meeting: Defining the Future*. Graz: Graz University of Technology Publishing House, pp. 72–73. doi: 10.3217/978-3-85125-260-6-34.

Bruce, C. J., Goldberg, M. E., Bushnell, M. C. and Stanton, G. B. (1985) 'Primate frontal eye fields. II. Physiological and anatomical correlates of electrically evoked eye movements.', *Journal of neurophysiology*, 54(3), pp. 714–34. Available at:

http://www.ncbi.nlm.nih.gov/pubmed/4045546.

Buschman, T. J. and Miller, E. K. (2007) 'Top-Down Versus Bottom-Up Control of Attention in the Prefrontal and Posterior Parietal Cortices', *Science*, 315(5820).

Cardin, J. A., Carlén, M., Meletis, K., Knoblich, U., Zhang, F., Deisseroth, K., Tsai, L.-H. and Moore, C. I. (2009) 'Driving fast-spiking cells induces gamma rhythm and controls sensory responses.', *Nature*, 459(7247), pp. 663–7. doi: 10.1038/nature08002.

Carmena, J. M., Lebedev, M. A., Crist, R. E., O'Doherty, J. E., Santucci, D. M., Dimitrov, D. F., Patil, P. G., Henriquez, C. S. and Nicolelis, M. A. L. (2003) 'Learning to control a brain-machine interface for reaching and grasping by primates.', *PLoS biology*, 1(2), p. E42. doi: 10.1371/journal.pbio.0000042.

Chafee, M. V and Goldman-Rakic, P. S. (1998) 'Matching patterns of activity in primate prefrontal area 8a and parietal area 7ip neurons during a spatial working memory task.', *Journal of neurophysiology*, 79(6), pp. 2919–40. Available at: http://www.ncbi.nlm.nih.gov/pubmed/9636098 (Accessed: 22 March 2016).

Collinger, J. L., Wodlinger, B., Downey, J. E., Wang, W., Tyler-Kabara, E. C., Weber, D. J., McMorland, A. J. C., Velliste, M., Boninger, M. L. and Schwartz, A. B. (2013) 'High-performance neuroprosthetic control by an individual with tetraplegia.', *Lancet*, 381(9866), pp. 557–64. doi: 10.1016/S0140-6736(12)61816-9.

Engel, A. K. and Fries, P. (2010) 'Beta-band oscillations--signalling the status quo?', *Current opinion in neurobiology*, 20(2), pp. 156–65. doi: 10.1016/j.conb.2010.02.015.

Fries, P. (2005) 'A mechanism for cognitive dynamics: neuronal communication through neuronal coherence', *Trends in Cognitive Sciences*, 9(10), pp. 474–480. doi: 10.1016/j.tics.2005.08.011.

Fries, P. (2009) 'Neuronal Gamma-Band Synchronization as a Fundamental Process in Cortical Computation', *Annual Review of Neuroscience,* 32(1), pp. 209–224. doi: 10.1146/annurev.neuro.051508.135603.

Fries, P., Reynolds, J. H., Rorie, A. E. and Desimone, R. (2001) 'Modulation of Oscillatory Neuronal Synchronization by Selective Visual Attention', *Science*, 291(5508).

Funahashi, S., Bruce, C. J. and Goldman-Rakic, P. S. (1991) 'Neuronal activity related to saccadic eye movements in the monkey's dorsolateral prefrontal cortex.', *Journal of neurophysiology*, 65(6), pp. 1464–83. Available at: http://www.ncbi.nlm.nih.gov/pubmed/1875255 (Accessed: 2 May 2013).

Funahashi, S., Chafee, M. V and Goldman-Rakic, P. S. (1993) 'Prefrontal neuronal activity in rhesus monkeys performing a delayed anti-saccade task.', *Nature*, 365(6448), pp. 753–6. doi: 10.1038/365753a0.

Graf, A. B. A. and Andersen, R. A. (2014) 'Brain-machine interface for eye movements.', *Proceedings of the National Academy of Sciences of the United States of America*, 111(49), pp. 17630–5. doi: 10.1073/pnas.1419977111.

Grasse, D. W. and Moxon, K. A. (2010) 'Correcting the Bias of Spike Field Coherence Estimators Due to a Finite Number of Spikes', *Journal of Neurophysiology*, 104(1).

Guenther, F. H., Brumberg, J. S., Wright, E. J., Nieto-Castanon, A., Tourville, J. A., Panko, M., Law, R., Siebert, S. A., Bartels, J. L., Andreasen, D. S., Ehirim, P., Mao, H. and Kennedy, P. R. (2009) 'A Wireless Brain-Machine Interface for Real-Time Speech Synthesis', *PLoS ONE*, 4(12), p. e8218. doi: 10.1371/journal.pone.0008218.

Hastie, T., Tibshirani, R. and Friedman, J. J. H. (2001) *The elements of statistical learning*. Springer New York.

Hatsopoulos, N., Joshi, J. and O'Leary, J. G. (2004) 'Decoding continuous and discrete motor behaviors using motor and premotor cortical ensembles.', *Journal of neurophysiology*, 92(2), pp. 1165–74. doi: 10.1152/jn.01245.2003.

Histed, M. H. and Miller, E. K. (2006) 'Microstimulation of frontal cortex can reorder a remembered spatial sequence.', *PLoS biology*, 4(5), p. e134. doi: 10.1371/journal.pbio.0040134.

Hochberg, L. R., Serruya, M. D., Friehs, G. M., Mukand, J. A., Saleh, M., Caplan, A. H., Branner, A., Chen, D., Penn, R. D. and Donoghue, J. P. (2006) 'Neuronal ensemble control of prosthetic devices by a human with tetraplegia.', *Nature*, 442(7099), pp. 164–71. doi: 10.1038/nature04970.

Hsieh, L.-T. and Ranganath, C. (2014) 'Frontal midline theta oscillations during working memory maintenance and episodic encoding and retrieval.', *NeuroImage*, 85 Pt 2, pp. 721–9. doi: 10.1016/j.neuroimage.2013.08.003.

Huerta, M. F. and Kaas, J. H. (1990) 'Supplementary eye field as defined by intracortical microstimulation: Connections in macaques', *The Journal of Comparative Neurology*, 293(2), pp. 299–330. doi: 10.1002/cne.902930211.

Ifft, P. J., Shokur, S., Li, Z., Lebedev, M. A. and Nicolelis, M. A. L. (2013) 'A brain-machine interface enables bimanual arm movements in monkeys.', *Science translational medicine*, 5(210), p. 210ra154. doi: 10.1126/scitranslmed.3006159.

Isoda, M. and Tanji, J. (2003) 'Contrasting neuronal activity in the supplementary and frontal eye fields during temporal organization of multiple saccades.', *Journal of neurophysiology*, 90(5), pp. 3054–65. doi: 10.1152/jn.00367.2003.

Jensen, O., Gelfand, J., Kounios, J. and Lisman, J. E. (2002) 'Oscillations in the alpha band (9-12 Hz) increase with memory load during retention in a short-term memory task.', *Cerebral cortex,* 12(8), pp. 877–82. doi: 10.1093/CERCOR/12.8.877.

Johnston, K. and Everling, S. (2008) 'Neurophysiology and neuroanatomy of reflexive and voluntary saccades in non-human primates.', *Brain and cognition*, 68(3), pp. 271–83. doi: 10.1016/j.bandc.2008.08.017.

Kagan, I., Iyer, A., Lindner, A. and Andersen, R. A. (2010) 'Space representation for eye movements is more contralateral in monkeys than in humans.', *Proceedings of the National Academy of Sciences of the United States of America*, 107(17), pp. 7933–8. doi: 10.1073/pnas.1002825107.

Kayser, C., Montemurro, M. A., Logothetis, N. K. and Panzeri, S. (2009) 'Spike-Phase Coding Boosts and Stabilizes Information Carried by Spatial and Temporal Spike Patterns', *Neuron*, 61(4), pp. 597–608. doi: 10.1016/j.neuron.2009.01.008.

Kopell, N., Ermentrout, G. B., Whittington, M. A. and Traub, R. D. (2000) 'Gamma rhythms and beta rhythms have different synchronization properties', *Proceedings of the National Academy of Sciences of the United States of America*, 97(4), pp. 1867–1872. doi: 10.1073/pnas.97.4.1867.

Kubánek, J., Miller, K. J., Ojemann, J. G., Wolpaw, J. R. and Schalk, G. (2009) 'Decoding flexion of individual fingers using electrocorticographic signals in humans.', *Journal of neural engineering*, 6(6), p. 66001. doi: 10.1088/1741-2560/6/6/066001.

Lakatos, P., Karmos, G., Mehta, A. D., Ulbert, I. and Schroeder, C. E. (2008) 'Entrainment of Neuronal Oscillations as a Mechanism of Attentional Selection', *Science*, 320(5872).

Lepage, K. Q., Kramer, M. A. and Eden, U. T. (2011) 'The dependence of spike field coherence on expected intensity.', *Neural computation*, 23(9), pp. 2209–41. doi: 10.1162/NECO_a_00169.

Liu, J. and Newsome, W. T. (2006) 'Local field potential in cortical area MT: stimulus tuning and behavioral correlations.', *The Journal of neuroscience*, 26(30), pp. 7779–90. doi: 10.1523/JNEUROSCI.5052-05.2006.

Luo, H. and Poeppel, D. (2007) 'Phase Patterns of Neuronal Responses Reliably Discriminate Speech in Human Auditory Cortex', *Neuron*, 54(6), pp. 1001–1010. doi: 10.1016/j.neuron.2007.06.004.

Manning, J. R., Jacobs, J., Fried, I. and Kahana, M. J. (2009) 'Broadband shifts in local field potential power spectra are correlated with single-neuron spiking in humans.', *The Journal of neuroscience*, 29(43), pp. 13613–20. doi: 10.1523/JNEUROSCI.2041-09.2009.

Markowitz, D. A., Wong, Y. T., Gray, C. M. and Pesaran, B. (2011) 'Optimizing the decoding of movement goals from local field potentials in macaque cortex.', *The Journal of neuroscience*, 31(50), pp. 18412–22. doi: 10.1523/JNEUROSCI.4165-11.2011.

Martinez-Trujillo, J. C., Medendorp, W. P., Wang, H. and Crawford, J. D. (2004) 'Frames of reference for eye-head gaze commands in primate supplementary eye fields.', *Neuron*, 44(6), pp. 1057–66. doi: 10.1016/j.neuron.2004.12.004.

Mehring, C., Rickert, J., Vaadia, E., Cardosa de Oliveira, S., Aertsen, A. and Rotter, S. (2003) 'Inference of hand movements from local field potentials in monkey motor cortex.', *Nature neuroscience*, 6(12), pp. 1253–4. doi: 10.1038/nn1158.

Meyers, E. and Kreiman, G. (2011) 'Tutorial on Pattern Classification in Cell Recording', in Kriegeskorte and Kreiman (ed.) *Understanding visual population codes*. MIT Press.

Miller, K. J., Shenoy, P., den Nijs, M., Sorensen, L. B., Rao, R. N. and Ojemann, J. G. (2008) 'Beyond the gamma band: the role of high-frequency features in movement classification.', *IEEE transactions on bio-medical engineering*, 55(5), pp. 1634–7. doi: 10.1109/TBME.2008.918569.

Mitchell, D. J., McNaughton, N., Flanagan, D. and Kirk, I. J. (2008) 'Frontal-midline theta from the perspective of hippocampal "theta"', *Progress in Neurobiology*, 86(3), pp. 156–185. doi: 10.1016/j.pneurobio.2008.09.005.

Nauhaus, I., Busse, L., Carandini, M. and Ringach, D. L. (2009) 'Stimulus contrast modulates functional connectivity in visual cortex.', *Nature neuroscience*, 12(1), pp. 70–6. doi: 10.1038/nn.2232.

Pereda, E., Quiroga, R. Q. and Bhattacharya, J. (2005) 'Nonlinear multivariate analysis of neurophysiological signals.', *Progress in neurobiology*, 77(1–2), pp. 1–37. doi: 10.1016/j.pneurobio.2005.10.003.

Pesaran, B., Pezaris, J. S., Sahani, M., Mitra, P. P. and Andersen, R. A. (2002) 'Temporal structure in neuronal activity during working memory in macaque parietal

cortex.', *Nature neuroscience*, 5(8), pp. 805–11. doi: 10.1038/nn890.

Pierrot-Deseilligny, C., Milea, D., Mu, M. and Müri, R. M. (2004) 'Eye movement control by the cerebral cortex.', *Current opinion in neurology*, 17(1), pp. 17–25. doi: 10.1097/01.wco.0000113942.12823.e0.

Rainer, G., Asaad, W. F. and Miller, E. K. (1998) 'Selective representation of relevant information by neurons in the primate prefrontal cortex.', *Nature*, 393(6685), pp. 577–9. doi: 10.1038/31235.

Rasch, M. J., Gretton, A., Murayama, Y., Maass, W. and Logothetis, N. K. (2008) 'Inferring Spike Trains From Local Field Potentials', *Journal of Neurophysiology*, 99(3).

Ray, S., Crone, N. E., Niebur, E., Franaszczuk, P. J. and Hsiao, S. S. (2008) 'Neural correlates of high-gamma oscillations (60-200 Hz) in macaque local field potentials and their potential implications in electrocorticography.', *The Journal of neuroscience*, 28(45), pp. 11526–36. doi: 10.1523/JNEUROSCI.2848-08.2008.

Ray, S. and Maunsell, J. H. R. (2011a) 'Different origins of gamma rhythm and high-gamma activity in macaque visual cortex.', *PLoS biology*, 9(4), p. e1000610. doi: 10.1371/journal.pbio.1000610.

Ray, S. and Maunsell, J. H. R. (2011b) 'Network rhythms influence the relationship between spike-triggered local field potential and functional connectivity.', *The Journal of neuroscience*, 31(35), pp. 12674–82. doi: 10.1523/JNEUROSCI.1856-11.2011.

Robinson, D. A. and Fuchs, A. F. (1969) 'Eye movements evoked by stimulation of frontal eye fields', *Journal of Neurophysiology*, 32(5), pp. 637–648. Available at: http://jn.physiology.org/content/32/5/637 (Accessed: 28 February 2016).

Russo, G. S. and Bruce, C. J. (2000) 'Supplementary Eye Field: Representation of Saccades and Relationship Between Neural Response Fields and Elicited Eye Movements', *Journal of Neurophysiology* , 84(5), pp. 2605–2621. Available at: http://jn.physiology.org/content/84/5/2605.abstract?ijkey=e034d5b51f2ecec9ce4282dc3f0acb150d6bee59&keytype2=tf_ipsecsha (Accessed: 11 December 2012).

Saalmann, Y. B., Pigarev, I. N. and Vidyasagar, T. R. (2007) 'Neural Mechanisms of Visual Attention: How Top-Down Feedback Highlights Relevant Locations', *Science*, 316(5831), pp. 1612–1615. doi: 10.1126/science.1139140.

Sawaguchi, T. and Iba, M. (2001) 'Prefrontal cortical representation of visuospatial working memory in monkeys examined by local inactivation with muscimol.', *Journal of neurophysiology*, 86(4), pp. 2041–53. Available at:

http://jn.physiology.org/content/86/4/2041.abstract (Accessed: 24 March 2015).

Schalk, G., Kubánek, J., Miller, K. J., Anderson, N. R., Leuthardt, E. C., Ojemann, J. G., Limbrick, D., Moran, D., Gerhardt, L. A. and Wolpaw, J. R. (2007) 'Decoding two-dimensional movement trajectories using electrocorticographic signals in humans.', *Journal of neural engineering*, 4(3), pp. 264–75. doi: 10.1088/1741-2560/4/3/012.

Schroeder, C. E. and Lakatos, P. (2009) 'Low-frequency neuronal oscillations as instruments of sensory selection', *Trends in Neurosciences*, 32(1), pp. 9–18. doi: 10.1016/j.tins.2008.09.012.

Sederberg, P. B., Kahana, M. J., Howard, M. W., Donner, E. J. and Madsen, J. R. (2003) 'Theta and gamma oscillations during encoding predict subsequent recall.', *The Journal of neuroscience*, 23(34), pp. 10809–14. Available at: http://www.ncbi.nlm.nih.gov/pubmed/14645473 (Accessed: 1 August 2016).

Serruya, M. D., Hatsopoulos, N. G., Paninski, L., Fellows, M. R. and Donoghue, J. P. (2002) 'Instant neural control of a movement signal.', *Nature*, 416(6877), pp. 141–2. doi: 10.1038/416141a.

Siegel, M., Donner, T. H. and Engel, A. K. (2012) 'Spectral fingerprints of large-scale neuronal interactions.', *Nature reviews. Neuroscience*, 13(2), pp. 121–34. doi: 10.1038/nrn3137.

Siegel, M., Warden, M. R. and Miller, E. K. (2009) 'Phase-dependent neuronal coding of objects in short-term memory.', *Proceedings of the National Academy of Sciences of the United States of America*, 106(50), pp. 21341–6. doi: 10.1073/pnas.0908193106.

So, K., Dangi, S., Orsborn, A. L., Gastpar, M. C. and Carmena, J. M. (2014) 'Subject-specific modulation of local field potential spectral power during brain-machine interface control in primates.', *Journal of neural engineering*, 11(2), p. 26002. doi: 10.1088/1741-2560/11/2/026002.

Stark, E. and Abeles, M. (2007) 'Predicting movement from multiunit activity.', *The Journal of neuroscience*, 27(31), pp. 8387–94. doi: 10.1523/JNEUROSCI.1321-07.2007.

Takeda, K. and Funahashi, S. (2002) 'Prefrontal task-related activity representing visual cue location or saccade direction in spatial working memory tasks.', *Journal of neurophysiology*, 87(1), pp. 567–88. Available at: http://www.ncbi.nlm.nih.gov/pubmed/11784772 (Accessed: 28 February 2016).

Tanji, J. and Shima, K. (1994) 'Role for supplementary motor area cells in planning several movements ahead.', *Nature*, 371(6496), pp. 413–6. doi: 10.1038/371413a0.

Taylor, D. M., Tillery, S. I. H. and Schwartz, A. B. (2002) 'Direct cortical control of 3D neuroprosthetic devices.', *Science*, 296(5574), pp. 1829–32. doi: 10.1126/science.1070291.

Tehovnik, E. J., Sommer, M. a, Chou, I. H., Slocum, W. M. and Schiller, P. H. (2000) 'Eye fields in the frontal lobes of primates.', *Brain research. Brain research reviews*, 32(2–3), pp. 413–48. Available at: http://www.ncbi.nlm.nih.gov/pubmed/10760550.

Varela, F., Lachaux, J. P., Rodriguez, E. and Martinerie, J. (2001) 'The brainweb: phase synchronization and large-scale integration.', *Nature reviews. Neuroscience*, 2(4), pp. 229–39. doi: 10.1038/35067550.

Velliste, M., Perel, S., Spalding, M. C., Whitford, A. S. and Schwartz, A. B. (2008) 'Cortical control of a prosthetic arm for self-feeding.', *Nature*, 453(7198), pp. 1098–101. doi: 10.1038/nature06996.

Vinck, M., Battaglia, F. P., Womelsdorf, T. and Pennartz, C. (2012) 'Improved measures of phase-coupling between spikes and the Local Field Potential', *Journal of Computational Neuroscience*, 33(1), pp. 53–75. doi: 10.1007/s10827-011-0374-4.

Vinck, M., van Wingerden, M., Womelsdorf, T., Fries, P. and Pennartz, C. M. A. (2010) 'The pairwise phase consistency: A bias-free measure of rhythmic neuronal synchronization', *NeuroImage*, 51(1), pp. 112–122. doi: 10.1016/j.neuroimage.2010.01.073.

Wang, X.-J. (2010) 'Neurophysiological and Computational Principles of Cortical Rhythms in Cognition', *Physiological Reviews*, 90(3).

Weiss, S. and Rappelsberger, P. (2000) 'Long-range EEG synchronization during word encoding correlates with successful memory performance', *Cognitive Brain Research*, 9(3), pp. 299–312. doi: 10.1016/S0926-6410(00)00011-2.

Wessberg, J., Stambaugh, C. R., Kralik, J. D., Beck, P. D., Laubach, M., Chapin, J. K., Kim, J., Biggs, S. J., Srinivasan, M. A. and Nicolelis, M. A. (2000) 'Real-time prediction of hand trajectory by ensembles of cortical neurons in primates.', *Nature*, 408(6810), pp. 361–5. doi: 10.1038/35042582.

Whittingstall, K. and Logothetis, N. K. (2009) 'Frequency-band coupling in surface EEG reflects spiking activity in monkey visual cortex.', *Neuron*, 64(2), pp. 281–9. doi: 10.1016/j.neuron.2009.08.016.

Womelsdorf, T., Anton-Erxleben, K., Pieper, F. and Treue, S. (2006) 'Dynamic shifts of visual receptive fields in cortical area MT by spatial attention.', *Nature neuroscience*, 9(9), pp. 1156–60. doi: 10.1038/nn1748.

Womelsdorf, T. and Fries, P. (2007) 'The role of neuronal synchronization in selective attention', *Current Opinion in Neurobiology*, 17(2), pp. 154–160. doi: 10.1016/j.conb.2007.02.002.

Wong, Y. T., Fabiszak, M. M., Novikov, Y., Daw, N. D. and Pesaran, B. (2016) 'Coherent neuronal ensembles are rapidly recruited when making a look-reach decision', *Nature Neuroscience*, 19(2), pp. 327–334. doi: 10.1038/nn.4210.

Wu, W. and Hatsopoulos, N. G. (2008) 'Real-time decoding of nonstationary neural activity in motor cortex.', *IEEE transactions on neural systems and rehabilitation engineering*, 16(3), pp. 213–22. doi: 10.1109/TNSRE.2008.922679.

Zeitler, M., Fries, P. and Gielen, S. (2006) 'Assessing Neuronal Coherence with Single-Unit, Multi-Unit, and Local Field Potentials', *Neural Computation*, 18(9), pp. 2256–2281. doi: 10.1162/neco.2006.18.9.2256.

Zhuang, J., Truccolo, W., Vargas-Irwin, C. and Donoghue, J. P. (2010) 'Decoding 3-D reach and grasp kinematics from high-frequency local field potentials in primate primary motor cortex.', *IEEE transactions on bio-medical engineering*, 57(7), pp. 1774–84. doi: 10.1109/TBME.2010.2047015.

CURRICULUM VITAE